UNIVERSITY OF ICELAND

United Nations Educational, Scientific and Cultural Organization

GRÓ GTP
Geothermal Training Programme
Under the auspices of UNESCO

M.S. thesis
in Geology

Borehole geology of Well HLS-EX Hululais geothermal field, Sumatra Island, Indonesia

Vivi Dewi Mardiana Nusantara

Supervisor: Enikő Bali & Tobias Björn Weisenberger
May, 2022

FACULTY OF EARTH SCIENCES

Borehole geology of Well HLS-EX Hululais geothermal field, Sumatra Island, Indonesia

Vivi Dewi Mardiana Nusantara

M.S thesis in Geology
Supervisor: Enikő Bali & Tobias Björn Weisenberger
Faculty coordinator: Guðmundur Heiðar Guðfinnsson

Faculty of Earth Sciences
School of Engineering and Natural Sciences, University of Iceland
May, 2022

Borehole geology of Well HLS-EX
Hululais geothermal field, Sumatra Island, Indonesia

This thesis satisfies 60 credits towards an M.S.
in Geology in the Faculty of Earth Sciences,
University of Iceland, School of Engineering and Natural Sciences

Abstract

This study characterizes the stratigraphy and hydrothermal alteration of the 3,280 m deep HLS-EX well, in the Hululais geothermal field, Sumatra Island, Indonesia. Rock cuttings and cores were examined through stereo- and optical microscope, clay minerals were determined by X-ray diffractometry (XRD) and whole-rock compositions were studied by inductively coupled plasma-optical emission spectrometry (ICP-OES) and loss on ignition (LOI). These obtained data were combined with the results of drilling logs.

Eight rock types were distinguished in the borehole, including altered andesitic and dacitic lavas, intrusions of basaltic diorite, diorite, and granodiorite, andesitic and dacitic tuff, and volcanic breccia. Andesitic rocks dominate (~70%) in the borehole. Magmatic differentiation process was observed in the weakly altered rocks. The negative correlation between MgO and Na_2O, K_2O, SiO_2, and Zr indicates the incompatibility of these components in the andesitic magma from which most of the samples are derived. On the other hand, CaO decreases with MgO due to the crystal fractionation of plagioclase, FeO concentration decreases during the crystallization of Fe-Mg silicates (pyroxene and amphibole), and TiO_2 decreases due to the crystallization of Fe-Ti oxides.

The alteration intensity observed in the samples shows a positive correlation with the loss on ignition measurements, suggesting most of the samples are highly altered, especially in the pyroclastic tuff and volcanic breccia. Hydrothermal alteration zones are categorized as the smectite zone, epidote-illite zone, mixed-layer clay zone, and secondary biotite zone. Although it is slightly lower than the geothermometry profile, the measured borehole temperature trend is similar, representing a high-temperature geothermal well. Hydrothermal alteration processes have resulted in the geochemical modification of the magmatic rocks. Major and trace components were intensively mobilized during the alteration processes, and MgO was found to be the least mobile major component. The following processes were observed: silicification that increases the SiO_2, illitization results in gain of K_2O, chloritization, pyritization, and oxidation, which causes an increase in total iron, enrichment of Na_2O during albitization in some samples, whereas, in the other samples, kaolinization of plagioclase decreased the Na_2O concentration. Plagioclase breakdown leads to the mobilization of CaO and the leaching of calcium in the hydrothermally altered rocks.

Útdráttur

Í þessari rannsókn er jarðlögum og jarðhitaummyndun í hinni 3,280 m djúpu borholu HLS-EX á Hululais-jarðhitasvæðinu á eynni Súmötru í Indónesíu lýst. Borsvarf og borkjarnar voru skoðaðir með víðsjá og bergfræðismásjá, leirsteindir voru greindar með röntgentæki (XRD) og efnasamsetning bergsýna var greind með ICP-OES-tæki og glæðitapsmælingu (LOI). Þessi gögn voru samnýtt með borholumælingum.

Átta berggerðir fundust í borholunni, ummynduð andesít- og dasíthraun, basaltískt díórít-, díórít- og granódíórítinnskot, andesít- og dasítgjóskuberg og gosþursti. Andesítberg er ríkjandi (~70%) í holunni. Merki sjást um kvikuþróunarferli í því bergi sem er lítillega ummyndað. Neikvæð fylgni milli MgO og Na_2O, K_2O, SiO_2 og Zr gefur til kynna utangarðshegðun síðarnefndu efnanna í andesítkvikunni sem flest sýnin eiga uppruna sinn úr. Hins vegar lækkar styrkur CaO með lækkandi styrk MgO vegna hlutkristöllunar plagíóklass, styrkur FeO lækkar þegar Fe-Mg-silikröt (pýroxen og amfiból) kristallast og styrkur TiO_2 lækkar vegna kristöllunar Fe-Ti-oxíða.

Stig ummyndunar í sýnunum hefur jákvæða fylgni með glæðitapsmælingum, sem gefur til kynna að flest sýnanna séu mjög ummynduð, sérstaklega gjóskubergssýnin og gosþurstinn. Jarðhita-ummyndunarbelti eru flokkuð sem smektítbelti, epidót-illítbelti, blandleirsbelti og sekúndert bíótítbelti. Þó svo mældur hitaferill í holunni sé aðeins lægri en steindahitamælar gefa til kynna er um að ræða háhitaholu. Jarðhitummyndunarferli hafa leitt til jarðefnafræðilegra breytinga á storkuberginu. Mikil færsla var á bæði aðal- og snefilefnum af völdum ummyndunarinnar, en meðal aðalefna virðist MgO vera minnst hreyfanlegt. Eftirtalin ummyndunarferli greindust: kísilauðgun sem leiðir til aukins magns SiO_2, illítmyndun sem eykur styrk K_2O, klórítmyndun, pýrítmyndun og oxun, sem auka heildarmagn járns, auðgun í Na_2O af völdum albítummyndunar í sumum sýnum, á meðan kaólínummyndun á plagíóklasi leiddi til lækkunar á styrk Na_2O í öðrum sýnum. Niðurbrot á plagíóklasi leiðir til hreyfinga á CaO og útskolunar á kalsíni í bergi sem hefur orðið fyrir jarðhitaumynduninni.

To my father

Table of Contents

List of Figures

List of Tables

Abbreviations

AI: Alteration intensity.

BHA: Bottom hole assembly.

BPM: barrel per minute (equivalent to 153 liters per minute).

Bt: Bukit (translated as “Mountain”).

DSI: Dipole sonic imager.

Dm: Darcy meter.

EMS: Electronic Multi-Shot.

EOB: End of built.

GPM: gallon per minute.

ICP-OES: Inductively coupled plasma-optical emission spectrometry.

KOP: Kick-off point.

LCM: Loss circulation material.

LOI: Loss on ignition.

masl: meter above sea level.

MLC: Mixed-layer clay

MT: Magnetotelluric.

Mt: Mountain.

MWD: Measured-while drilling.

MWe: Megawatt electricity.

NW-SE: Northwest – southeast.

NNW-SSE: North northwest – south southeast.

PDC: Polycrystalline diamond compact.

PLC: Partial loss circulation.

PPL: Plane polarized light.

PT: Pressure Temperature

PT PGE: PT Pertamina Geothermal Energy

SWC: Sidewall core.

TD: Total depth.

TLC: Total loss circulation.

XPL: Crossed polarized light.

XRD: X-ray diffractometry.

Acknowledgements

I would like to acknowledge the GRÓ Geothermal Training Programme (GRÓ-GTP) under the auspices of the United Nations Educational, Scientific and Cultural Organisation (UNESCO) for providing me full support during my study at the University of Iceland. To Lúdvík Georgsson, Gudni Axelsson, Málfríður Ómarsdóttir, Ingimar Haraldsson, Markús Wilde, and Vigdís Harðardóttir, thank you for all of your assistance and encouragement in many circumstances.

I express my gratitude to PT Pertamina Geothermal Energy (PT PGE) Indonesia and my colleagues: Pak Tavip Dwikarianto, Pak M. Husni Thamrin, Pak Imam Baru Raharjo, Hary Koestono, Imam M. Prasetyo, Sapto Trianggo Nurseto, Dhani Marstiga, Graniko, and Tajul, for giving me access to the drilling data and many supportive conversations for this study.

I would like to thank my supervisors, Enikő Bali and Tobias Björn Weisenberger, for their thoughtful guidance, advice, and time invested in the knowledge-sharing process during my study. Thanks to Anette K. Mortensen for many constructive inputs and insights to shape my study objectives, Guðmundur Heiðar Guðfinnsson for helping me to coordinate this thesis program and the translations, Jóhann Gunnarsson Robin for his help in the ICP-OES preparation and measurement work, and Sigurdur Sveinn Jónsson for his assistance in the XRD analysis work.

I am grateful to have empowering and solid friends that constantly keep me motivated to pursue my goals. Thanks to Erick for the many hours and frustrations spent tutoring me with the programming language and marvelous experiences. I thank Araksan for her help in the sample preparation works, Tingting and Daniel for their positive energy, Ari for her genuine heart, Santiago and Nick for their friendship and hard jokes, and my GRO-GTP fellows 2020/2021 for their support and accompany. Finally, thanks to my beloved family and Indonesian friends for their encouragement and prayers during my stay in Iceland.

1 Introduction

1.1 Background and objectives

Situated in the belt of the ring of fire, Indonesia is naturally blessed with tremendous geothermal energy manifested as volcanoes and geothermal activity on the surface. In 2021, the geothermal potency in Indonesia was estimated to be at around 29,000 MWe, with 1,948.5 MWe installed capacity. It establishes Indonesia as the second-largest country in geothermal utilization, behind the United States of America, which utilized 3,676 MWe (Darma et al., 2021). Numerous efforts have been made to utilize geothermal energy to fulfill the necessity of sustainable clean energy, largely for electricity generation.

PT Pertamina Geothermal Energy (PT PGE) is a company engaged in the geothermal energy sector from exploration to utilization in Indonesia. Established in 2006, PT PGE has been working on geothermal energy development in several potential fields in Celebes, Java, and Sumatra Island, with 672 MWe installed capacity by 2021. On Sumatra Island itself, PT PGE operates seven geothermal fields, including the Hululais geothermal field. Hululais geothermal field is located in Lebong district, Bengkulu province, Indonesia (Figure 1.1).

Figure 1.1 Location map of the Hululais geothermal field.

The Hululais geothermal field is significant in the national power expansion project for the South Sumatra area, which is encountering a power shortage. Moreover, the development of this field will promote environmentally friendly power generation from a non-fossil energy source. The Hululais geothermal field is targeted to generate 110 MWe power when it is connected to the transmission system. Accordingly, twenty-four deep geothermal wells have been drilled to fulfill the steam capacity for electricity generation.

During the drilling of a geothermal well, several initial data are retrieved in the form of rock cuttings, cores, and drilling logs. These initial data are discovered with a costly and vulnerable drilling process. Therefore, a detailed borehole geology study needs to be done to understand the subsurface geology in the prospect area, assess the natural resource's potential and risk, and forecast the next well targeting program for future development. On a larger scale, the borehole geology study is beneficial for constructing the subsurface model and inputs for a long-term field development strategy.

This thesis implements a borehole geology study to characterize the subsurface geology of a geothermal well, called HLS-EX, from the Hululais geothermal field. The rock cuttings, cores, and drilling logs data were examined through the stereomicroscopy and petrographic analysis, inductively coupled plasma-optical emission spectrometry (ICP-OES), loss on ignition (LOI), and X-ray diffractometry (XRD) analysis. The borehole geology study in well HLS-EX aims to:

1. Construct a subsurface stratigraphy along the borehole.
2. Determine the hydrothermal alteration zones and their secondary mineral assemblages.
3. Compare the borehole stratigraphy and hydrothermal alteration zone with the general subsurface model from the field.
4. Compare the mineral geothermometry with the current measured temperature from the borehole.
5. Elaborate the effects of the hydrothermal alteration process.

1.2 Previous research in the study area

In 1993, the preliminary geology, geochemistry, and geophysical surveys were conducted in the Hululais geothermal field. The surveys identified the area as a graben structure produced by the NW-SE movement of the Sumatran Fault system, accompanied by acid volcanism and granite to diorite intrusions. Reservoir temperature was estimated from 250 to 300 °C, with fumaroles and acid pools were discovered at a high elevation, about 1,050 to 1,300 masl (Budiardjo et al., 2001). The magnetotelluric (MT) survey indicates that the conductive anomaly with apparent resistivity less than 10 Ωm near the thermal springs is associated with hydrothermal alteration (Mulyadi, 1995).

Pratama et al. (2020) produced the volcano stratigraphy of the field from surface geological mapping. In parallel, the fault network of the Hululais geothermal system was observed by Nurseto et al. (2021). The results show that the NW-SE and NNW-SSE fault trends are responsible for the focal feed zone in the production wells. Furthermore, the study explained that the volcanic evolution of Mt. Suban Agung is related to the development of geothermal resources in the area. The microearthquake monitoring measured similar NW-SE trend with some variation of NE-SW fracture trend related to the Ketahun and Musi segment in the Hululais area (Juanda et al., 2015).

The conceptual model of the Hululais geothermal system points out that the upwelling zone is situated beneath the Mt. Suban Agung crater (Budiardjo et al., 2001). It is supported by the hydrothermal mineralogy assessment from the first exploratory well drilled near Mt. Suban Agung (Koestono et al., 2015). The first exploratory well was drilled in 2012, indicating favorable temperature and permeability in the prospect area. The first 3D geology model of the field was constructed in 2016, suggesting the upwelling system is related to the thermal activity in Mt. Suban Agung and Mt. Beriti. The general subsurface rock formation in the field is categorized into five formations: the Upper and Lower Suban Agung Volcanic, Hululais Volcanic, Hululais Granodiorite Intrusions, and the Seblat Metasediment formation (Nusantara et al., 2020).

Arifin et al. (2020) studied the feed points in the production and injection wells. The study depicts that the permeability of the wells is controlled by geological structures and lithological factors. The highest permeability zone was associated with fractures due to the fault zone in well pads C and E, followed by the diffuse permeability within the tuff and breccia unit, as shown in well pad P. The minor permeable zone was associated with the distributed fractures within granodiorite as manifested in well pad H.

Located in well pad E and closer to Mt. Suban Agung and Mt. Beriti Besar, which were mentioned as the sweet spots of the area, HLS-EX is anticipated to become a significant steam producer for the field. There has not been any borehole geology study covering hydrothermal alteration and rock chemistry in the Hululais geothermal field. This study will provide information about surbsurface stratigraphy and hydrothermal alteration process in the borehole HLS-EX. Furthermore, this pilot study is expected to be applied and collaborated with other approaches for the subsequent geothermal wells.

2 Geology

2.1 Tectonic setting

Indonesia is an archipelago country of more than 17,000 islands stretching over 5,000 km from east to west and 1,800 km from north to south. Indonesia is situated between 95° and 141° east and crossing the equator from 6° north to 11° south. Sumatra Island forms the western end of the Indonesia archipelago (Hall, 2009). Sumatra Island extends in an NW-SE direction across the equator for 1,760 km long and about 400 km wide. Sumatra lies on the active edge of the Sunda Land, at the southeastern tip of the Eurasian Plate. The relative movement of the Indian Ocean in a north-northeast direction results in the oblique subduction along the Sunda Subduction Zone (Figure 2.1).

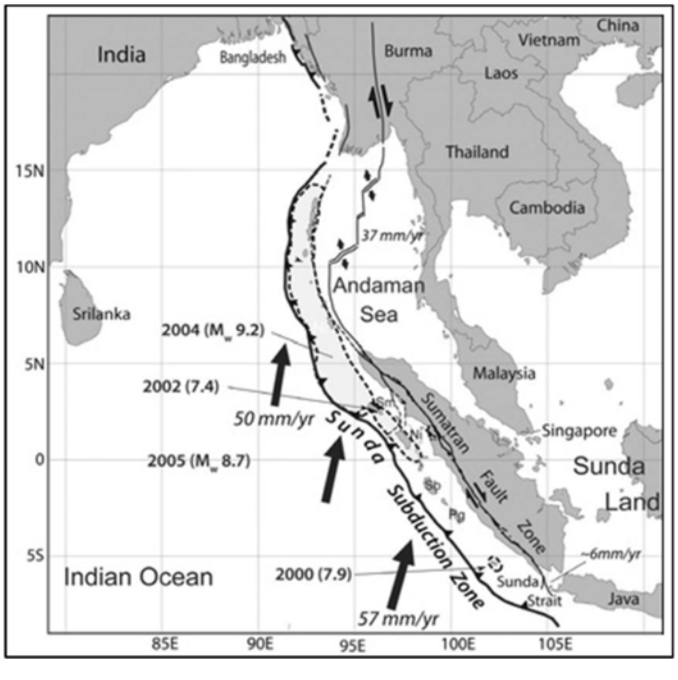

Figure 2.1 Tectonic control in Sumatra Island is affected by the subduction activity and the right-lateral strike-slip mega Sumatran Fault (Natawidjaja & Triyoso, 2007).

Sumatra is a manifest of slip partitioning, which occurs when the relative motion between two obliquely converging plates is taken up on multiple parallel faults. The subduction rate in this region is estimated at around 50 to 57 mm per year. In Sumatra, the tectonic movement of the Eurasian and Indian Plates controls the right-lateral strike-slip mega Sumatran Fault (Sieh & Natawidjaja, 2000). The offset of the Sumatran Fault on the surface is around 20 km, trending northwest-southeast. The Sumatran Fault is segmented into nineteen segments along its mega fault zone (Sieh & Natawidjaja, 2000).

Prominent high-temperature geothermal prospect areas associated with clustered volcanoes are discovered along the Sumatran Fault, namely Kutacane, Sipohon, Sarulla, Pintupadang, Panyambungan, Tanjungbatung, Singkarak, Muaralaboh, Sungaipenuh, Tambangsawah, Hululais, Talakemang, Suoh, and Antatai. Importantly, these geothermal prospect areas are situated in the pull-a-part basin between two overlapped segments (Figure 2.2).

Figure 2.2 High-temperature geothermal prospect areas along the Sumatran Fault. Note the location of the Hululais geothermal field in the southern part of Sumatra Island (Nurseto et al., 2021).

2.2 Geology of the Hululais area

The Hululais geothermal field lies in a pull-a-part basin between the Ketahun and Musi segments (Figure 2.3). The movement of the pull-a-part basin combined with the right-lateral strike-slip Sumatran Fault affects the structural trends in the Hululais area. Consequently, the major structural trends in the Hululais geothermal field are NW-SE and NNW-SSE. The two structural trends control the natural permeability as open fractures, extensional faults, and surface thermal manifestation lineaments (Figure 2.3). Deposits of the Quaternary volcanism products compose the geology of the Hululais geothermal field. On the surface, it is outcropped as lava, breccia, and pyroclastic product with andesitic composition. The geological map of the Hululais geothermal field is presented in Figure 2.4.

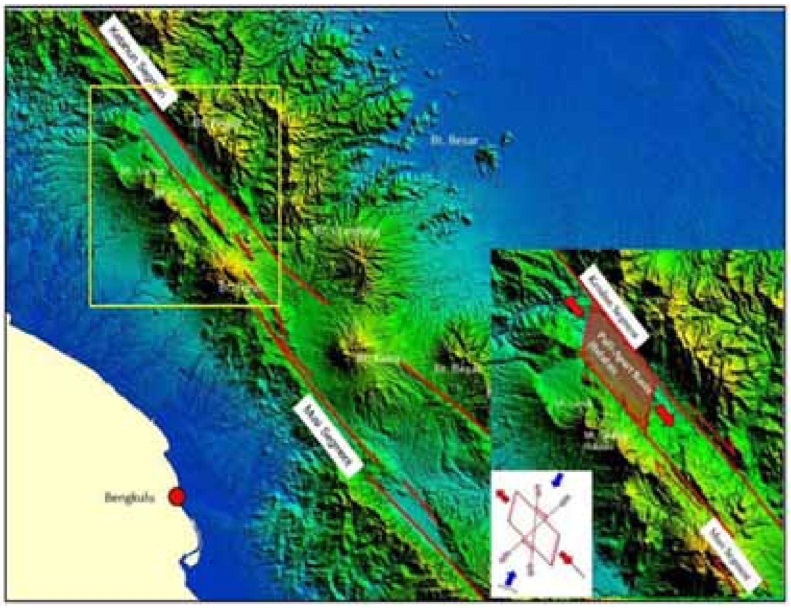

Figure 2.3 Hululais geothermal field is located in a pull-a-part basin system between Ketahun and Musi segments. The yellow frame points out the Hululais geothermal field location zoomed in the lower right corner (Nurseto et al., 2021).

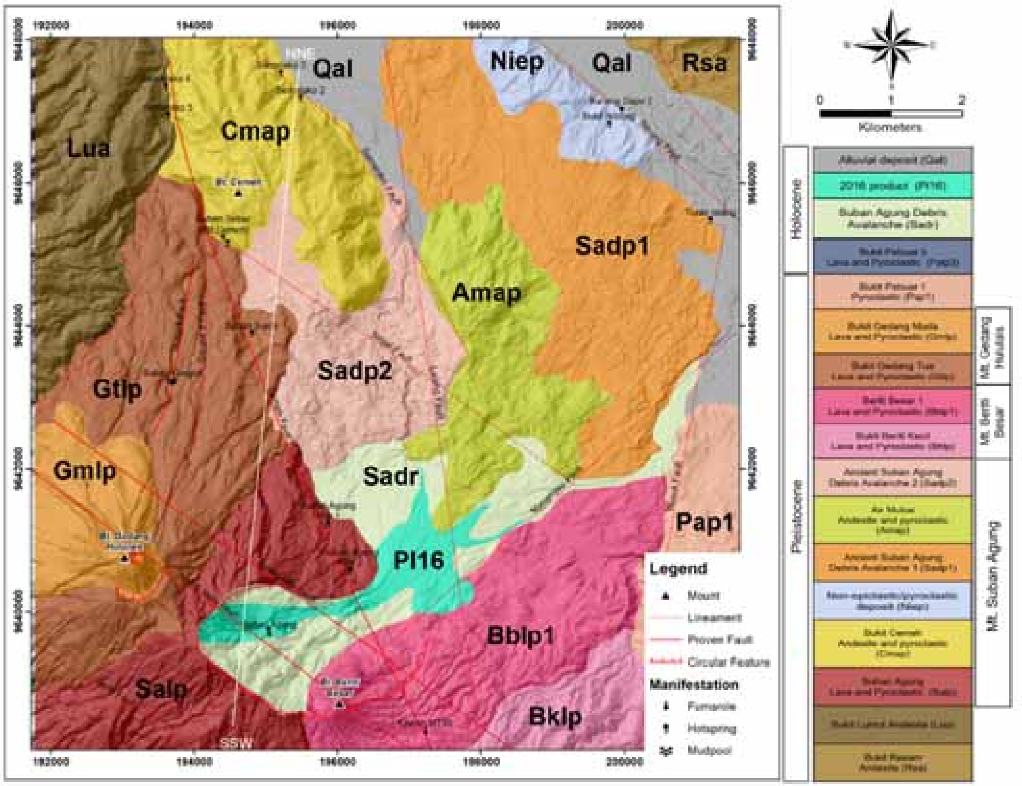

Figure 2.4 Geological map of Hululais geothermal field (PT Pertamina Geothermal Energy Indonesia, 2021).

At least three inactive volcanoes were identified in Hululais geothermal field; mentioned from the younger to older sequences are Mt. Gedang Hululais, Mt. Beriti Besar, and Mt. Suban Agung (Figure 2.4). The products of Mt. Gedang Hululais are composed of the Gedang Muda lava and pyroclastic (Gmlp) and Gedang Tua lava and pyroclastic (Gtlp) formation. The Gmlp is younger than Gtlp formation. Gmlp occupies the central part of Mt. Gedang Hululais to the relatively northwest part of the mountain. The Gmlp formation is composed of lava andesite, andesitic breccia, and hydrothermal breccia. Kaolinite associated with low pH hydrothermal fluid is commonly found in the Gmlp formation. The Gtlp formation covers the proximal and northern distal parts of Mt. Gedang Hululais. Andesitic lava and breccia associated with obsidian dominate the product of Gtlp formation. The product of Mt. Beriti Besar is depicted as Bblp1 (Beriti Besar 1 lava and pyroclastic) and distributed in the southeastern part of the Mt. Suban Agung caldera (Figure 2.4). It is composed of andesitic lava, breccia, tuff, and hydrothermal clay deposits.

Mt. Suban Agung is the oldest and largest quaternary volcano in the Hululais geothermal field. The age of Mt. Suban Agung volcanic product was estimated to be around 0.907 ± 0.25 million years, based on K/Ar from the andesite samples (PT Pertamina, 1994). The product of Mt. Suban Agung is composed of andesitic lava and pyroclastics (Salp) and the Suban Agung debris avalanche (Sadr) formations. The rocks are intensely altered in the Mt. Suban Agung crater area due to hydrothermal activities associated with steam vents, hot springs, steam-heated water, and hot ground. The primary cinder cone of Mt. Suban Agung has been modified by its ancient eruption. The eruption induced a 2 km diameter crater structure (or so-called caldera) that collapsed towards the northeast direction. During the destructive period, the body of ancient Mt. Suban Agung collapsed and ejected debris avalanches products, i.e., colluvium deposit, lava, and pyroclastic flow. This event produced the modern morphology of Mt. Suban Agung, as illustrated in Figure 2.5.

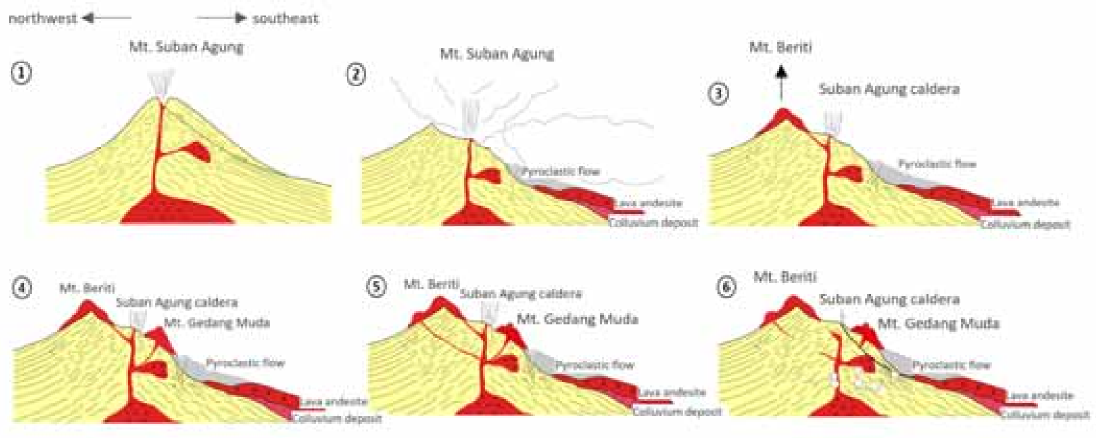

Figure 2.5 The evolution of Mt. Suban Agung (Nurseto et al., 2021).

The product of debris avalanches followed the northeast collapse structure from Mt. Suban Agung caldera and was deposited in the lower elevation as colluvium deposits. The ancient debris avalanches were deposited in three periods, and it is distinguished as Ancient Suban Agung Debris Avalanche 1 (Sadp1), Suban Agung Debris Avalanche 2 (Sadp2), and Suban Agung Debris Avalanche (Sadr). The most recent debris avalanche product was deposited in 2016 through a natural catastrophic event near the Mt. Suban Agung crater, and it is illustrated as the 2016 product (PI16). Modern unconsolidated deposits are depicted as colluvium and alluvial cover on the surface. It is found in the north and northeastern part of the area as the product of flood plain deposits in the lower part of the basin (Figure 2.4).

The subsurface rock in Hululais geothermal field is simplified into five formations: Upper Suban Agung Volcanic (USAV), Lower Suban Agung Volcanic (LSAV), Hululais Volcanic (HV), Hululais Granodiorite Intrusion (HGI), and Seblat Metasediment (SM). The USAV formation consists of pyroclastic tuff, volcanic breccia, and lahars. The LSAV comprises intercalation of andesitic lavas, andesitic breccia, and lithic tuff. The HV is composed of andesitic lava, autoclastic breccia, and ignimbrite. The HGI is composed of a granodiorite intrusion body. Lastly, the SM is indicated by the biogenic metasedimentary rocks scattered as lenses layers in the subsurface (PT Pertamina Geothermal Energy, 2021).

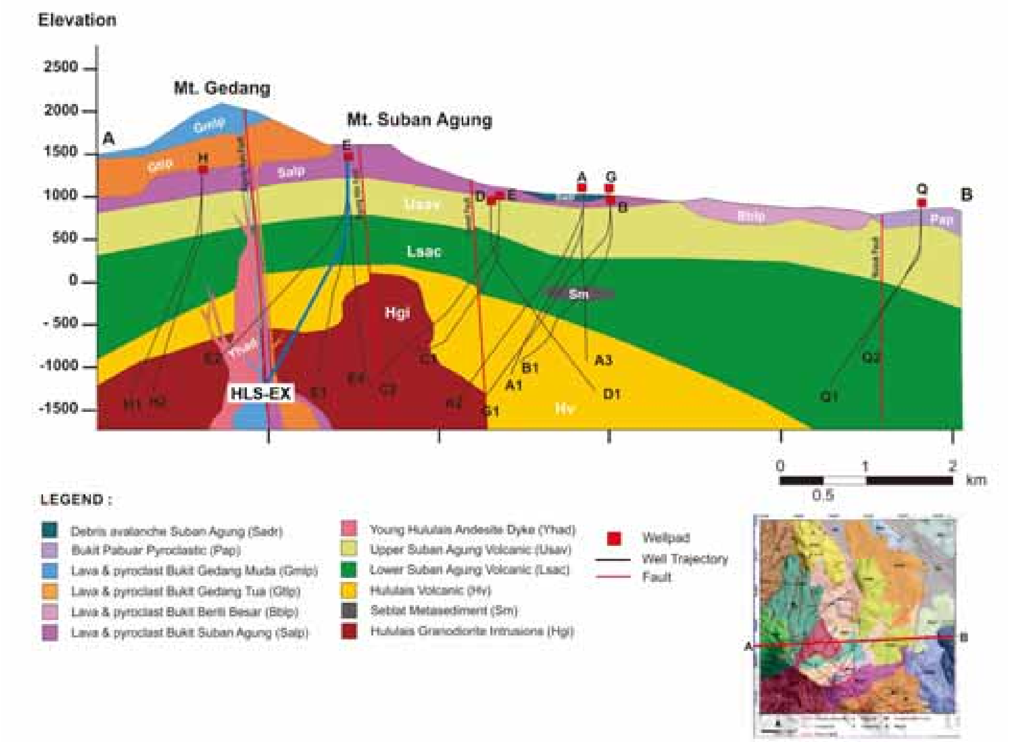

Figure 2.6 Subsurface rock formations in Hululais geothermal field. Trajectory of well HLS-EX is shown in a blue line (Pratama et al., 2021).

2.3 Hululais geothermal system

The magnetotelluric (MT) survey detects a low resistivity zone extending at the shallow depth upon a high resistivity zone at a deeper depth that characterized the prospective area in the Hululais geothermal field (Figure 2.7). A low resistivity zone at depth 325 masl extends on the southwestern part with an NW-SE trend. The low resistivity zone was estimated to represent the maximum prospect area of about 84.5 km^2 (PT Pertamina Geothermal Energy in The Ministry of Economy, Trade and Industry Indonesia, 2011).

The high resistivity zone is apparent at elevation 675 masl. The high resistivity zone determines the minimum prospect area, about 22.9 km^2. Reservoir thickness was estimated based on the appearance of the high resistivity zone and the bottom surface of the numerical model from 500 to 3,500 m thickness (PT Pertamina Geothermal Energy in The Ministry of Economy, Trade and Industry Indonesia, 2011).

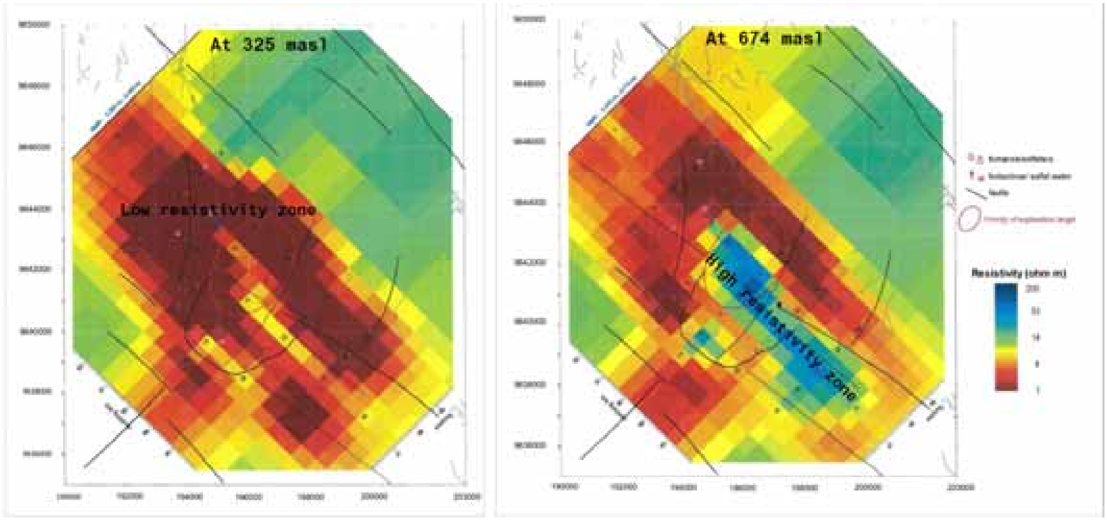

Figure 2.7 Resistivity map at 325 and 674 masl shows the low and high resistivity zone estimated as the prospective areas in Hululais geothermal field (PT Pertamina Geothermal Energy in The Ministry of Economy, Trade and Industry Indonesia, 2011).

The microearthquake monitoring recorded active seismicity within the Musi and Ketahun fault segments. The seismic hypocenters are located in the fault and fracture zones with a similar orientation to the NW-SE and some variation to the NE-SW direction (Juanda et al., 2015).

The seismicity, structural geology, and thermal manifestation distribution fit within the regional NW-SE lineament in Hululais (Figure 2.8). The hypocenter was identified to be around 1 to 10 km in depth (Juanda et al., 2015).

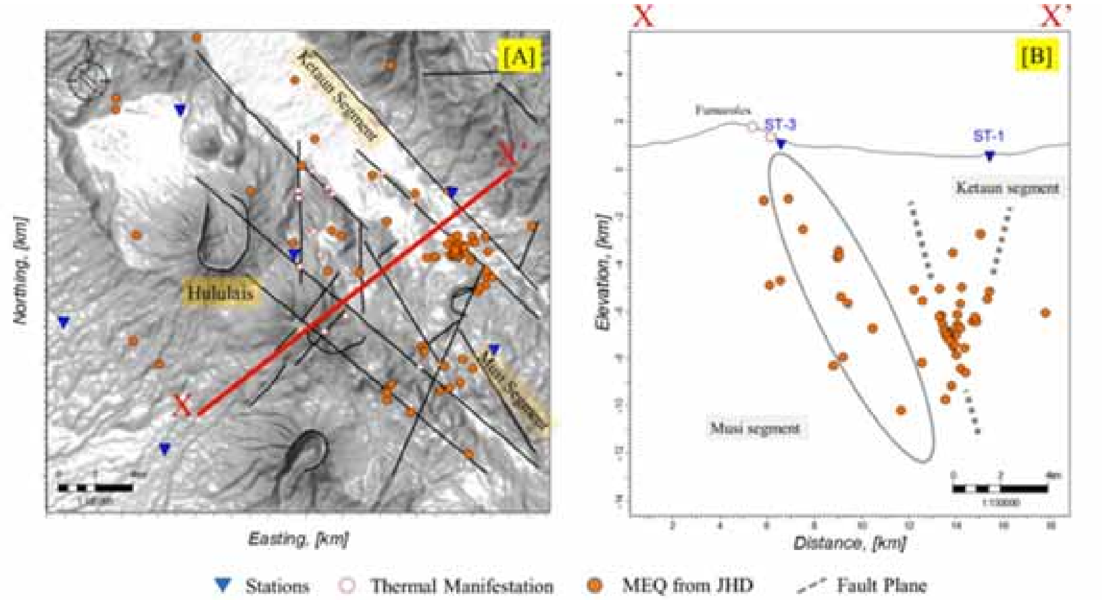

Figure 2.8 The microearthquake distribution map shows the epicenter points, structural geology, and thermal manifestations in the Hululais area [A]. The cross-section shows the hypocenter distribution identified at depths of 10 to 10 km [B] (Juanda et al., 2015).

The Hululais geothermal field is a water-dominated system. The flow of the hydrothermal fluid is mainly controlled by the NW-SE and NNW-SSE fault patterns. The Agung Hulu and Agung Hilir faults are the two major reservoir conduits encountered in the production feedzone from the boreholes in well pads A, C, E, and G. The surface thermal manifestations, geological structure, well trajectory, and subsurface conceptual model of the Hululais geothermal field are presented in Figure 2.9.

As depicted in Figure 2.9, the upwelling zone of the Hululais geothermal system was estimated beneath the Mt. Suban Agung crater complex. The hydrothermal fluid was manifested as a 95 – 98 °C steam vents complex, neutral pH hot springs with a 50 – 83 °C, and steam-heated water at 70 – 85 °C, associated with acid rock alteration (Budiardjo et al., 2001).

The hydrothermal fluid flows northward of the upwelling zone. It was exposed as an acid sulfate (SO_4) fluid at the Suban Gregok hot mud pool with a temperature of 70 – 83 °C.

Further north, the hydrothermal fluid emerged on the surface as sulfate bicarbonate (HCO_3 – SO_4) water with decreasing temperature of 35 to 45 °C in the Mt. Cemeh area. Finally, it appeared as sodium chloride bicarbonate ($NaCl$ – HCO_3) water in the Semelako hot springs complex. The water temperature in this area is about 40 to 70 °C, at an elevation of 400 – 550 masl (Figure 2.9).

Na-K-Ca solute and D'Amour-Panichi gas geothermometer were used to estimate the reservoir temperature of the system. The result indicates that the minimum subsurface reservoir temperature of the Hululais geothermal system falls between 240 to 300 °C (Budiardjo et al., 2001). Furthermore, the reservoir temperature measured from the borehole of HLS-EX reached 258 °C in its convective zone (PT Pertamina Geothermal Energy, 2018).

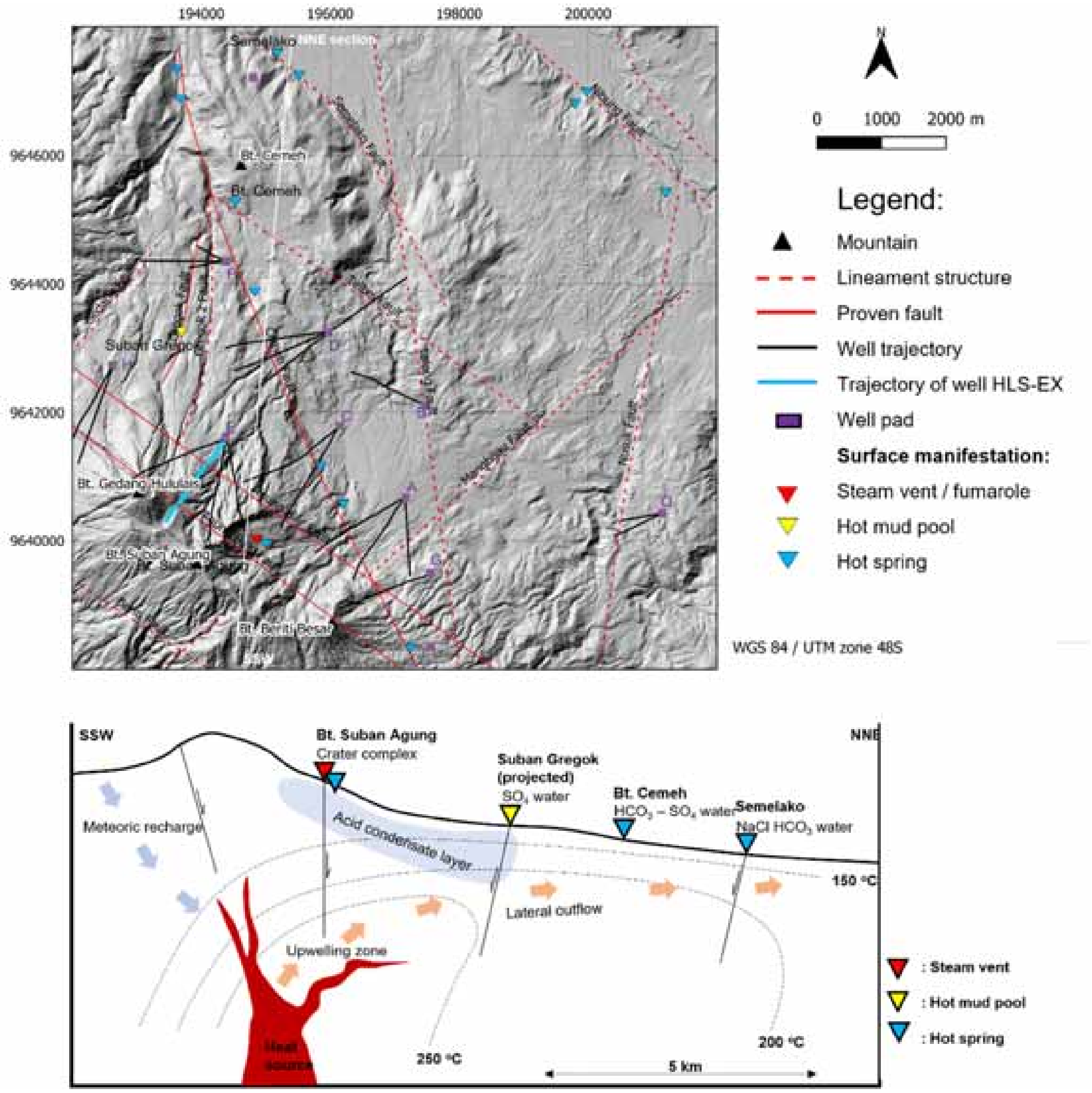

Figure 2.9 The surface thermal manifestation, structural geology, and conceptual model of the Hululais geothermal field (modified from Budiardjo et al., 2001).

The reservoir rock in the Hululais geothermal system is associated with the andesitic lava and fractured granodiorite intrusion body (Figure 2.6). Hydrothermal alteration in the Hululais geothermal field is generally divided into the smectite zone, transition zone, illite – epidote zone, and secondary biotite zone (Figure 2.10). Chlorite, secondary quartz, wairakite, calcite, anhydrite, actinolite, titanite, epidote, and secondary biotite are alteration minerals commonly found in this field (Koestono et al., 2015).

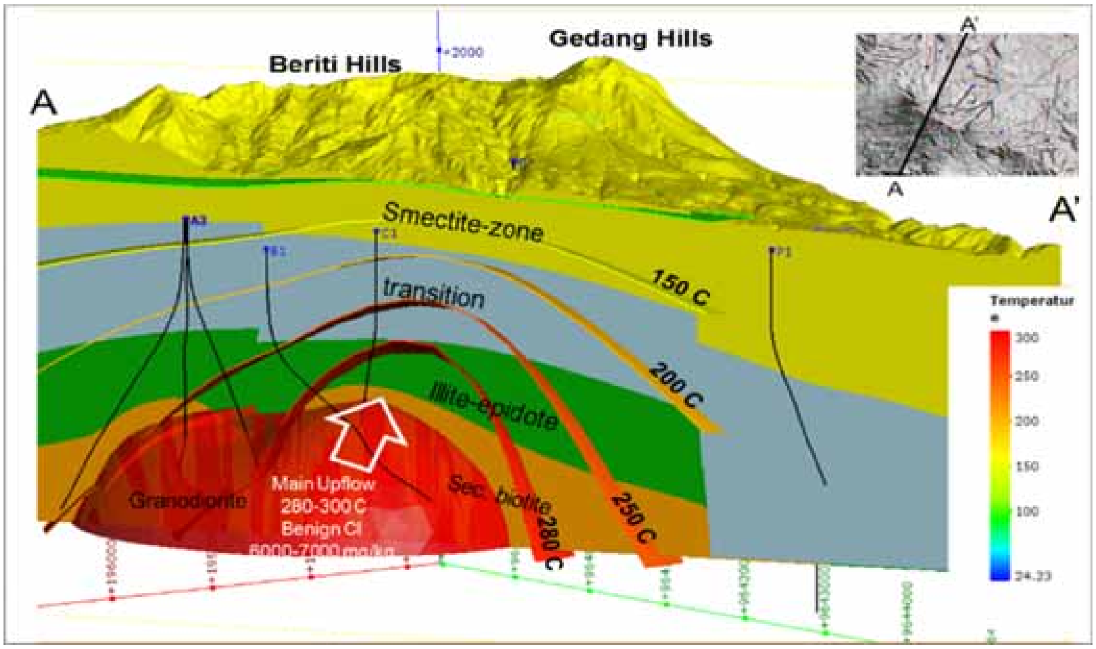

Figure 2.10 Hydrothermal alteration zone in Hululais geothermal field (Nusantara et al., 2017).

The top of the reservoir zone of the system is estimated at 1000 masl (Koestono et al., 2015). The primary feed zone in the wells from well pad E was approximately encountered at an elevation of 100 masl. Furthermore, the well transmissivity on well clusters C and E is found to be the highest among the wells in the production area. It ranges from 15 to 30 Dm, categorized as a good permeability well (Arifin et al., 2020).

3 Drilling of well HLS-EX

The high-temperature geothermal well HLS-EX is located on well pad E of the Hululais geothermal project. Well pad E is located at 1,397 masl. Drilling started on 19th June 2017 and was completed after 124 days of operation on 20th October 2017. HLS-EX was drilled to extract the benign hydrothermal fluid from 260 to 295 °C. The NW-SE fractures from the Suban Agung Hulu and Suban Agung Hilir faults are the main permeability target of the drilling (Figure 3.1).

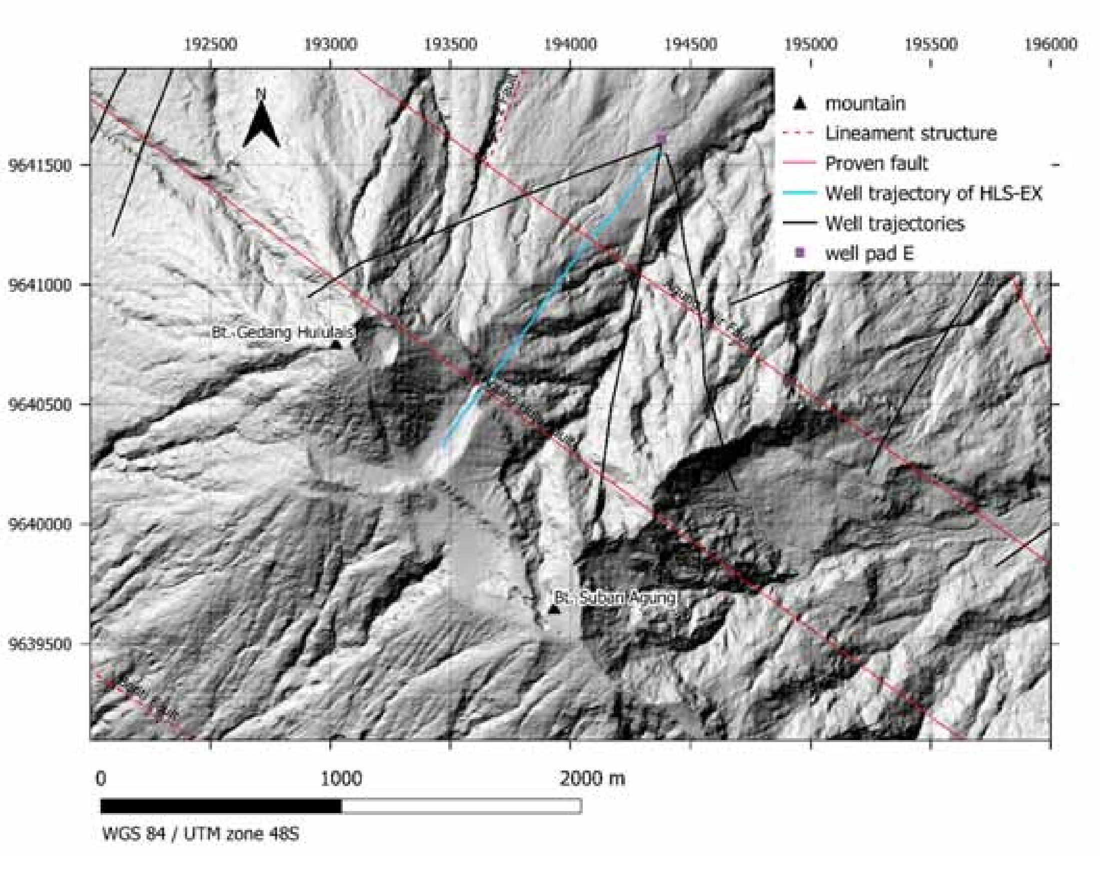

Figure 3.1 Trajectory map of well HLS-EX (modified from PT Pertamina Geothermal Energy, 2018).

HLS-EX was designed as a directional well to meet the drilling target. The actual well configuration of HLS-EX attained the borehole azimuth to N 203 °E, inclination around 38°, kick-off point (KOP) at 645 m, end of built (EOB) at 1,114 m, and reached the total measured depth of 3,280 m or equivalent to 1,355 m below sea level. The depth reference point of well HLS-EX is calibrated to the surface ground level. The well configuration of HLS-EX is illustrated in Figure 3.2.

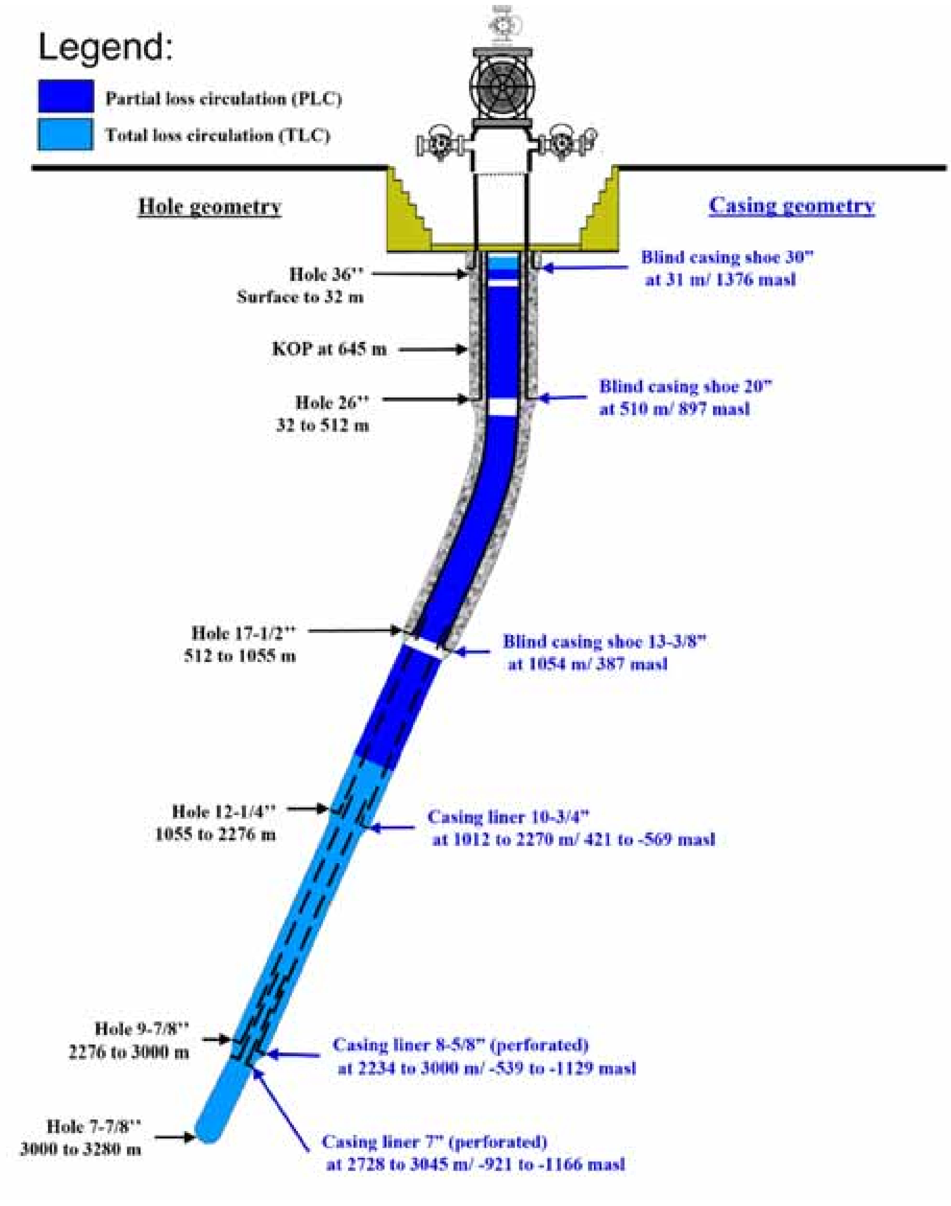

Figure 3.2 Well configuration of HLS-EX (PT Pertamina Geothermal Energy, 2018).

3.1 Drilling phase 1: hole 36” (10–32 m)

Phase 1 is the drilling from 10 to 32 m below the surface with a 36” drill bit. A total loss circulation (TLC) zone was encountered while drilling from 26 to 32 m. Stove pipe 30” was set from the surface to 31 m depth (casing shoe 30”). The circulation loss rate is measured in barrel per minute (BPM).

3.2 Drilling phase 2: hole 26” (32–512 m)

In drilling phase 2, three 26” drill bits were used. While drilling, a mud motor and a measured-while drilling (MWD) tool were used. Drilling fluid freshwater has been used while adding potassium chloride (KCl) and polymer mud. The concentration of KCl in the mud ranges from 1 to 2.2%.

Circulation losses were hit from 32 to 512 m (Table 3.1). Around 973 barrels of cement slurry was used to cure the circulation loss, then added the loss circulation material (LCM) and plugging material such as palm fiber, and bentonites. According to the drilling program, casing 20” was cemented from 32 to 510 m depth.

Table 3.1 Loss of circulation zones in the drilling of phase 2.

Partial loss circulation zone	
Depth (meter)	**Loss rate (barrel per minute)**
55 – 63	6 – 8
63 – 67	0.5
82 – 512	0.1 – 14

Total loss circulation zone	
Depth (meter)	**Loss rate (barrel per minute)**
32 – 55	≥ 14 – 19
67 – 70	≥ 18
91	≥ 18
120	≥ 18
145	≥ 18

3.3 Drilling phase 3: hole 17½” (512–1055 m)

At the beginning of drilling phase 3, the casing drop problem and hoisting system maintenance delayed the drilling progress. The 20” casing was detached from its connection and detected from the cement chips mixed with metal flakes at 272 m. This obstruction was resolved by re-cementing, milling, reaming down, and cleaning the hole with a junk basket and fishing magnet.

Formation drilling was continued from 512 to 1055 m with a steerable bottom hole assembly (BHA) and two 17½” bits. Polymer mud and LCM were used in this interval. The loss circulation zone in this drilling stage is summarized in Table 3.2.

Table 3.2 Loss of circulation zones in the drilling of phase 3.

Partial loss circulation zone	
Depth (meter)	**Loss rate (barrel per minute)**
590 – 593	0.3 – 20
593 – 783	0.3 – 1.7
788 – 872	1 – 2.7
872 – 1016	2 – 3.5
1017 – 1054	2 – 3.5
1055	8 – 11

Total loss circulation zone	
Depth (meter)	**Loss rate (barrel per minute)**
593	20
783	21
872	13

Casing 13⅜” was cemented from the surface to 1054 m (production casing shoe). Wireline logging was performed from the surface to 1049 m to evaluate the cement bonding quality. The result indicates a good cement bonding within the annulus.

3.4 Drilling phase 4: hole 12¼” (1055–2276 m)

The depth interval 1055 to 2276 m was drilled with steerable BHA and six 12¼” bits. Aerated drilling was started at 1476 m, and water polymer mud drilling was performed from 1055 to 1826 m. Freshwater drilling was done in the interval from 1826 to 2276 m, in which the reservoir zone was estimated. The loss of circulation zones in this section are shown in Table 3.3. A perforated casing liner 10¾” was successfully set at 2,270 m, with the top of liner at 1012 m.

Table 3.3 Loss of circulation zones in the drilling of phase 4.

Depth (meter)	**Loss rate (barrel per minute)**	**Loss zone type**	**Drilling method**
1076 – 1476	0.2 – 0.5	PLC	Gel polymer mud
1476 – 1846	1 – 6	PLC	Aerated mud
1846 – 1936	5 – 14	PLC	Aerated water
1936 – 2276	> 20	TLC	Aerated water

Note: PLC: Partial loss circulation, TLC: Total loss circulation (no return).

3.5 Drilling phase 5: hole 9⅞” (2276–3000 m)

Hole 9⅞” was drilled in TLC condition with aerated water from 2276 to 3000 m. Blind drill was performed with a 9⅞” drill bit and two 9⅞” polycrystalline diamond compact (PDC) drill bits. An electronic Multi-Shot (EMS) survey obtained the borehole geometry in 2964.34 m measured depth is 4.33 m on the right and 3.83 m below the planned well design. Hole inclination is 37.63°, azimuth N 219.10° E, and total vertical depth is 2508.57 m.

Wireline logging was performed after reaching the total depth for this drilling phase. The wireline logging included the caliper, pressure and temperature, dipole sonic imager (DSI), the formation micro imager (FMI), and resistivity. In addition, sidewall coring in the open hole section was carried out. Finally, the shoe of 8⅝” perforated liner was set at 3000 m, with the top of liner at 2234 m.

3.6 Drilling phase 6: hole 7⅞” (3000–3280 m)

Interval 3000 to 3280 m was drilled with two 7⅞” drill bits and rotary BHA. Depth progress continued to drill in TLC condition with aerated water. Drilling stalls occurred at 3110, 3112, 3122, 3125, 3213, and 3280 m. Due to the high drilling torsion and stall problems, the total depth (TD) of the well was decided at 3280 m, 20 m shallower than the planned well design.

An attempt to perform an FMI logging in the open section was done but failed due to the limited tool dimension and clearance area inside the casing. The tool was stuck at 2552 m.

Pressure and temperature logging was conducted while injecting 700 GPM of freshwater through the annulus in TLC conditions. The maximum temperature recorded from the well is 120.39 °C, and the maximum measured pressure is 18.49 MPa at 3270 m. The fluid level was identified at 397 m. The DSI logging successfully covered the open hole section, and the result indicates the presence of high fracture intensity around 3200 to 3212 m.

The EMS survey yielded the position of the actual borehole at 3193 m measured depth is 6.36 m on the left and 9.21 m below the planned borehole design. Hole inclination is 37.95°, azimuth to N 207.24° E, total vertical depth is 2689 m. Projected well geometry at 3280 m measured depth was estimated based on the measurement at depth 3193 m. It is estimated that the well has 37.95° inclination and azimuth to N 207.24° E at the TD well.

The 7” perforated casing liner sits on 3045 m. Finally, the casing was released at 3045 (casing shoe), and the top of liner was located at 2728 m, continued with the well completion. The drilling progress curve resumed the drilling phases of well HLS-EX (Figure 3.3).

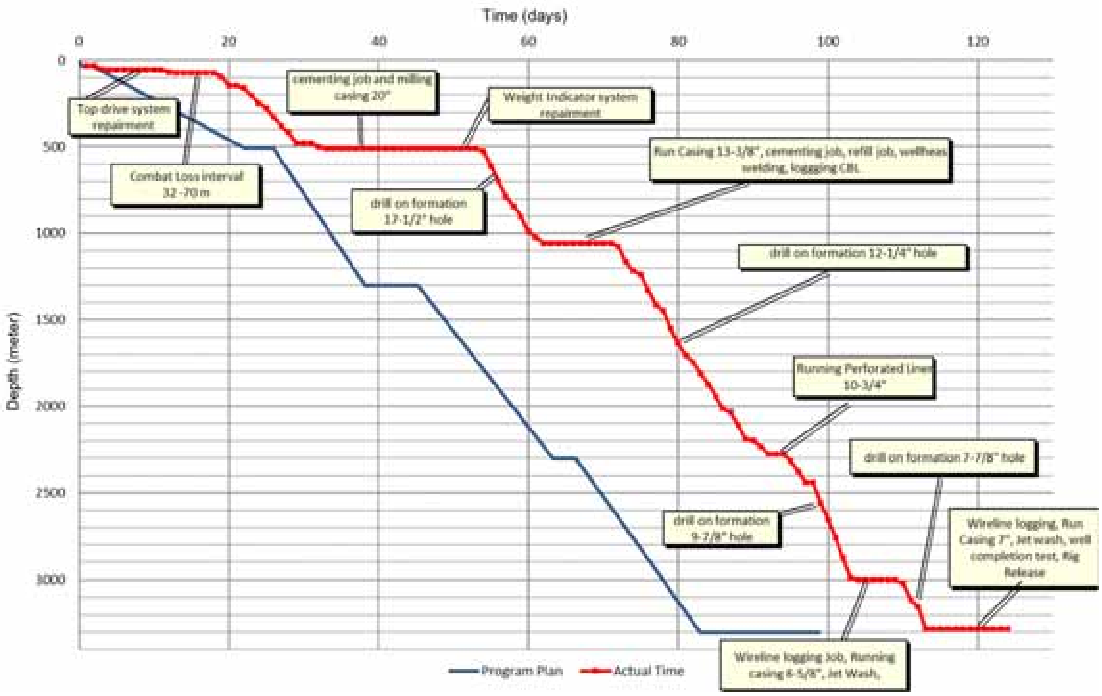

Figure 3.3 Drilling progress curve HLS-EX (modified from PT Pertamina Geothermal Energy, 2018).

4 Sampling and analytical method

4.1 Sampling

Drill cuttings and cores from HLS-EX are used as the primary data source in this study. The samples are analyzed through several methods according to different objectives. Drill cutting samples of HLS-EX are available from 10 – 1937 m, in an interval of 3 m.

The TLC started from 1937 until 3280 m (TD well). In the TLC zone, nine sidewall core (SWC) samples were retrieved at depths 2280, 2285, 2286, 2290, 2300, 2400, 2420, 2440, and 2500 m. In total, twenty-six thin sections from drill cutting and all SWC samples are available.

4.2 Analytical method

4.2.1 Stereomicroscopic analysis

Stereomicroscopic analysis is a fast method to identify texture and rock type on a microscopic scale. It has been done onsite by wellsite geologists and re-examined again in the laboratory for a more detailed investigation in this study. The examination was performed using an Olympus SZ61 stereo microscope at the Institute of Earth Sciences, University of Iceland. The microscope is equipped with a digital camera type SC50, which allows image documentation via the OLYMPUS Stream Start software. The magnification used in this observation is up to 35x.

In stereomicroscopic analysis, the physical properties of the rock samples were observed, both in drill cutting and core. The examination observed the visible parameters such as color, rock texture, grain size and contact, sorting, crystal shape, luster, alteration rank and intensity, veins density, and composition abundance of the minerals and rocks in the samples. Composition abundance is measured semi-quantitatively and classified into five categories in Table 4.1.

Table 4.1 Scoring classification for mineral abundance.

Rank	**Qualitative score**	**Quantitative**
0	Absence	none
1	Trace	0 - 2%
2	Rare	2 - 5%
3	Common	5 - 15%
4	Abundant	> 15%

In visual, the percentage abundance estimation needs to be consistently calibrated using the comparison charts illustrated in Figure 4.1.

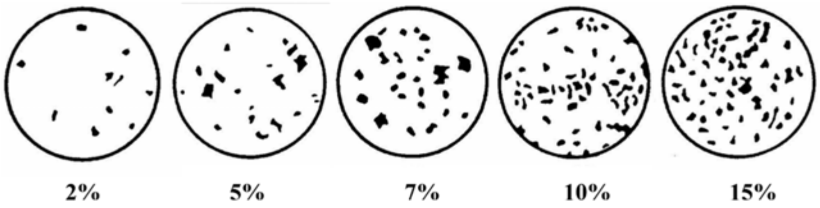

Figure 4.1 Comparison charts for visual estimation of mineral percentage in drill cutting sample (Baker Hughes INTEQ, 1996).

A table of standard descriptive parameters is established to observe drill cutting samples based on texture, grain size, brittleness, crystallinity, and rock fabric. This table adapts the rock identification approach by Whitman et al. (1906), McPhie et al. (1993), and Baker Hughes INTEQ (1996) that was modified to be applied in drill cutting samples (Table 4.2).

Table 4.2 Descriptive feature to identify rock type in drill cutting sample.

Descriptive feature of drill cutting	**Effusive process**		**Explosive process**	
	Intrusions and coherent lava		**Consolidated pyroclastic deposits**	
	Intrusion	**Coherent lava**	**Pyroclastic tuff**	**Volcanic breccia**
1. **General texture**	Crystalline, porphyritic, and non-vesicular.	Crystalline, porphyritic, massive, flow foliated, spherulitic, vesicular, pumiceous, or scoriaceous.	Fragmental, aphanitic, glass shard, vesicular, pumiceous, or scoriaceous.	Fragmental, consists of more than one type of volcanic clasts.
2. **Grain size:** The magnitude of crystal or volcanic material in the rock mass.	Coarse-grained rock. Crystal size greater than 5 mm.	Medium-grained rock. Crystal size is between 1 to 5 mm.	Fine tuff (1/16 mm) and coarse tuff (1/16 to 2 mm).	Tuff breccia or lapilli tuff (2-64 mm).
3. **Brittleness:** The tendency to easily break or deform into subtler fragments under stress.	Un-brittle, commonly found in larger chip fragments.	Moderately hard.	Easily broken and washed out by water.	A mix of solid resistance rock chips with clay size loose material.
4. **Crystallinity:** The degree of crystallization is measured by the relative number of crystals and glass, or in altered rock, the clay portion.	Holocrystalline to dominantly crystalline.	Hypo crystalline to dominantly glassy.	Extremely glassy to holohyaline.	Hypocrystalline to glassy. The fragments of tuff and lava are present in nearly equal portions.
5. **Rock fabric:** The arrangement of crystals and glassy parts in the rock. It is defined by measuring the relative number of phenocrysts and groundmass distribution.	It is dominated by coarse to medium size phenocrysts. It is present in euhedral to subhedral shape bounded by its crystal faces.	Fine-sized groundmass scattered through its coarse phenocrysts. The contrast between the sizes is observable as porphyritic fabric.	Rich in groundmass portion. Phenocrysts may be present in very fine sizes, mostly feldspar and quartz.	A mix of glassy tuff fragments and fine to medium-sized lava could be found in the same sample.
Note: The grain size of crystal minerals is categorized as very fine-grained for particles smaller than 0.1 mm, fine-grained for 0.1 – 1 mm, medium-grained for 1 – 5 mm, and coarse-grained for a material size greater than 5 mm. In pyroclastic tuff and volcanic breccia, the grain size description follows the classification suggested by Fisher (1961).				

4.2.1 Petrographic analysis

The optical properties of individual minerals and their textural relationships were examined using polarization microscopy. This study used an Olympus BX51 polarization microscope to analyze the available thin sections, at the Institute of earth Sciences, University of Iceland. A photomicrograph was obtained using an *Olympus UC30* microscope camera and software called *analysis-getIT*. The magnifications used in this observation vary from 40x, 100x, and 200x.

Observations were made under crossed polarized light (XPL) and plane-polarized light (PPL). Optical mineral properties such as color, pleochroism, relief, interference color, cleavage, twinning, and extinction angle are identified to determine minerals and mineral sequences. Moreover, the texture was observed to determine the rock types.

Eighteen drill cutting thin sections were examined from depths 65, 152, 350, 452, 551, 650, 749, 851, 950, 1052, 1151, 1250, 1352, 1451, 1550, 1652, 1751, and 1850 m. Eight sidewall core (SWC) thin sections were included in the observation derived from depths 2286, 2290, 2300, 2400, 2420, 2440, 2500, and 2550 m. A single SWC sample from depth 2285 m was not prepared for the thin section analysis assuming it still represents the same rock type as the sample from 2286 m.

4.2.2 Inductively coupled plasma-optical emission spectrometry (ICP-OES) analysis

Inductively coupled plasma-optical emission spectroscopy (ICP-OES) measured the bulk major and selected trace element contents. Sample preparation and analysis were performed at the Institute of Earth Sciences, University of Iceland. In this study, sixty drill cutting samples were prepared for ICP-OES analysis. The samples were selected from several depths representing different rock types with different alteration intensities (Appendix A).

The samples were crushed into a fine powder (size <2 μm) and stored in vials. Each powdered rock sample mass was measured and mixed with lithium metaborate ($LiBO_2$). About 0.1 g of the powdered sample was mixed with 0.2 g of $LiBO_2$ powder in a graphite crucible. Afterwards, the standard samples (A-THO, B-THO, B-ALK, BCR-1, and B-HVO-1) were prepared similarly. Each 0.1 g standard sample was mixed with 0.2 g $LiBO_2$. At the end of this stage, each rock sample and the standard sample were put into a graphite crucible and ready to be melted.

In total, sixty-five samples (including the five standard samples) were melted inside a Thermo scientific Lindberg/Blue vacuum furnace for ± 30 minutes at a temperature of 1000 °C. This process melted the samples to form glass beads. Every glass bead was dissolved with 20 g of the acid solution containing 5 vol% HNO_3, 1.33 vol% HCl, and 1.33 vol% of saturated $H_2C_2O_4$. The dissolution was done overnight by putting the sample solution into plastic bottles mounted onto a rotating rack. All the sample preparation stage for ICP-EOS analysis is pictured in Figure 4.2.

Figure 4.2 The ICP-OES sample preparation includes the process of sample selection from the cutting charts, the blue dots represents depth samples selected for ICP-OES and yellow dots for thin section analysis (a-b), sample powder making using an agate mortar pestle (c), sample storing inside the vials (d), sample and lithium metaborate mixing in a graphite crucible (e), the melting process (e-g), cooling down the melt to form glass beads (h), glass bead and acid solution mixing in a plastic bottle (i), dissolution in a rotating rack (j), and arranging dissolved samples on the instrument sample holder prior measurement (k).

The concentration of major and trace elements in this study was analyzed using the Thermo Scientific™ iCAP™ 7400 ICP-OES equipment at the Institute of Earth Sciences, University of Iceland. Major elements measurements include SiO_2, Al_2O_3, FeO, MnO, MgO, CaO, Na_2O, K_2O, TiO_2, and P_2O_5 (in wt.% unit). Trace element concentration including Ba, Co, Cr, Cu, Ni, Sc, Sr, V, Y, Zn, and Zr is acquired in µg/g unit. Additionally, the standard samples were run for instrument calibration. The accuracy in the measurement process was calibrated with standard samples, and each element has different accuracy that is reflected in the value of standard error as presented in Table 4.3.

Table 4.3 Instrumental standard error for elements in the ICP-OES analysis

Element	**Unit**	**Instrument**	**Standard error (2σ)**
SiO_2	wt.%	ICP-OES	0.26
Al_2O_3	wt.%	ICP-OES	0.14
FeO	wt.%	ICP-OES	0.08
MnO	wt.%	ICP-OES	0.00
MgO	wt.%	ICP-OES	0.25
CaO	wt.%	ICP-OES	0.20
Na_2O	wt.%	ICP-OES	0.08
K_2O	wt.%	ICP-OES	0.15
TiO_2	wt.%	ICP-OES	0.01
P_2O_5	wt.%	ICP-OES	0.02
Ba:	µg/g	ICP-OES	7.94
Sc	µg/g	ICP-OES	0.99
Sr	µg/g	ICP-OES	5.94
V	µg/g	ICP-OES	14.02
Y	µg/g	ICP-OES	0.85
Zr	µg/g	ICP-OES	4.07

Note: The standard error was measured in wt.% for major elements and µg/g for the trace elements.

The major element concentration was normalized to a volatile-free basis and plotted into the total-alkali-silica (TAS) diagram modified from Le Bas et al. (1986) to determine the rock type based on its chemical composition. The bivariate plots were produced using Python scripting language and can be accessed through https://github.com/vividewi/altrock_plots.git. The plots were designed to take into account three essential parameters: (1) the elements concentration, (2) rock texture, and (3) alteration intensity.

4.2.3 Loss on ignition (LOI) analysis

Loss on ignition (LOI) measures the volatile content from sample weight in several ignition tests. The moisture in the rock composition is related to mineral characteristics. Thus, heating the rock sample into several temperature stages will affect the sample weight due to dehydration. In practice, heating the rock sample to 110 °C will remove the H_2O constituent from its clay layers and the surface moisture. In higher ignition to 530 and 800 °C, the OH and CO_2 will be released from the rock sample (Kohno et al., 1993). This measurement used an analytical balance scale type Mettler Toledo AT 250 with a precision of 0.01 mg.

Sixteen samples were selected for the LOI analysis. The LOI samples were picked based on their chemical composition analyzed by the ICP-OES (inductively coupled plasma-optical emission spectrometry). The samples representing the highest and lowest alteration intensity and the outliers in alkali, SiO_2 content, and calcium contents, are picked to be analyzed.

The sample was crushed to powder, placed in a clean ceramic crucible, and dried inside an oven for over twenty-four hours at 110 °C to remove surface moisture from the sample. Keeping the sample in dry condition during the LOI analysis is essential. Therefore, it is important to avoid physical contact with the sample to prevent moisture contamination. After 24 hours, the weight of the empty crucible and the sample were carefully measured at room temperature condition. In this first weight measurement, the sample amount at room temperature was approximately 1 g.

The dehydration rate increase within a short time and reaches a plateau within 6 – 12 hours (Kohno et al., 1993). Therefore, the heating period within 24 hours is considered appropriate. The color of the sample would slightly change to reddish and light brown due to the oxidation process during the gradual heating up (Kohno et al., 1993).

After drying, the sample was put in the furnace to be heated at 600 °C overnight. Afterward, the sample was removed from the furnace, cooled down to room temperature, and measured again. In this second weight measurement, the sample weight at 600 °C was obtained. After the sample weight at 600 °C has been recorded, the sample was placed back in the furnace at 800 °C for 6 hours.

After 6 hours, the sample was removed and cooled down again to room temperature. The weight of the sample was measured and recorded as the sample weight at 800 °C. The percentage of total LOI was calculated by using the formula below.

$$Total\ LOI\ (\%) = \left(\frac{weight\ at\ room\ temperature\ (g) - weight\ at\ 600\ ^\circ\mathrm{C}\ (g)}{weight\ at\ room\ temperature\ (g)} \times 100\%\right)$$

$$+$$

$$\left(\frac{weight\ at\ 600\ ^\circ\mathrm{C}\ (g) - weight\ at\ 800\ ^\circ\mathrm{C}\ (g)}{weight\ at\ 600\ ^\circ\mathrm{C}\ (g)} \times 100\%\right)$$

4.2.4 X-ray diffractometry (XRD) analysis

X-ray diffractometry (XRD) analysis was conducted to quantify the clay minerals. In this study, five samples were treated and measured in three conditions: air-dried or untreated, ethylene glycol added, and heated to 550 °C.

The first step of XRD analysis was to wash each sample carefully in the deionized water and put about 2 g of rock cutting sample in a glass test tube. Each tube was filled with deionized water, closed with a rubber stopper, and put in a mechanical shaker. The sample was shaken for about four hours. The suspended clay slurry is left to settle for about ten minutes and then transferred onto a circular glass slide using a pipette. The sample was left to dry at ambient temperature and humidity. The sample was measured after complete drying. The measurement result in this stage represents an untreated condition (code: UNT, untreated).

After the untreated measurement, the sample was placed inside a closed desiccator above a container filled with ethylene-glycol. The sample was left in the ethylene-glycol fume for twenty-four hours and then measured. This measurement states the glycolated condition (code: GLY, glycolated). Finally, the sample was heated in a furnace for about one hour at 550 °C. After the sample was cooled down, the heated condition was measured (HIT, heated). The set of three measurements was then viewed superimposed using a software for X-ray diffraction data display.

The glass slide is secured with soft putty in a back-loaded steel sample holder during the measurement process. Each sample was measured using a parameter file ranging from $2\theta = 2°$ to $2\theta = 65°$ with high resolution. Background radiation was not subtracted, and the patterns were not smoothed. A Malvern Panalytical Empyrean diffractometer in the Institute of Physical Sciences, University of Iceland, was used (Bragg-Brentano goniometer), with spinner assembly, Ni-filtered Cu-ka radiation at 1.54 Å wavelength at 40 mA and 45 kV, with automatic (variable) slits and PIXcel 3D solid-state detector. The data was interpreted by superimposing and viewing the 2θ at the 2 - 14° range of the three differently treated components of the sample.

4.3 Drill cutting limitation

Analytical errors in drill cutting analysis could occur due to the instrument, sample, and human control limitations. Additionally, a drilling rig is not an ideal clean laboratory; thus, there is always a risk of contamination in drill cuttings. It is necessary to address the limitation of the drill cutting samples in the analysis to obtain high accuracy and reliability in the result.

Drill cuttings from well HLS-EX are retrieved with fine-grain size, from less than 1 mm to 5 mm. Due to its fine grain size, it is challenging to identify rock types from drill cuttings. Some textures like amygdales, cavities, cross-cutting relations, and veins that have been destructed in the drill cutting are difficult to observe.

Drill cutting may not represent the rock from which they derive. The softer material may be washed away, and only the more rigid material is retrieved at the surface. Mixed cutting from deeper and shallower depths could be collected simultaneously. Mixing is often associated with formation collapsing during drilling (Browne, 1984). Formation collapse also appear as irregular cutting size. In some cases, the gravel to boulder sized rock fragments are found to be mixed with sand-sized cuttings at the same depth. The collapsing formation depths could be identified and measured by the caliper log.

Naming the hydrothermally altered rock in the scale of drill cutting for this study follows the standard system that has been made by McPhie et al. (1993). In this system, the hydrothermally altered rock is divided into the coherent lava and intrusion type, and the volcaniclastic deposit type (see Figure 4.3).

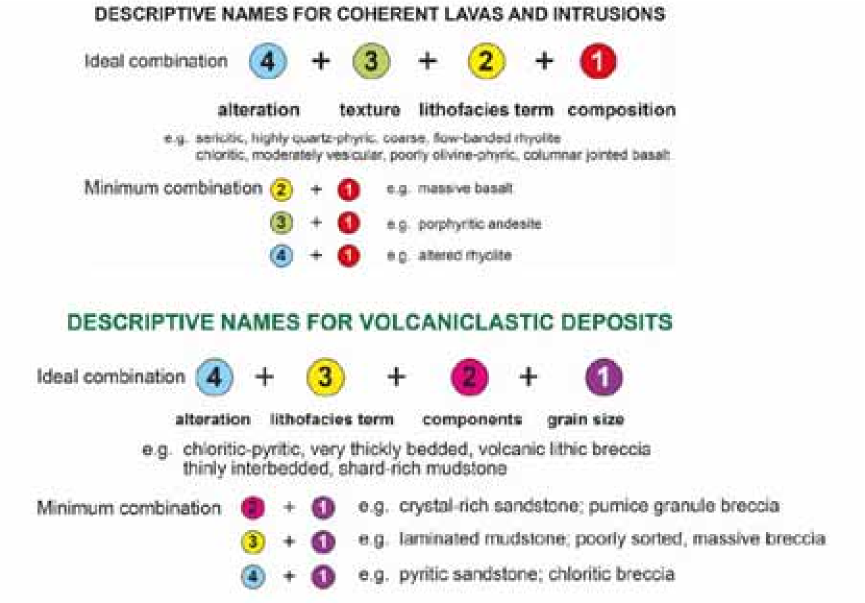

Figure 4.3 Adapted naming system for hydrothermally altered rocks in drill cutting observation (McPhie et al., 1993).

Essential descriptive points in the naming system proposed by McPhie et al. (1993) are composition/component, lithofacies, texture, alteration, and grain size. Lithofacies provides information at the outcrop scale in the field, such as structures and geometry that are unobservable in drill cutting samples. Thus, the lithofacies term is not applied in this study.

Coherent volcanic textures form from the solidification of magma in lava and intrusions. It is manifested as porphyritic texture, especially in evenly distributed, euhedral crystals with a narrow size range. Aphyric, aphanitic, and glassy may also be coherent. Chemical composition is emphasized in naming the lava and intrusions (McPhie et al., 1993).

The term volcaniclastic is descriptive and applies to deposits composed predominantly of volcanic particles. The grain size classification from Fisher (1961) is adapted in naming the volcaniclastic deposits. However, grains larger than 2 to 6 mm are challenging to identify in drill cutting.

5 Results

5.1 Rock types

The stereomicroscopic and polarization microscopy examination distinguished the rock cuttings and cores in well HLS-EX into four textural groups. These are coherent lava, intrusions, tuff, and volcanic breccia. Rock composition was determined by combining ICP-OES measurements and qualitative counts of the mineral percentage in petrographic analysis. In total, eight different rock types were identified in well HLS-EX. It includes andesitic and dacitic lava, intrusion of basaltic diorite, diorite, and granodiorite, andesitic and dacitic tuff, and volcanic breccia (Table 5.1).

Table 5.1 Rock types in well HLS-EX.

Texture	Composition		Rock type
Coherent lava	Basaltic andesite, andesite, and dacite	1	Lava andesite
		2	Lava dacite
Intrusions	Basaltic andesite, andesite, and granodiorite	3	Basaltic diorite
		4	Diorite
		5	Granodiorite
Tuff	Andesite and dacite	6	Andesitic tuff
		7	Dacitic tuff
Volcanic breccia	The mixture from andesitic to dacitic	8	Volcanic breccia

Note:
See Figure 5.8 and Appendix B for the distribution depths along the borehole

5.1.1 Coherent lava group

The coherent lava group is characterized by its porphyritic texture. The phenocrysts are composed of crystal grains in size 0.1 – 1.5 mm, dominantly plagioclase and clinopyroxene. Volcanic glass dominates the groundmass (hypohyaline). Coherent lava is divided into andesite and dacite types based on its chemical composition. The ICP-OES plots thirty-five lava samples of well HLS-EX into three compositional types (Figure 5.14). Twenty-eight lava samples were defined as andesite, two basaltic andesites, and five dacites. Accordingly, the andesite and basaltic andesite are classified as lava andesite. Meanwhile, lava dacite has no compositional variation.

Lava andesite is white, grey, light grey, dark grey, black, dark green to pale yellow. The coarser size of phenocryst grains generally distinguishes lava andesite from lava dacite. The phenocrysts are plagioclase and clinopyroxene with crystal sizes ranging from 0.1 to 1.5 mm. The groundmass is dominated by volcanic glass. Lava andesite is commonly associated with volcanic breccia in the upper part and intrusions in the deeper depths (Figure 5.8 and Appendix B).

Lava dacite has a lighter color than the other lava rocks, and it has colors from grey, light grey, and pale yellow to white. Fine-grained phenocrysts of feldspar plagioclase are common in lava dacite. Volcanic glass and fine-grained quartz build up the groundmass. Lava dacite is associated with volcanic breccia and dacitic tuff. The trachytic texture is frequently observed in andesitic and dacitic lava. Lava andesite and dacite in well HLS-EX are represented in Figure 5.1.

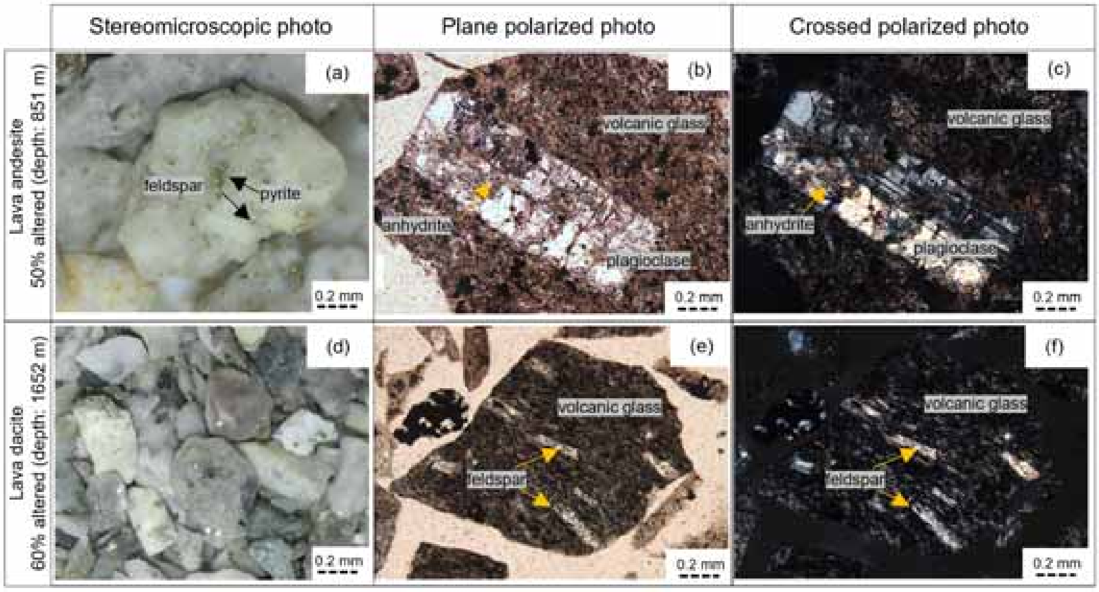

Figure 5.1 Lava andesite (a-c) and dacite (d-f) from the depth of 851 m and 1652 m.

5.1.2 Intrusions group

The intrusions group has holocrystalline and phaneritic textures. Intrusions are typically composed of crystal grains in size 0.2 – 2 mm in cutting samples. Meanwhile, the average grain size reaches 5 mm in the core samples. Observed minerals include plagioclase, K-feldspar, pyroxene, hornblende, quartz, and biotite with subhedral to euhedral crystal habit. The intrusion rocks are identified as basaltic diorite and diorite in cutting samples and granodiorite in core samples (Figure 5.2 and Figure 5.3).

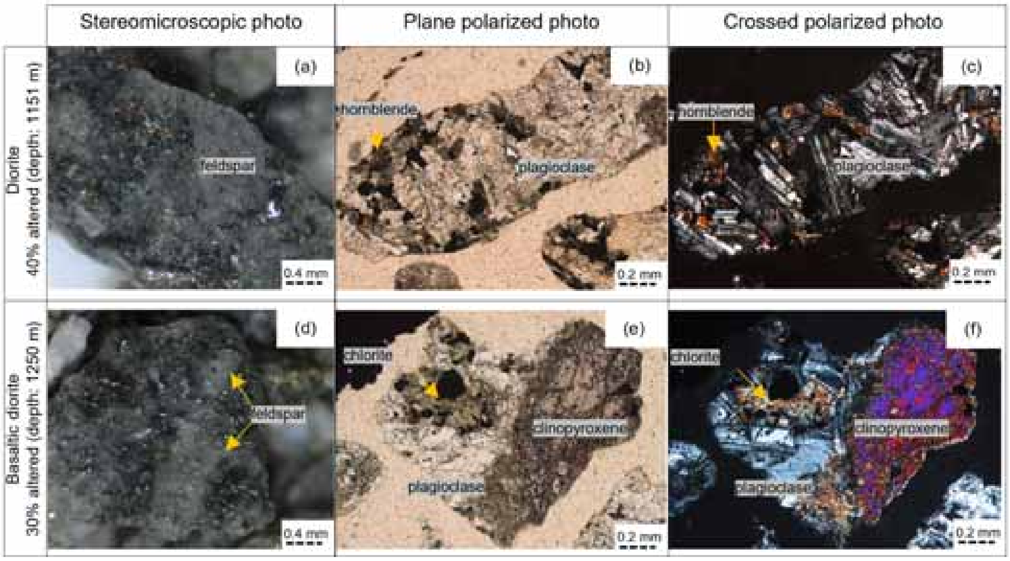

Figure 5.2 Basaltic diorite and diorite from drill cutting at 1250 and 1151 m.

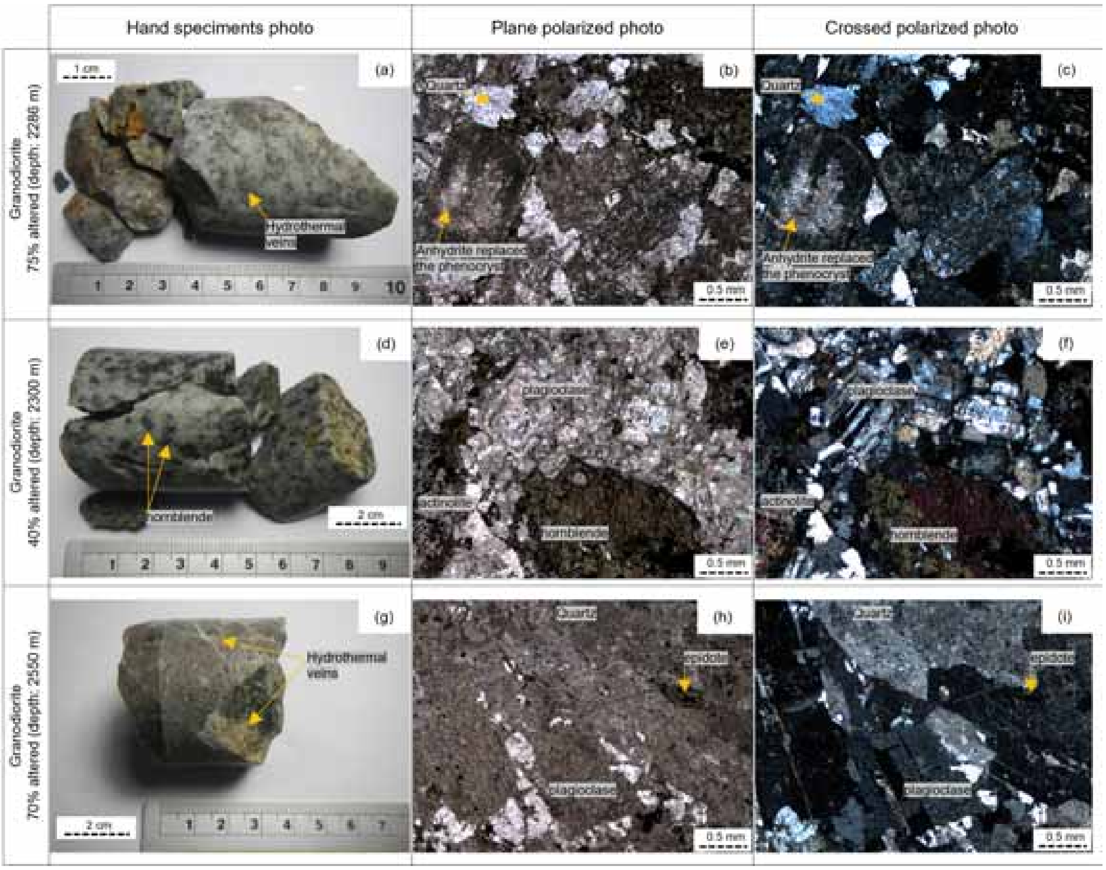

Figure 5.3 Granodiorite from the sidewall cores at 2286, 2300, and 2550 m.

Basaltic diorite appeared in grey, dark grey, dark green, to white-colored crystalline rocks with subhedral to euhedral crystals. Plagioclase and clinopyroxene appear in the average size of 0.5 – 2 mm, and 0.2 – 0.5 mm, respectively. Diorite and granodiorite were identified in grey, dark-grey, black, dark, green, and white colors. Textures are phaneritic to porphyritic. Phenocrysts are composed of plagioclase feldspar (0.3 – 1.5 mm), clinopyroxene (0.2 – 0.5 mm), hornblende (0.5 – 2.5 mm), and biotite (0.1 – 0.3 mm). The presence of primary quartz distinguishes granodiorite from the other intrusions (Figure 5.2 and Figure 5.3). Basaltic diorite is exclusively found in one interval depth, from 1223 to 1301 m (78 m thickness), and at 1757 m. Diorite was encountered as thin layers along the borehole associated with lava andesite. Granodiorite was identified from core samples depths 2286, 2290, 2300, and 2550 m.

5.1.3 Tuff group

The tuff group shows fragmental texture in the fine-grained (1/4 to 1/16 mm) pyroclastic material. The rock cuttings containing tuff are commonly brittle, have clay fragments, and are easily washed out by the water. Tuff composition in HLS-EX is classified as andesitic and dacitic tuff (Figure 5.4).

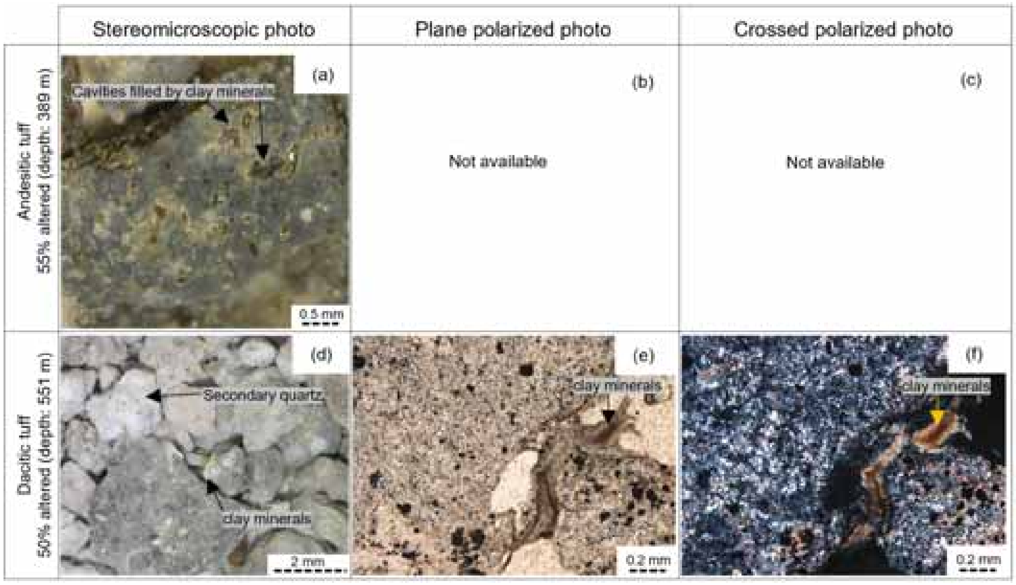

Figure 5.4 Andesitic and dacitic tuff.

Andesitic tuff generally has darker color than dacitic tuff, from light grey, dark grey, white, pale green, orange, red, and yellow. The andesitic tuff was distinguished by aphanitic texture in its volcanic glass, and the presence of clay minerals, sulfide minerals, and iron oxide. Andesitic tuff appeared fragmental, pumiceous, and highly porous with open vesicular features. Dacitic tuff was found in the color of light grey to medium grey, white, and pale yellow. It is composed of very fine-grained feldspar, volcanic glass material, sulfide mineral, and quartz. It is commonly associated with volcanic breccia layers at 524 – 599 m, 659 – 686 m, and 701 – 725 m (Figure 5.8 and Appendix B).

5.1.4 Volcanic breccia

Volcanic breccia has a broader range of color than the other rock types. It appeared in light to dark grey, reddish grey, light brown, dark to light green, dark to pale yellow, and white. Chemical composition in the volcanic breccia varies from basalt andesitic, andesitic, trachyandesitic, to dacitic (Figure 5.14).

Volcanic breccia has fragmental texture. It is composed of clay-sized volcanic material, medium to coarse-grained quartz (0.5 – 1 mm), fine-grained feldspars, and mixture fragments of lithic tuff and lava. Some lithic fragments had trachytic texture in the rock matrix and embayment quartz (Figure 5.5).

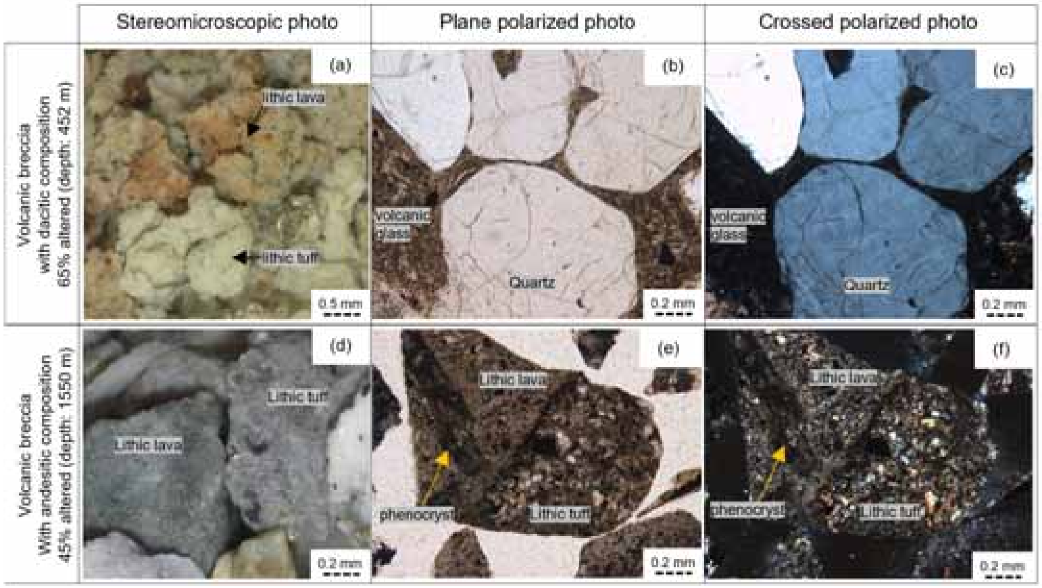

Figure 5.5 Volcanic breccia in borehole HLS-EX.

5.2 Stratigraphic units and alteration intensity

5.2.1 Stratigraphic units

The strThe stratigraphic unit or formation within well HLS-EX was constructed by correlating the rock types from the borehole to the suggested formation from PT. Pertamina Geothermal Energy (2021). The stratigraphic units of HLS-EX from the surface to the deeper parts are Suban Agung Lava and pyroclastic (SALP), Upper Suban Agung Volcanic (USAV), Lower Suban Agung Volcanic (LSAV), Hululais Volcanic (HV), and Hululais Granodiorite Intrusion (HGI). A simplified log was made to point out the characteristic of each stratigraphic unit (Figure 5.6).

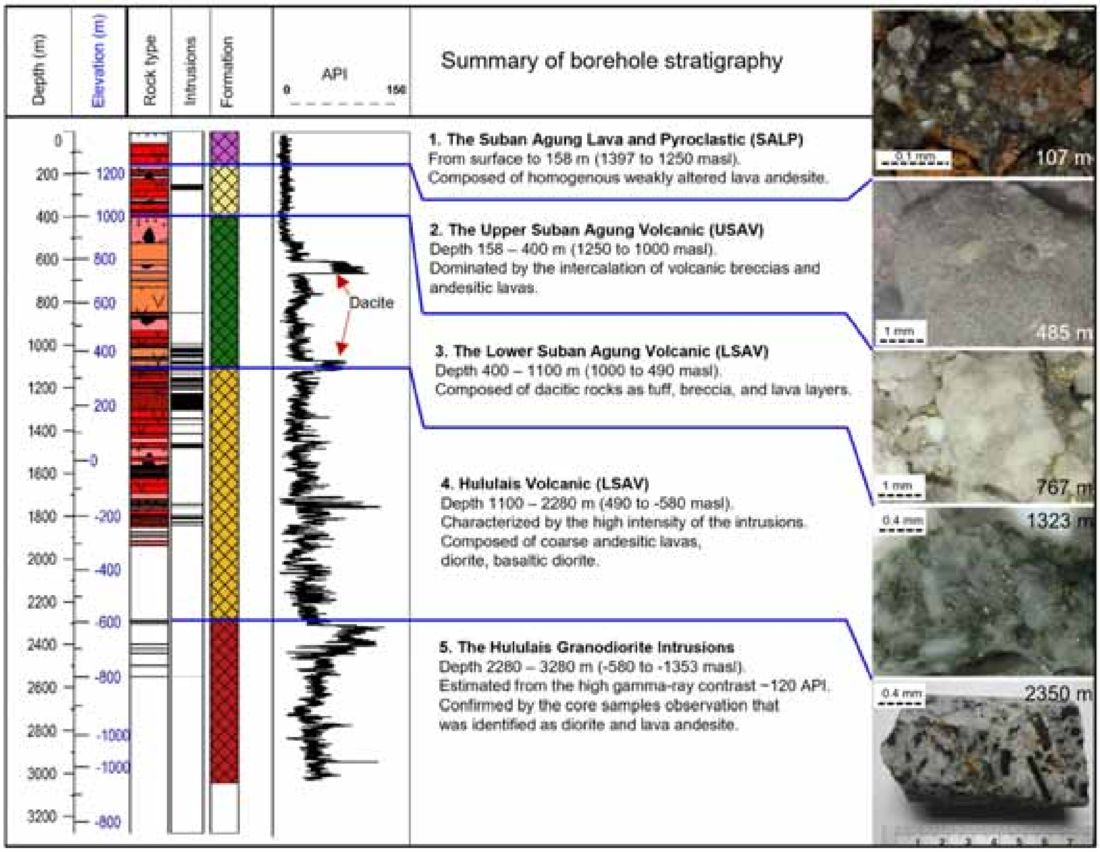

1. The Suban Agung Lava and Pyroclastic (SALP)
From surface to 158 m (1397 to 1250 masl).
Composed of homogenous weakly altered lava andesite.

2. The Upper Suban Agung Volcanic (USAV)
Depth 158 – 400 m (1250 to 1000 masl).
Dominated by the intercalation of volcanic breccias and andesitic lavas.

3. The Lower Suban Agung Volcanic (LSAV)
Depth 400 – 1100 m (1000 to 490 masl).
Composed of dacitic rocks as tuff, breccia, and lava layers.

4. Hululais Volcanic (LSAV)
Depth 1100 – 2280 m (490 to -580 masl).
Characterized by the high intensity of the intrusions.
Composed of coarse andesitic lavas,
diorite, basaltic diorite.

5. The Hululais Granodiorite Intrusions
Depth 2280 – 3280 m (-580 to -1353 masl).
Estimated from the high gamma-ray contrast ~120 API.
Confirmed by the core samples observation that
was identified as diorite and lava andesite.

Figure 5.6 Simplified borehole log shows the stratigraphic units in borehole HLS-EX.

Suban Agung Lava and Pyroclastic (SALP)

The geological map (Figure 2.4) depicts that well HLS-EX lies on the Suban Agung Lava and Pyroclastic (SALP) formation from the Mt. Suban Agung volcanic unit. In addition, the well is located on the flank of Mt. Suban Agung, on the northern part of the crater. The SALP was exposed as lava and pyroclastic with an andesitic composition.

The borehole log (Figure 5.6) indicates the SALP encountered in the borehole as homogeneous layers of lava andesite from the surface to 158 m depth (1397 – 1250 masl). It is associated with the unaltered to weakly altered rocks (Figure 5.7) and shallow TLC zones at depths of 26 – 55 and 67 – 70 m.

Upper Suban Agung Volcanic (USAV)

The dominance of andesitic lavas and volcanic breccia is correlated with the Upper Suban Agung Volcanic (USAV). This formation is composed of pyroclastic tuff, volcanic breccia, and lahars. In this study, the lahar is difficult to identify from drill cuttings, even though the volcanic breccia could be the product of lahar due to the mixture of rocks and clay.

Upper Suban Agung Volcanic (USAV) was determined from depths 158 to 400 m (1250 – 1000 masl). It is generally weakly to moderately altered (Figure 5.7). An intrusion layer was found at 248 – 275 m with an andesitic composition.

Lower Suban Agung Volcanic (LSAV)

Lower Suban Agung Volcanic (LSAV) comprises dacitic rocks that continuously appear at 524 – 934 m. It includes lava dacite, dacitic tuff, and volcanic breccia. The dacitic composition was also portrayed in the rising trend of the gamma-ray value with a prominent spike at 80 – 90 API at depths of 600 – 650 m, interval 1013 – 1055 m, and 1073 – 1097 m (Figure 5.8).

The LSAV was described as the intercalation of lava andesite, volcanic breccia, and ignimbrites at elevations 700 to 0 masl in the model (PT Pertamina Geothermal Energy, 2021). LSAV's ignimbrite and lava dacite display similar glass dominant textures. Thus, the dacitic rock layers in the borehole were correlated to the LSAV formation. The LSAV zone in borehole HLS-EX extends from 400 – 1100 m, and this formation shows the highest degree of alteration (Figure 5.7). Granodiorite intrusions started to appear in the bottom part of LSAV from around 1000 to 1100 m, and it is still associated with dacitic lava.

Hululais Volcanic (HV)

High frequency of the diorite intrusions and compositional change in lavas from dacitic to andesitic characterize the Hululais Volcanic (HV) from 1100 m depth. About nineteen diorite intrusions were discovered in this stratigraphic unit with various thicknesses. The majority of the intrusions were found in 3 m thickness. The thickest intrusions were a basaltic diorite layer with 81 m and diorite layer with 24 m thickness, respectively. The associated rock types are lava andesite, diorite, basaltic diorite, and volcanic breccia.

The last cutting data is recovered at 1934 m depth and was identified as lava andesite, even though an intermix of cuttings has potentially occurred from 1846 m depth due to the usage of aerated drilling. The HV formation was estimated to extend from 1100 to 2280 m depth (1050 to -580 masl) along the borehole, with a 348 m interval of the TLC zone. The bottom boundary of the HV formation was estimated from the gamma-ray contrast at 2280 m, which also indicates the top of the Hululais Granodiorite Intrusions (HGI) formation.

Hululais Granodiorite Intrusion (HGI)

Gamma-ray and sidewall cores provided sufficient information in the TLC zone (1937 – 3280 m). The top of Hululais Granodiorite Intrusions (HGI) was estimated from the depth where gamma-ray increases from ~40 to ~120 API instantly and stays relatively high until 2980 m.

The sidewall cores confirm the presence of diorite intrusions at 2286, 2290, 2300, and 2550 m. The diorite intrusions are associated with andesite lava identified from cores at 2400, 2420, 2440, and 2500 m. Thus, the HGI formation was interpreted to extend from depths of 2280 m to the TD well at 3280 m, equivalent to -580 to -1353 masl.

5.2.2 Relationship between the stratigraphic units and alteration intensity

The relationship between the stratigraphic units and alteration intensity was plotted along the borehole (Figure 5.7). Three main sections can be observed with changing intensities of hydrothermal alteration.

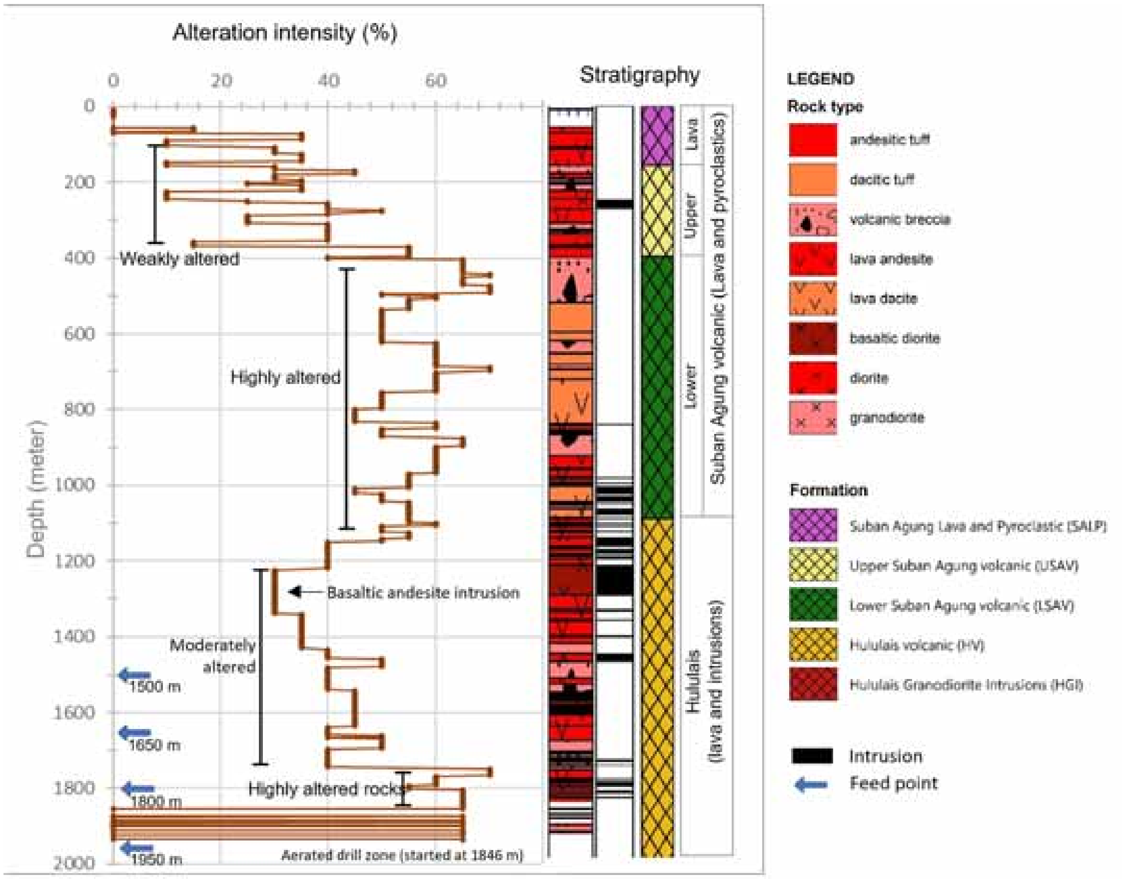

Figure 5.7 Correlation log shows the variation of alteration intensity and stratigraphic unit along with the borehole depth.

The weakly altered zone extends from 100 to 400 m and correlates with the upper part of Suban Agung volcanic (SALP and USAV) units. Highly altered rocks were found at 400 – 1150 m and 1750 – 1850 m (Figure 5.7). Between 400 and 1150 m, the highly altered rocks belong to the Lower Suban Agung Volcanic (LSAV), whereas from 1750 and 1850 m, the highly altered rocks belong to the Hululais Volcanic (HV) formation. Moderately altered rocks generally characterize the HV formation at 1200 – 1750 m.

Two feed points at depths 1500 and 1650 m observed in the HV formation are associated with moderately altered rocks. The other two feed points from depths 1800 and 1950 m correlate with higher alteration intensity. Another feed point at 2050 m was measured at the TLC zone with no cutting samples.

5.3 Secondary mineral assemblages

Interaction between the rock and hydrothermal fluid in well HLS-EX has transformed the primary minerals into secondary mineral assemblages. Clay minerals, calcite, Fe-Ti oxides, pyrite, epidote, secondary quartz, anhydrite, albite, wairakite, actinolite, and secondary biotite are the secondary minerals discovered in borehole HLS-EX (Figure 5.8)

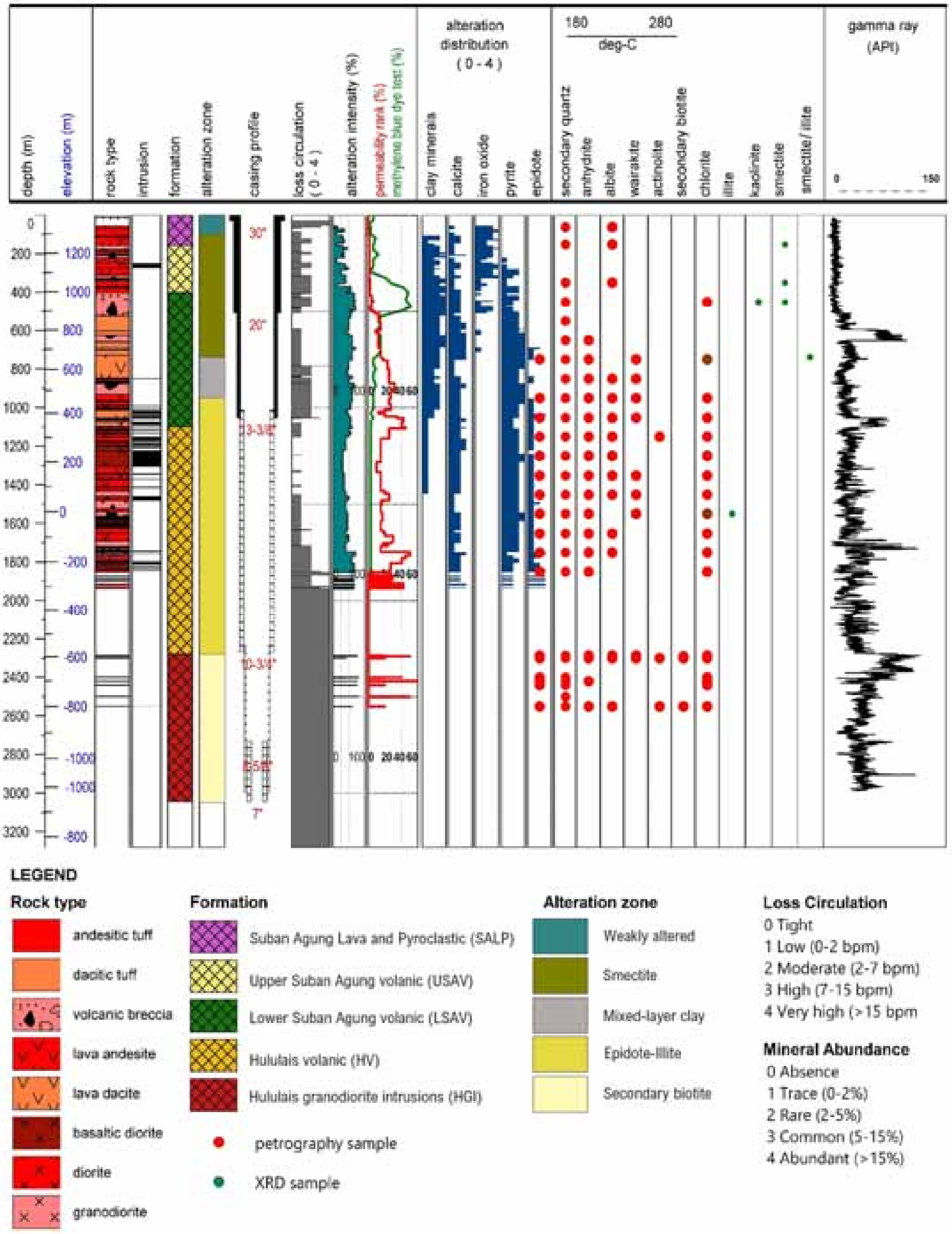

Figure 5.8 Borehole log of HLS-EX interval 0 – 3280 meters.

Clay minerals are clay-sized (ash) materials in sizes less than 2 mm (Fisher, 1961). By stereomicroscopic observation, it appears abundantly at 107 to 1050 m depth in grey, reddish-brown, white, and yellowish-green colors. In a polarization microscope, clay minerals appear in brown, light brown, reddish, and greenish colors. The clay minerals are smectite, kaolinite, chlorite, illite, and mixed-layer clay (MLC) which were detected through XRD analysis (see Chapter 5.5).

Calcite is transparent to translucent in the stereomicroscopic examination. Under a polarization microscope, calcite shows perfect cleavages and association with pyrite, anhydrite, secondary quartz, and chlorite. Calcite is present in all depths along the borehole with a fluctuated abundance of around 2 to 15% (Figure 5.9 a and i, Figure 5.10 b, c, and d).

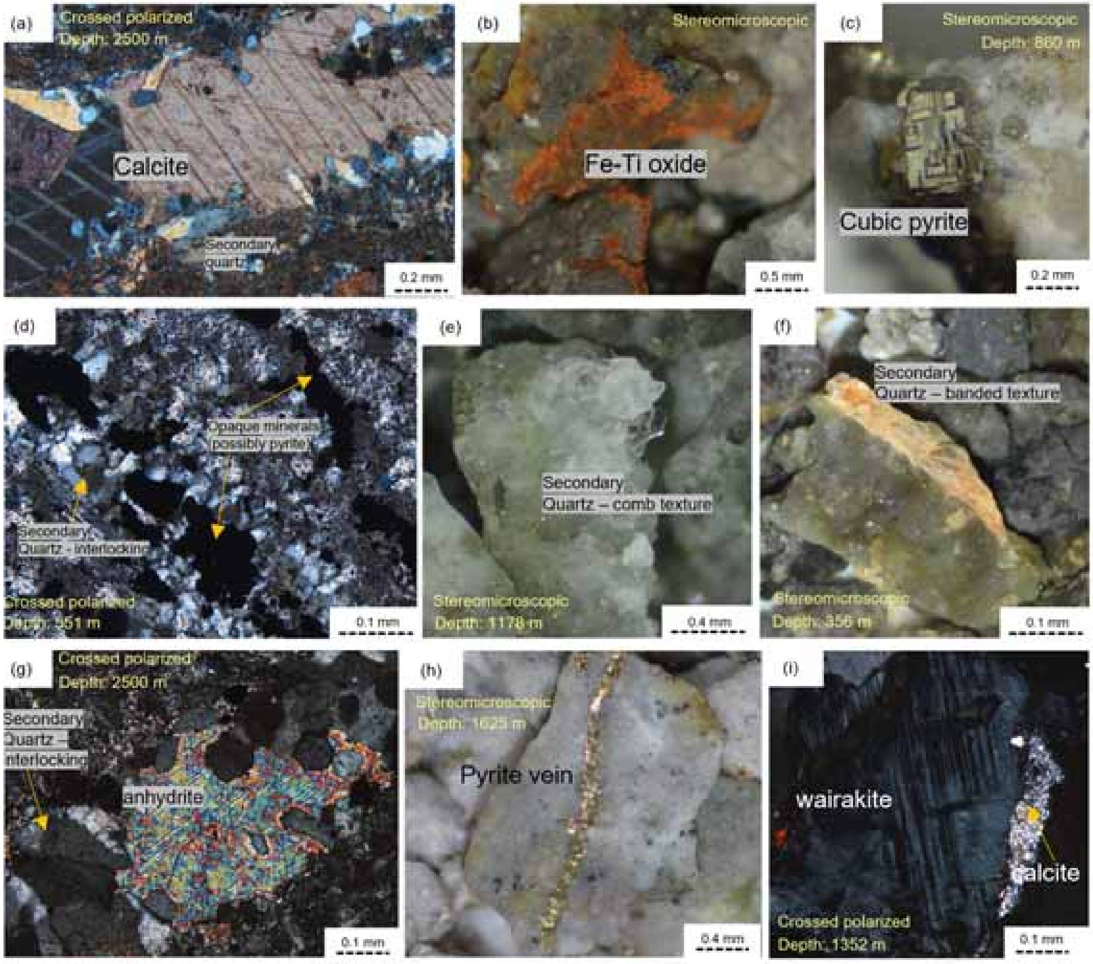

Figure 5.9 Secondary mineral assemblages show a paragenetic sequence of secondary quartz – calcite veins (a), iron oxide mineral (b), Cubic pyrite (c), a sequence of secondary quartz and opaque minerals in veins (d), Crystal growth of the euhedral secondary quartz (e), a vein of secondary quartz with banded texture (f), a vein of secondary quartz and anhydrite (g), a vein of pyrite (h), and a vein of wairakite and calcite (i).

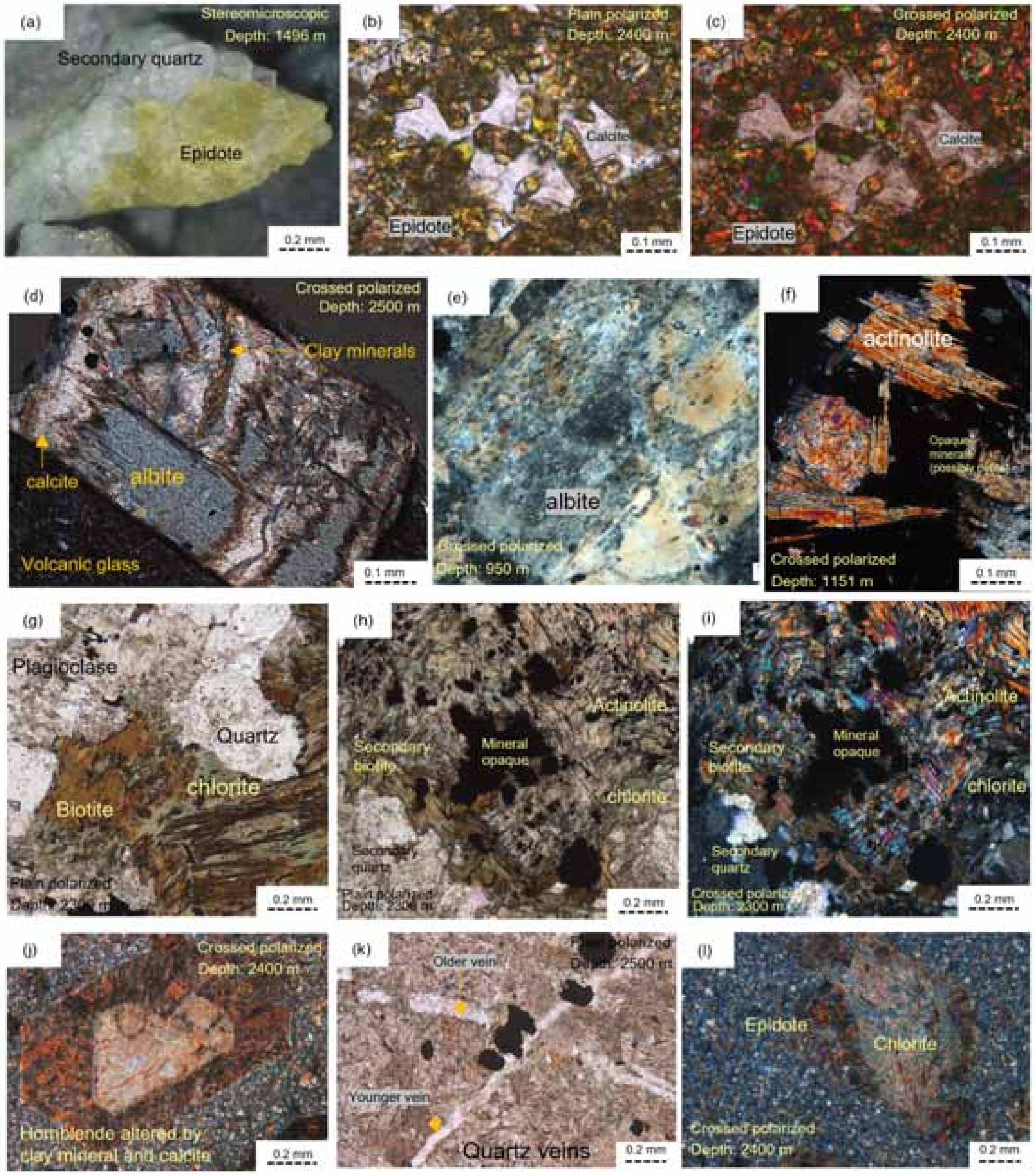

Figure 5.10 Secondary mineral assemblages show a paragenetic sequence of secondary quartz – epidote veins (a), a paragenetic sequence of calcite – epidote vein (b-c), albitization in plagioclase with micro veins filled by calcite and clay minerals (d), albitization in plagioclase (e), actinolite and opaque mineral vein (f), chloritization of biotite in granodiorite (g), secondary biotite forming associated with actinolite, chlorite, and opaque minerals (h and i), chloritization of hornblende (j), crosscutting between two generations of secondary quartz veins followed by opaque mineral deposition (k), chloritization and epidotization in mafic phenocrysts grain (i).

Oxide minerals are present as red to brown, brittle clay-sized crystals. They appear as aggregates and impurities in the rock mass, associated with clay and sulfide minerals. Mineral oxides were abundantly found (up to 15% of the rock composition) at depths 56 – 326 m, 443 – 452 m, and 473 – 506 m. Generally, it decreased to less than 5% from interval 326 – 440 m and finally disappeared at 611 m downwards (Figure 5.9 b).

Pyrite or sulfide minerals are commonly found in golden yellow, reddish to metallic dark brown colors in stereomicroscopic examination. Moreover, it is an opaque mineral in a polarization microscope. It is present in euhedral cubic grains in sizes smaller than 0.1 mm up to 2 mm, associated with calcite, clay minerals, and secondary quartz. Pyrite appeared and gradually increased in an interval of 140 – 419 m. It is significantly abundant in the veins starting at depth 614 m downwards (Figure 5.9 c, d, h, Figure 5.10 f, h, i, and k).

Under stereomicroscopic examination, secondary quartz occurred as a white, translucent, colorless mineral with a reddish, yellowish, and greenish-grey spectrum. The crystal appeared in prismatic euhedral to subhedral grains from size < 1 mm up to 2 mm. It is associated with calcite, pyrite, chlorite, anhydrite, wairakite, and epidote. In contrast with primary quartz, the secondary quartz does not show an embayment shape at its surface under a polarization microscope (Figure 5.5). Instead, secondary quartz usually appears in the interlocking, comb, or banded textures, especially in the rock vein system (Figure 5.9 a, d, e, f, g, Figure 5.10 h, i, and k).

Anhydrite is a white to translucent mineral with a vitreous luster. Under a polarization microscope, it shows very high birefringence (third order of blue, green violet) and perfect cleavage. Its presence is associated with secondary quartz, wairakite, calcite, and epidote in the hydrothermal veins. Anhydrite was found from 650 to 1850 m depth and in core samples from 2286, 2290, 2300, 2420, 2500, and 2550 m (Figure 5.9 g).

Albite is cloudy white, grey to translucent prismatic mineral in the stereomicroscopic examination, although best identified under the polarization microscope. It commonly gives plagioclase a “broken white” appearance and has a low birefringence in the first order. Albite is associated with epidote, chlorite, secondary quartz, and anhydrite. (Figure 5.10 d and e).

Under polarization microscope, wairakite appeared in white, light grey, and dark grey. It has a low birefringence first-order grey under the cross-polarized light. Furthermore, wairakite shows an intense tartan pattern twinning. Wairakite is associated with secondary quartz, albite, and anhydrite. It was found from depths 749 to 1550 m and in core samples of 2286 and 2300 m as veins (Figure 5.9 i).

Actinolite appears as a transparent, light green, yellowish needle-like crystal, with a weak pleochroism from pale green to yellow, in the plane-polarized light in the polarization microscope. In a crossed polarized light, actinolite shows colors from light brown, dark yellow, reddish, blue, and violet of the second order, associated with perfect cleavages. The grain size varies from fine lath-like grains up to 0.5 mm long. Actinolite is associated with chlorite, opaque minerals, secondary biotite, and quartz (Figure 5.10 f, h, and i).

In a polarization microscope, secondary biotite has a dark green to brown color, pleochroism from green to brown, perfect cleavage, and a supple lamellar structure (platy). Secondary biotite is distinguished from primary biotite by its finer-sized aggregate, presence filling the space between mineral grains as the product of hydrothermal precipitation. Meanwhile, primary biotite usually appears in a coarser euhedral crystal habit with stronger foliation and weakly bent. Secondary biotite was found in core samples from depths 2290, 2300, and 2550 m, associated with chlorite, actinolite, opaque minerals, and secondary quartz (Figure 5.10 h and i).

Epidote occurs as prismatic minerals in the color of yellow, light green to colorless with grain size reaching up to 1 mm. In crossed polarized light, epidote shows a high birefringence (third order of yellow, green, red, to violet). Moreover, it has a weak pleochroism from transparent, yellow, to light green in plane-polarized light. Epidote is commonly found with calcite, secondary quartz, anhydrite, opaque minerals, and chlorite. It appears from the depth of 749 m downwards (Figure 5.10 a, b, c, and i).

5.4 Hydrothermal alteration style

The hydrothermal alteration process identified in borehole HLS-EX occurred in two styles, (1) the replacement and (2) the depositional. The replacement style is generally identified in primary mineral grains. Plagioclases, pyroxenes, hornblende, and biotite acted as the primary minerals where the replacement took place. Plagioclase was replaced by clay minerals, albite, calcite, secondary quartz, and epidote. The clay minerals, chlorite, and epidote were formed at the expense of pyroxene. Hornblende was replaced by chlorite, actinolite, and secondary biotite. Primary biotite was altered to chlorite and secondary biotite. Clay minerals altered the volcanic glass. Fe-Ti oxides form some opaque minerals like pyrite and magnetite (Table 5.2).

Table 5.2 Hydrothermal alteration of major primary minerals in the study.

No	**Primary mineral**	Altered to:	**Secondary minerals**
1.	Plagioclase		Clay minerals, albite, calcite, secondary quartz, and epidote.
2.	Pyroxene		Clay minerals, chlorite, and epidote.
3.	Hornblende		Chlorite, actinolite, and secondary biotite.
4.	Biotite		Chlorite, secondary biotite.
5.	Volcanic glass		Clay minerals.
6.	Fe-Ti Oxides		Pyrite, ilmenite, titanite.

The depositional style was well recorded in rock veins and cavities, which could be filled by a single or more than one mineral type. When the deposition sequences are observable, a paragenetic sequence can be determined. The paragenetic sequence indicates the change during the deposition of a secondary mineral based on the index mineral geothermometry in Figure 6.3.

The paragenetic sequence is divided into the prograde, retrograde, and outstretched types (Appendix D). A prograde paragenetic sequence suggests the increase in hydrothermal fluid temperature by the deposition of a lower-temperature mineral, followed by a higher temperature mineral, e.g., the secondary quartz – epidote vein (Figure 5.10 a). The secondary quartz was formed at a minimum temperature of 180 °C and epidote at 230 °C (Reyes, 1990).

This trend likely indicates an initiation temperature built up. The retrograde paragenetic sequence works oppositely, it indicates the decline in hydrothermal fluid temperature during the mineral deposition in rock veins. The outstretched paragenetic sequence represents the deposition of minerals with wide temperature spans, for example, calcite at 80 – 325 °C and pyrite at 50 – 400 °C (Reyes, 1990).

5.5 Clay minerals

Clay minerals were identified through X-ray powder diffractometry (XRD) analysis. The result shows the presence of smectite, illite, mixed-layer clay (MLC) of smectite/illite, kaolinite, and unstable chlorite. Some non-clay minerals such as plagioclase and gypsum are also identified (Table 5.3).

Table 5.3 The results of X-ray diffractometry analysis.

No.	Depth (meter)	*d spacing* [001] (Å)			*d spacing* [002] (Å)	Mineral
		untreated	glycolated	heated		
1	152	12.76	14.35	10.05		Smectite
		6.49	6.49	6.49		Plagioclase*
2	350	12.27	14.82	9.84		Smectite
		6.49	6.49	6.49		Plagioclase*
3	452	11.46	13.02	9.92		Smectite
		7.16	7.162			Kaolinite
		6.49	6.49	6.49		Plagioclase*
4	749	14.11	14.11	14.11	7.12	Unstable chlorite
		10.02	10.02	10.02		Illite/smectite (MLC)
		7.62	7.62			Gypsum*
5	1550	14.11	14.11	14.11	7.12	Unstable chlorite
		10.01	10.01	10.01		Illite
		7.60	7.60			Gypsum*

** Indicates mineral impurities in the clay separation.*
**MLC: Mixed-layer clay*

The smectite group is distinguished by comparing the peak patterns in untreated, glycolated, and heated conditions. Pure smectite reflects peaks at ~17 Å (untreated) that swell to 15 Å when its glycolated, then decays to 10 Å after heating up (Moore & Reynolds, 1997). The smectite group commonly has a broad diffraction peak from around 12-13 Å to 15-17 Å. (Chen, 1977). Smectite (montmorillonite) in the studied samples from depths 152, 350, and 452 m has *d-spacing* peaks at ~12 Å in untreated conditions, expands to ~14 Å when glycolated, and finally collapses at ~10 Å after heating (Figure 5.11)

Illite always shows a stable, strong narrow peak at ~10 Å. The peaks shifting and broadening to a higher number indicate the presence of illite/smectite intercalating (Moore & Reynolds, 1997). The firm narrow illite peaks at 10.01 Å were observable at a sample from a depth of 1550 m. Meanwhile, broader and shifted illite peaks were identified from depth 749, indicating a presence of mixed-layer clay of smectite/illite (Figure 5.12).

Kaolinite and chlorite have a peak reflection of around 7 Å in air-dried. Kaolinite is distinguished from chlorite by observing its peak in glycolated and heated conditions. Kaolinite does not show any difference in glycol saturated conditions, and the peak collapsed due to heating (Moore & Reynolds, 1997). In the studied rocks, kaolinite was identified based on the diffraction peak of 7.162 Å in untreated and glycolated samples from 452 m (Figure 5.12).

The unstable chlorite does not show significant *d-spacing* shifting in various treatments. The peak is observable at 14.11 and 7.12 Å. Unstable chlorite is found in the sample from depths 749 and 1550 m (Figure 5.12). Some peaks belong to non-clay minerals, which are impurities. The peak at 6.491 Å in samples 152, 350, and 452 m is interpreted as plagioclase. Gypsum is identified at the peak of 7.60 Å in samples 749 and 1550 m (Figure 5.11 and Figure 5.12).

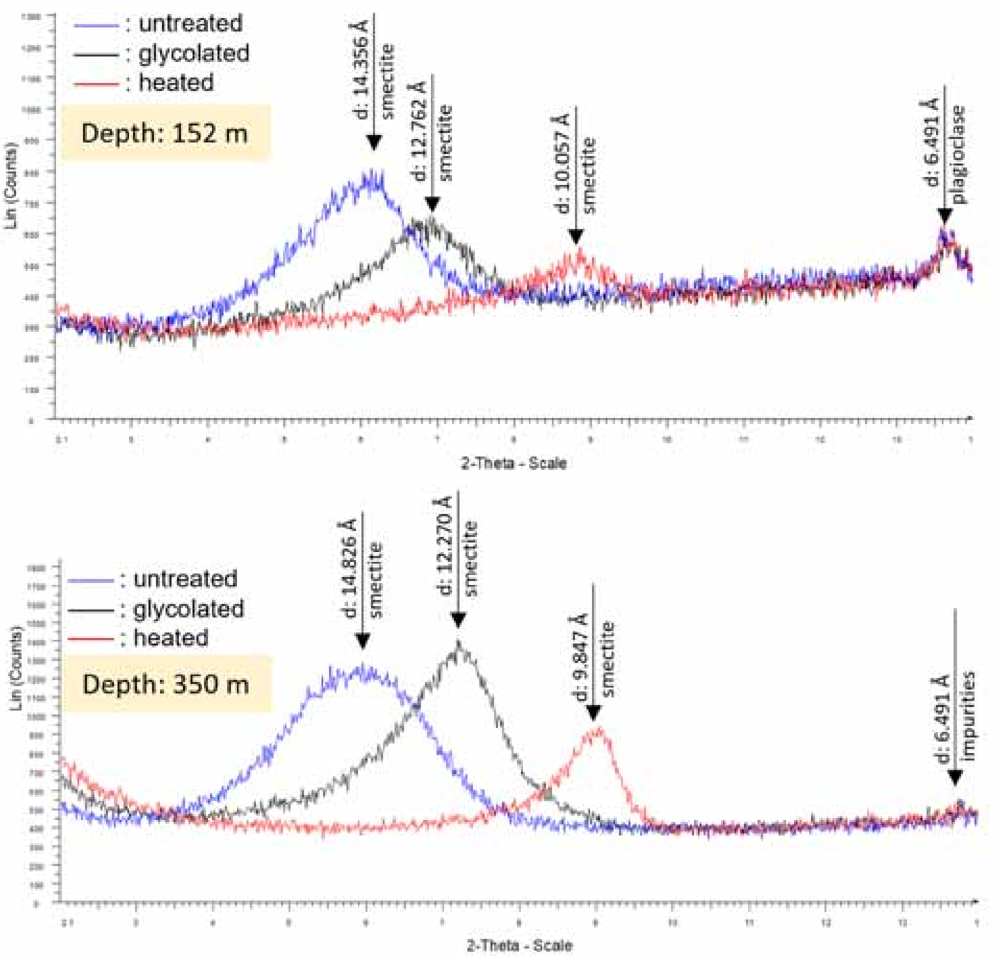

Figure 5.11 The XRD spectra of cutting samples at depths of 152 and 350 m show the appearance peaks of smectite. The impurities in the sample were identified as plagioclase and gypsum.

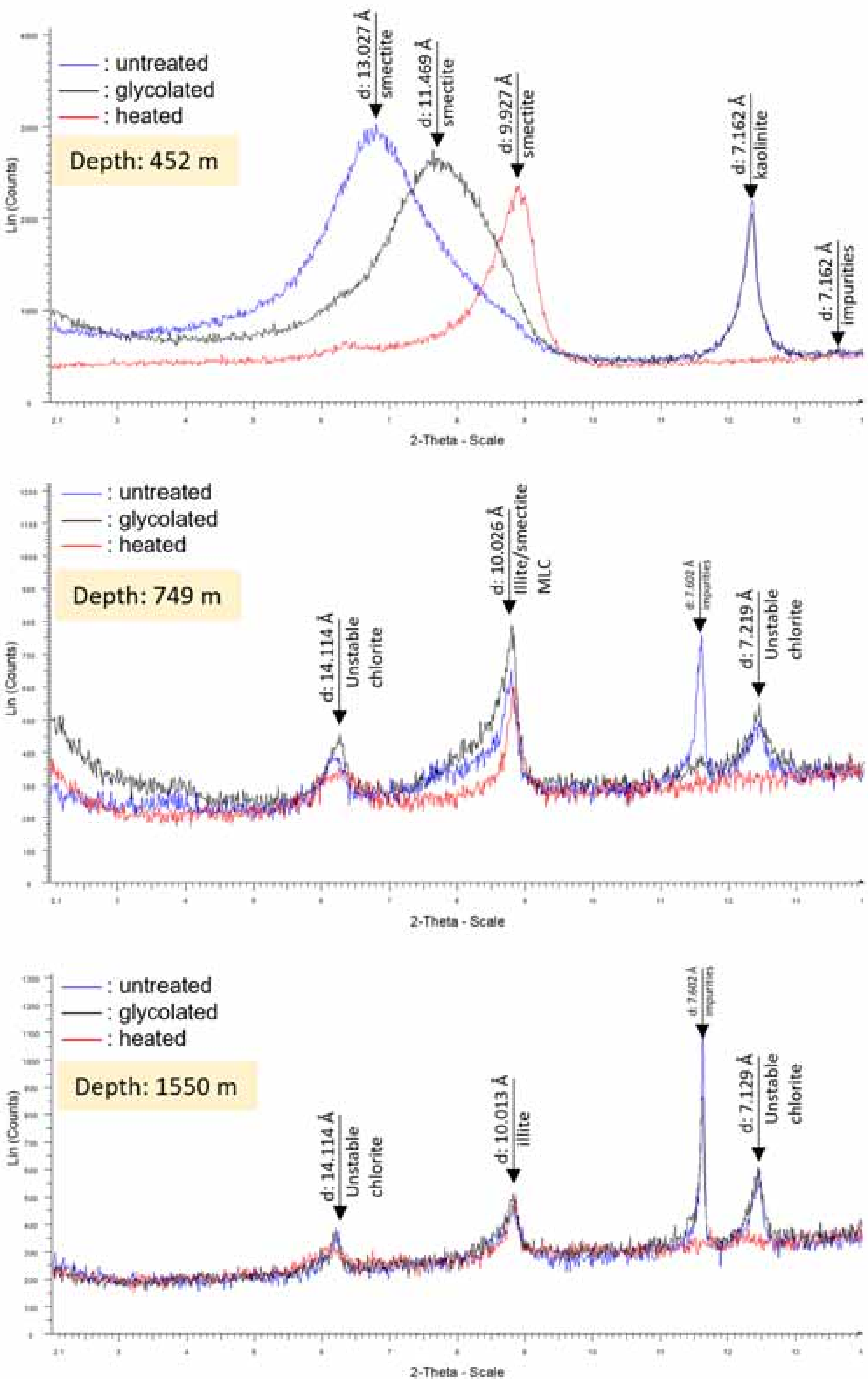

Figure 5.12 The XRD spectra of cutting samples at depths of 452, 749, and 1550 m show peaks of mineral smectite, mixed-layer clay of illite/smectite, kaolinite, illite, and unstable chlorite.

5.6 Loss on ignition

The loss on ignition (LOI) test was performed on sixteen rock samples. The majority of the LOI samples were selected due to their compositional anomaly, and others represent the variety of rock types and the alteration intensity (Table 5.4).

Table 5.4 Result of loss on ignition (LOI) test.

Loss on ignition (%)		Depth (meter)	Texture	Alteration intensity (%)		Remarks
1.38	Increases of LOI %	152	coherent lava	10		Weakly altered lava
1.40		62	coherent lava	15		Weakly altered lava
2.89		77	coherent lava	35		Excess Co
2.91		1751	volcanic breccia	70		Excess Ca
2.97		1250	intrusions	30		Weakly altered intrusion
3.10		1016	coherent lava	45		Low alkali and high SiO
3.82		1829	intrusions	65		Excess Cr and Zn
3.83		1691	coherent lava	50		The highest alkali
3.95		1667	coherent lava	40		High alkali
4.64		392	pyroclastic tuff	55		Excess Cr
6.80		749	coherent lava	60	Dacitic	Low alkali and high SiO_2
7.19		587	pyroclastic tuff	50		Low alkali and high SiO_2
7.29		650	volcanic breccia	60		Low alkali and high SiO_2
7.35		779	coherent lava	50		Low alkali and high SiO_2
7.44		551	pyroclastic tuff	50		Low alkali and high SiO_2
10.78		884	volcanic breccia	65		The lowest SiO_2

Generally, the alteration intensity and LOI have a positive correlation. The LOI is higher in the more altered samples. Moreover, the low alkali and high SiO_2 content samples (from dacitic rocks) show a higher LOI percentage. Dacitic rocks tend to have higher LOI even though they are not the most intensely altered rocks among the sample (Figure 5.13).

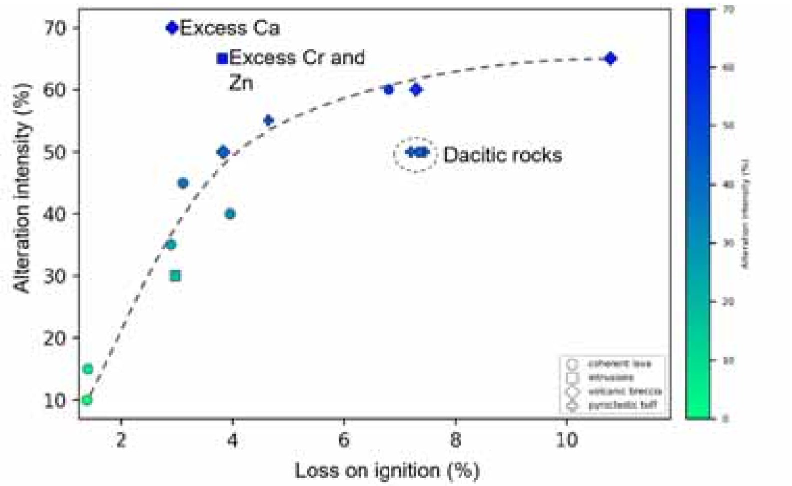

Figure 5.13 Correlation plot between alteration intensity versus the loss of ignition.

5.7 Compositional variation

5.7.1 Total alkali-silica diagram

The total-alkali-silica (TAS) diagram classifies most samples as andesites. Out of sixty whole-rock cuttings samples, 70% are categorized as andesites, 16% dacites, 10% basaltic andesites, 2% basalt, and 2% trachyandesite (Figure 5.14). The basalt (at 884 m) and trachyandesite (at 1691 m) outliers are attained from the heavily altered volcanic breccia, in which basalt has a high LOI reaching 10.78%, and trachyandesite has 3.83%. In addition, five highly altered samples from dacite also show high LOI ranging from 6.81 to 7.44% (Table 5.4).

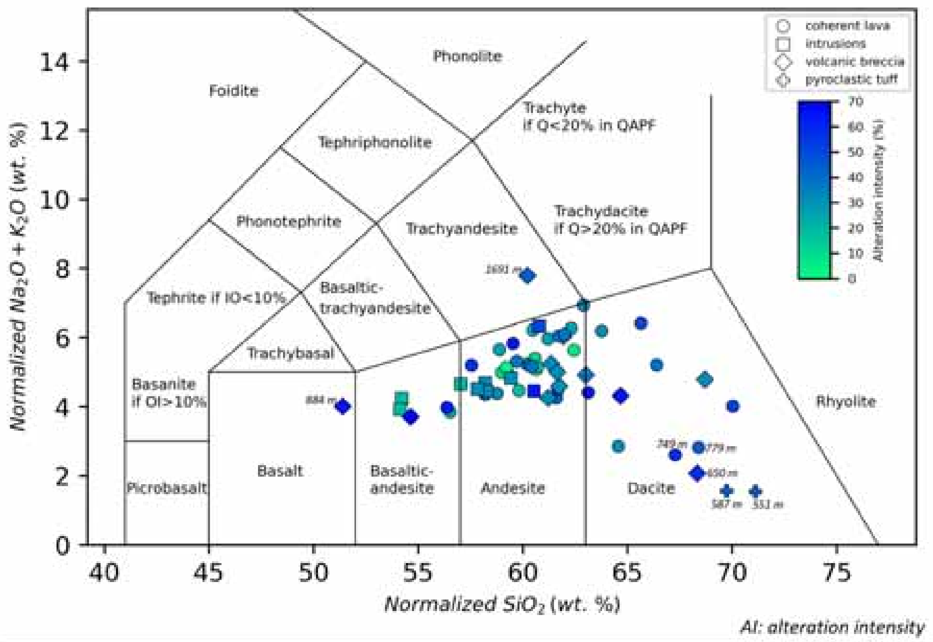

No.	Composition	Texture and sample depths
1	Andesites (70%)	Coherent lava at 62, 107, 152, 188, 206, 230, 299, 350, 365, 851, 950, 1121, 1310, 1325, 1352, 1367, 1394, 1421, 1571, 1571b, 1580, 1601, 1631, 1652, 1667, 1784, 1850, and 1916 m. Intrusions at 266, 1151, 1181, 1202, 1799, and 1829 m. A pyroclastic tuff at 392 m. Volcanic breccias at 317, 1451, 1481, 1508, 1520, 1550, and 1733 m. AI 10 – 65%.
2	Dacites (16%)	Coherent lavas at 605, 749, 779, 1016, 1052, and 1082 m. Pyroclastic tuffs at 551 and 587 m. Volcanic breccias at 452 and 650 m. AI 40 – 65%.
3	Basaltic andesites (10%)	Coherent lava at 77 & 1874. Intrusions at 1226, 1250, 1280. Volcanic breccia at 1751 m. AI 30 – 70%.
4	Basalt (2%)	Volcanic breccia at 884 m. AI 65%.
5	Trachyandesite (2%)	Volcanic breccia at 1691 m. AI 50%.

Figure 5.14 Total-alkali-silica (TAS) diagram shows that 70% of the samples are categorized as andesite, 16% dacite, 10% basaltic andesite, 2% basalt, and 2% trachyandesite.

5.7.2 Relationship of alteration intensity and elements mobility

Three major elements' behavior were compared to observe how the alteration process has affected the mobility of the elements that are commonly used to define magma differentiation. The MgO, SiO_2, and FeO were compared as concentration versus the alteration intensity (AI). The rock samples with an AI of < 30% are categorized as weakly altered rocks, 30 to < 40% are moderately altered rocks, and ≥ 40% are the intensively altered rocks. Five coherent lavas from shallow depths represent the weakly altered rocks. Twelve rock samples of coherent lava and intrusions are moderately altered. Lastly, forty-two rock samples are categorized as intensively altered rocks (Figure 5.15).

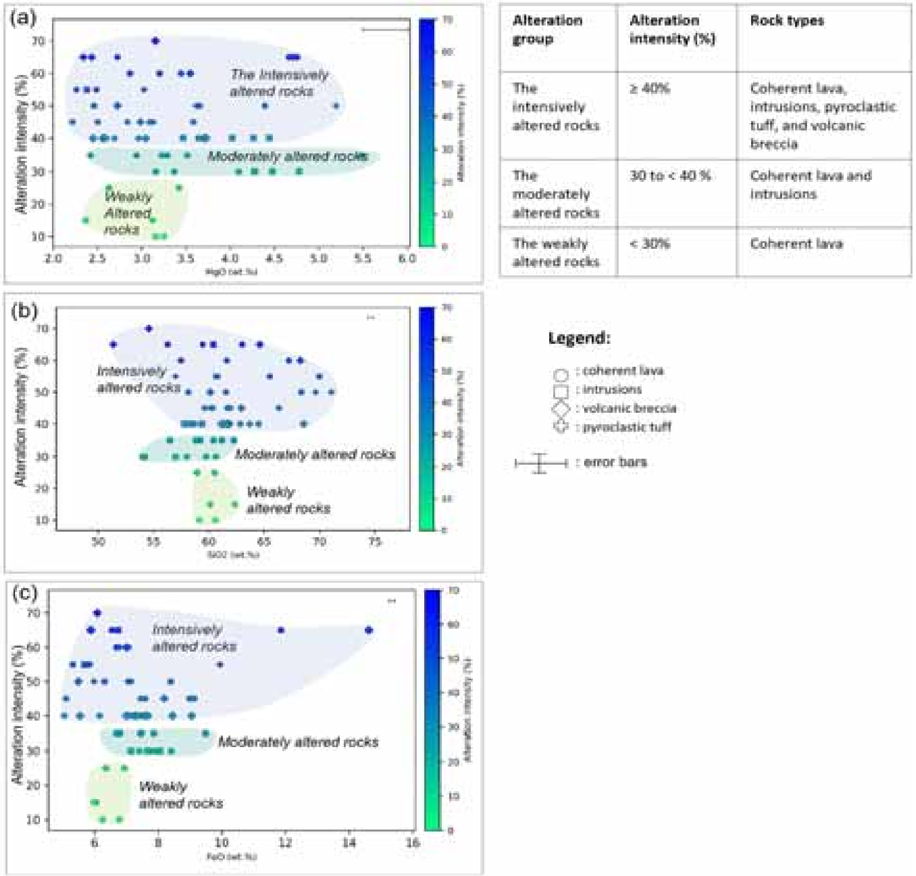

Alteration group	Alteration intensity (%)	Rock types
The intensively altered rocks	≥ 40%	Coherent lava, intrusions, pyroclastic tuff, and volcanic breccia
The moderately altered rocks	30 to < 40 %	Coherent lava and intrusions
The weakly altered rocks	< 30%	Coherent lava

Figure 5.15 Relationship of alteration intensity (AI) with MgO (a), SiO_2 (b), and FeO (c).

The MgO concentration spans from 2.22 to 5.48 wt.% for the rocks that have been moderate to intensively altered. On the other hand, MgO concentration for the weakly altered rock falls in the narrower range from 3.12 to 3.42 wt.%. Overall, the MgO composition spread is similar within moderately and strongly altered rocks (Figure 5.15 a).

The SiO_2 concentration is around 58.92 – 60.10 wt.% in the weakly altered rocks, 54.08 – 68.57 wt.% in moderately altered rocks, and 51.35 – 71.07 wt.% in the intensively altered rocks (Figure 5.15 b). The FeO concentration is 6.03 – 6.93 wt.% in the weakly altered rocks, 5.05 – 9.49 wt.% in moderately altered rocks, and 5.10 – 19.68 wt.% in the intensively altered rocks (Figure 5.15 c). The variation of SiO_2 and FeO concentration in the rock samples is getting broader by increasing alteration intensity.

As alteration intensity (AI) strongly affects the variation of SiO_2 and FeO content in the rocks, these two variables cannot be used to distinguish between magmatic evolution and hydrothermal alteration. Therefore, MgO was selected as a magmatic differentiation factor which in the following chapters will help distinguishing between these two processes.

5.7.3 Magmatic differentiation trend and hydrothermal alteration

The bivariate plots were produced to analyze the distribution and relation between the major and trace elements with the MgO content. The bivariate plots show that chemical trends are more apparent in the moderate to weakly altered samples (AI ≤ 40%) than in the intensely altered rocks. Thus, the moderate to weakly altered rock composition represents the process of magmatic differentiation. Meanwhile, the intensely altered rock compositions show how elements are mobilized during the hydrothermal alteration process, resulting in a more scattered distribution relative to the decreasing of MgO (Figure 5.16).

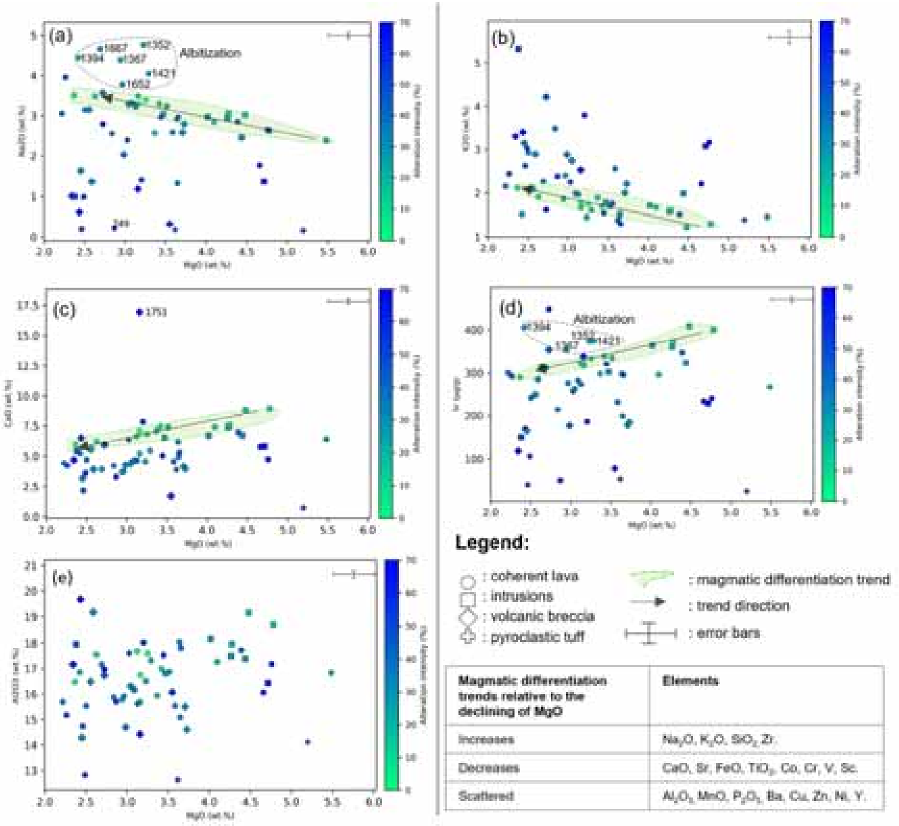

Magmatic differentiation trends relative to the declining of MgO	Elements
Increases	Na_2O, K_2O, SiO_2, Zr.
Decreases	CaO, Sr, FeO, TiO_2, Co, Cr, V, Sc.
Scattered	Al_2O_3, MnO, P_2O_5, Ba, Cu, Zn, Ni, Y.

Figure 5.16 Bivariate plots represent the trend of magmatic differentiation relative to the decline of MgO. Na_2O (a), K_2O (b), SiO_2, and Zr increase; CaO (c), Sr (d), FeO, TiO_2, Co, Cr, V, and Sc decrease with the decline of MgO. The rest of the elements do not show a correlation trend, as demonstrated by the Al_2O_3 (e).

The highly altered samples (AI >40%) show variation in distribution relative to the magmatic differentiation trend. K_2O, SiO_2, Cr, and FeO were enriched relative to the magmatic differentiation trend. Oppositely, the depletion only appears in CaO. The rest of the components, such as Na_2O, Zr, Sr, TiO_2, Co, Cr, V, and Sc, experienced both enrichment and depletion. Therefore, the highly altered rocks show extensive widespread compositions in these elements relative to the magmatic differentiation trend (Figure 5.17, Figure 5.18, and Appendix C).

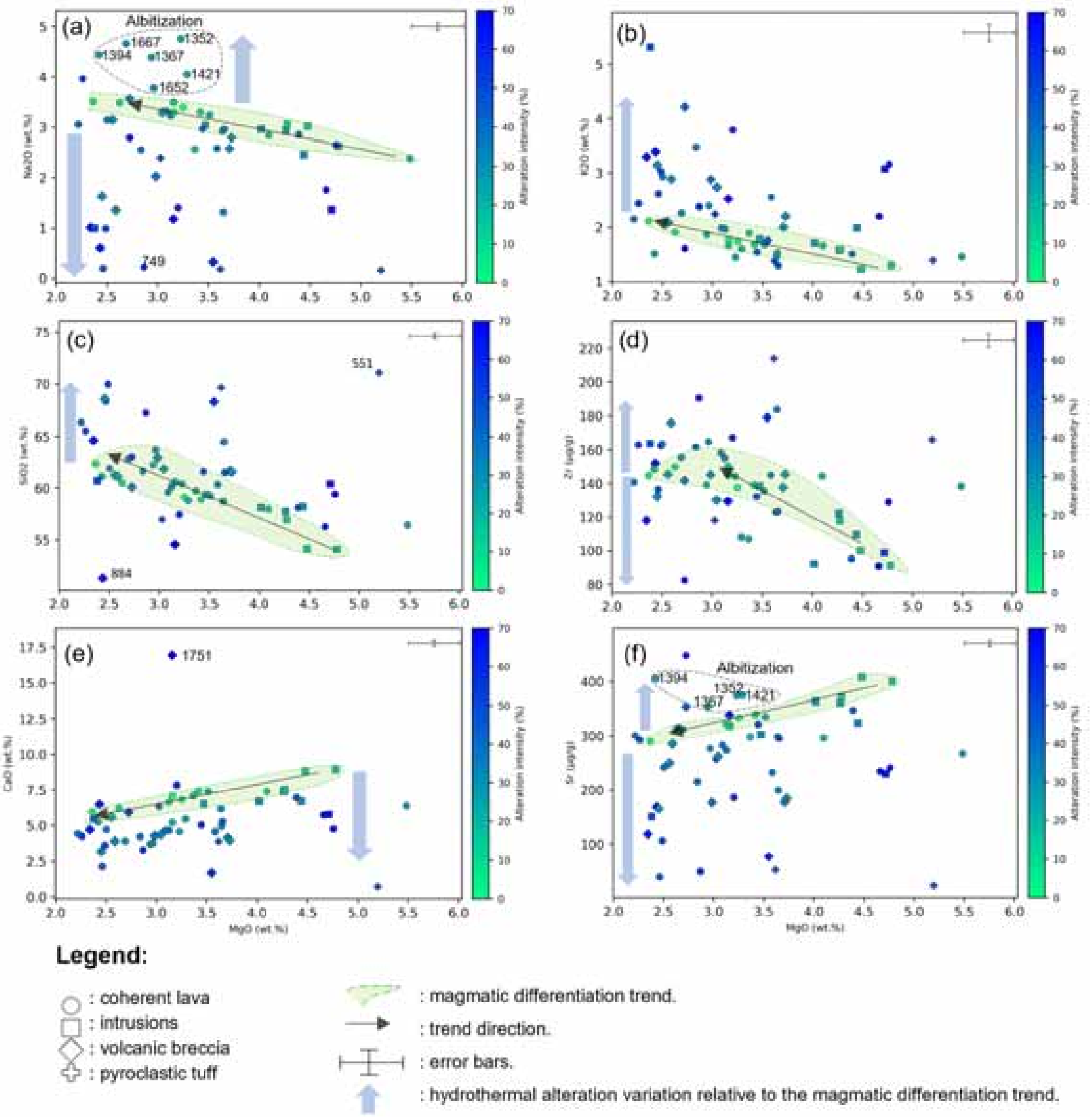

Figure 5.17 The hydrothermal alteration variation relative to the magmatic differentiation trend shows: enrichment in K_2O and SiO_2 (b and c), depletion in CaO, and both gaining and loss in Na_2O (a), Zr (d), and Sr (f).

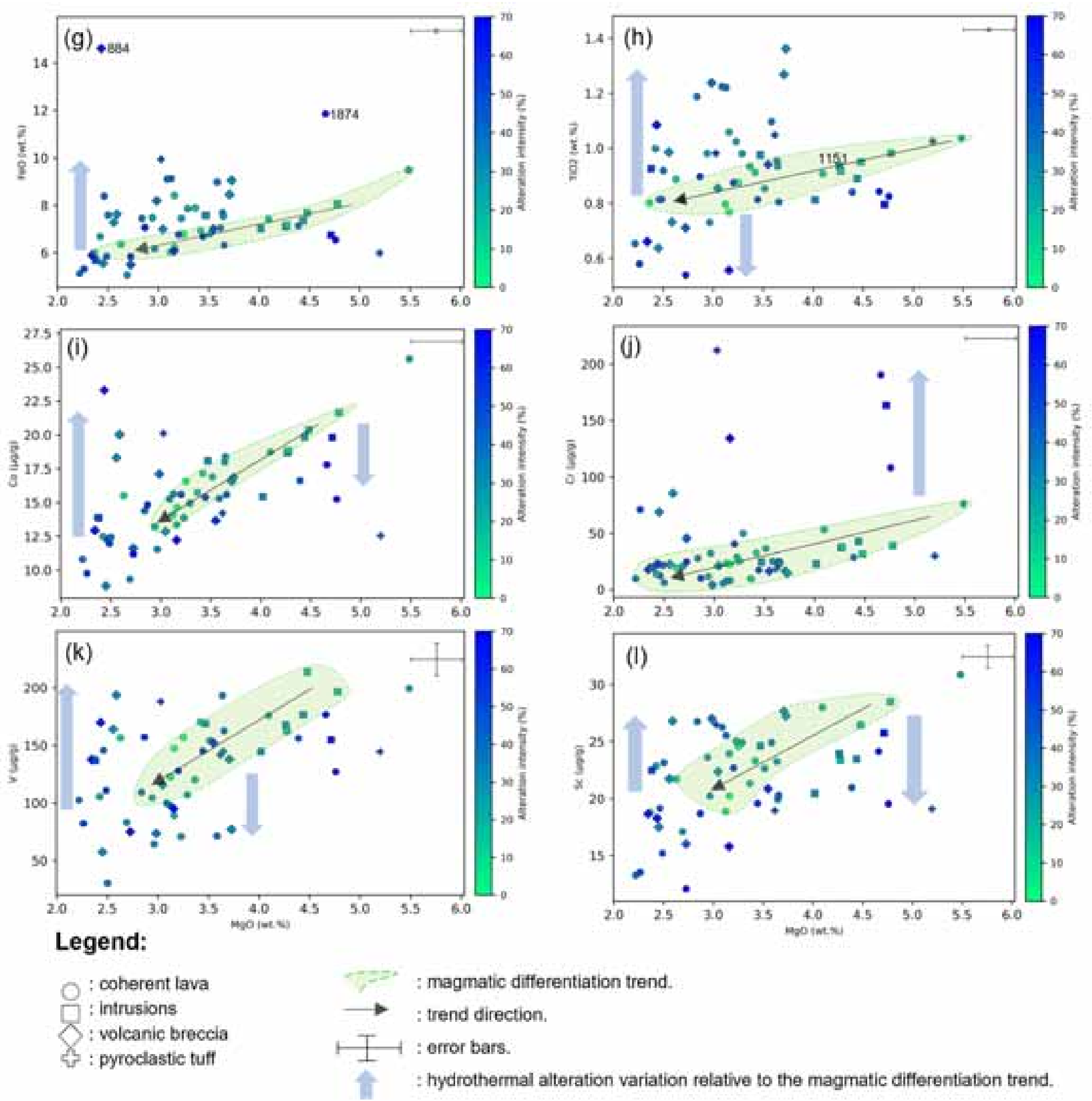

Figure 5.18 The hydrothermal alteration variation relative to the magmatic differentiation trend shows enrichment in FeO and Cr (g and j), and both enrichment and depletion in TiO_2, Co, V, and Sc (h, i, k, and l).

6 Discussion

6.1 Stratigraphy

As located in a hot wet climate, soil and vegetation dominantly cover the surface of the Hululais geothermal field. Remote sensing images were optimized to establish the surface rock formations based on the topography's pattern in liDAR, combined with the volcano stratigraphy delineation (Figure 2.4).

Beneath the surface, the rock formation was estimated from onsite stereomicroscopic examination during the drilling, as modeled in Figure 2.6. However, the model interpolates and simplifies rock formation based on drill cuttings' physical properties. Moreover, there was no available data on the rock's chemical composition from the borehole and the surface. Compared to the model, the stratigraphic units discovered in the borehole fit with diverse depths and thicknesses (Figure 6.1).

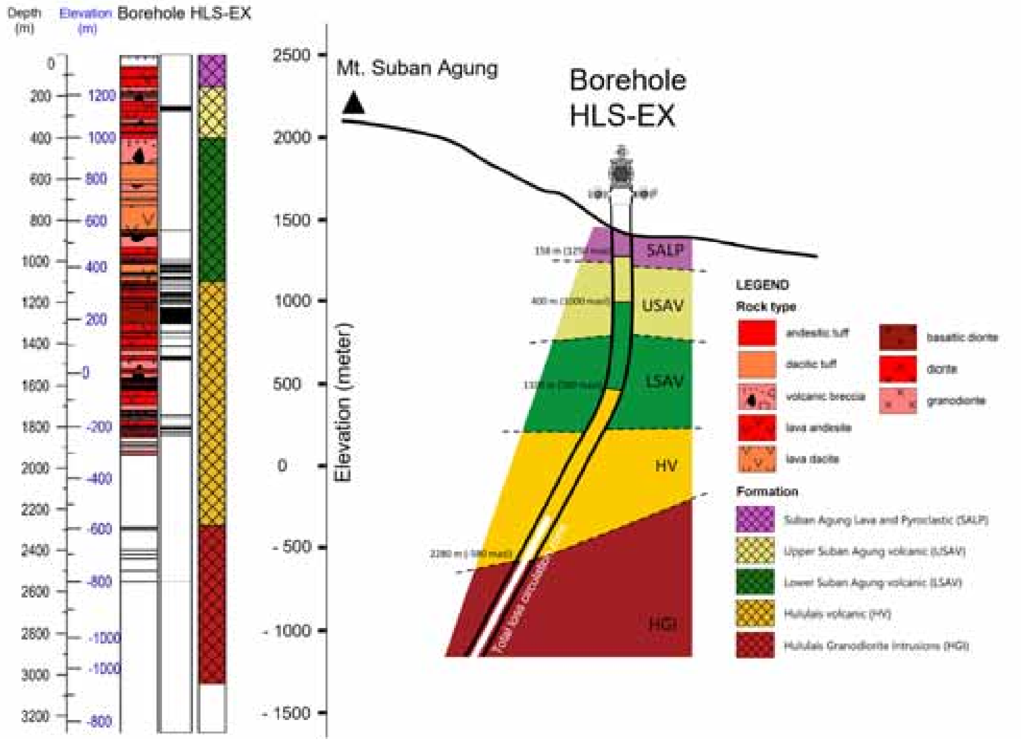

Figure 6.1 Illustration of stratigraphic units dicovered along the borehole of HLS-EX correlated with the subsurface rock model of the Hululais geothermal field.

The Suban Agung Lava and pyroclastic (SALP) is the only stratigraphic unit exposed on the surface. However, there is no thickness information from the surface outcrops. The homogenous unaltered to weakly altered andesitic lavas associated with the shallow TLC zone characterize SALP from the borehole. The TLC zone in SALP formation possibly reflects the fractures commonly found in a coherent lava body on the surface, such as columnar and sheeting joints, or the fractures produced during the ancient explosion in Mt. Suban Agung (Figure 2.5).

The Upper Suban Agung Volcanic (USAV) and Lower Suban Agung Volcanic (LSAV) were found shallower in the borehole compared to the model. No dacitic rock has ever been remarked in this field from previous models and literature. Thus, this compositional attribute is suggested to be added to the character of the Lower Suban Agung Volcanic (LSAV) formation. LSAV in this well was found approximately 200 m shallower than the referenced model (Figure 6.1).

Intrusions appear in the bottom part of LSAV with less thickness and frequency from depth 1000 to 1100 (Figure 6.1). However, due to its granodiorite composition, these intrusions were correlated to the LSAV and associated with dacitic lavas.

The intrusions observations and mapping along the borehole have never been done in this field. Accordingly, the high intensity of diorite to basaltic diorite intrusions is advised to be applied as one of the Hululais Volcanic (HV) distinctive features.

SALP and USAV shares similarity in terms of composition. Both formations consist of andesitic composition that indicates a more effusive process than LSAV. LSAV was formed during a more explosive process of Mt. Suban Agung and deposited more acidic rock (dacitic lava, tuff, and granodiorite to diorite intrusions). HV shows the product of an effusive volcanic process like andesitic lava, associated with perpetual diorite and basaltic diorite intrusions.

Hululais Granodiorite Intrusion (HGI) comprises granodiorite and lavas that were possibly fractured by the tectonic motions surrounding the Agung Hulu and Hilir faults zone. The gamma-ray log adequately determines HGI in this well and is confirmed by the sidewall core samples. The more acidic rock, such as granodiorite, produces higher gamma-ray activity than the basic igneous rocks. Thus, the increase of gamma-ray in HGI formation is likely related to granodiorite occurrence.

The intrusions in this borehole were projected into a map and plotted with the structural geology and feed points locations to observe their correlation (Figure 6.2). The intrusions are likely related more to the stratigraphic control than structural geology. The intrusions were found in the bottom part of LSAV, HV, and HGI formations. Five feed points (at 1500, 1650, 1800, 1950, and 2050 m) were encountered in the HV formation within the fault system. However, only one feed point at 1800 m is associated with the intrusion (Figure 5.7).

There are no NW-SE lineaments apparent on the surface where the intrusions occurred at depth intervals of 1100 – 1500 m. Intrusions in the HV formation show no correlation to feed point occurrences and permeability. Moreover, intrusions were not observable in the interval depths 1500 – 1650 m where the two first feed points were measured, and the drilling possibly hit the Agung Hilir fault. Closer to the fault zones, the frequency of intrusions decreased, and the feed points were encountered. Four feed points were discovered inside the fault system between Agung Hilir and Agung Hulu faults, where the frequency of intrusions decreased (Figure 6.2).

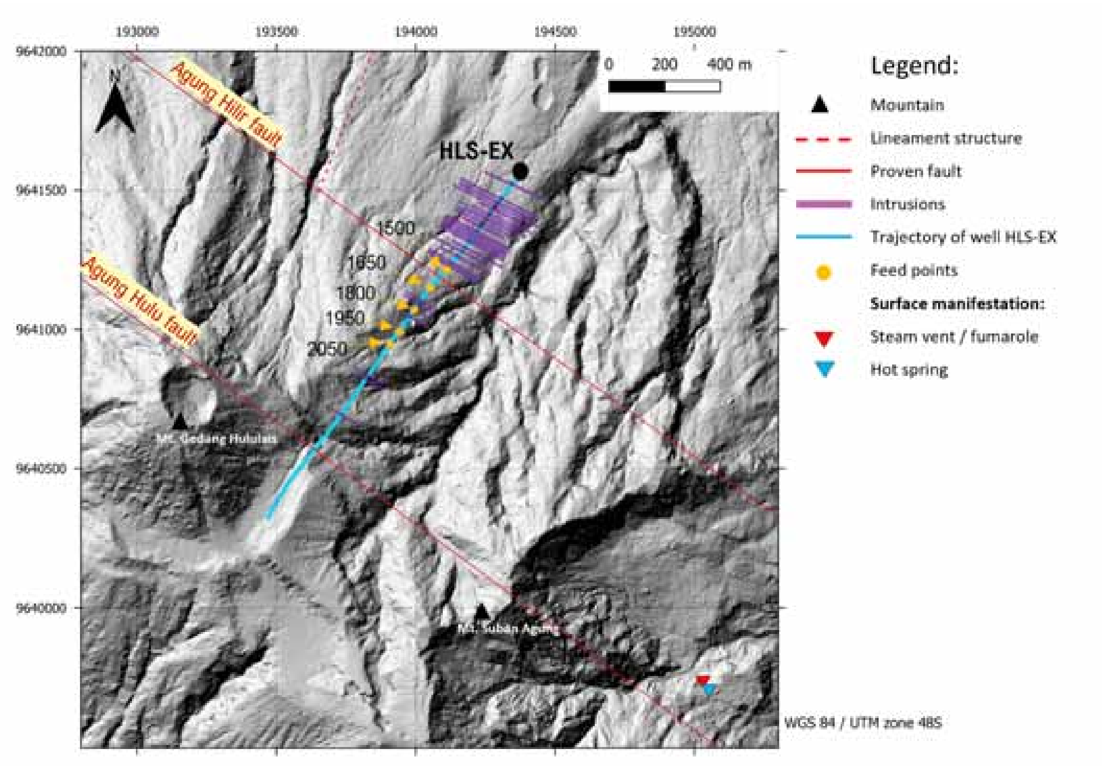

Figure 6.2 Intrusions mapping from the borehole of HLS-EX demonstrates a lack of correlation between the intrusion with the main faults and feed points.

In summary, there was no observable evidence in this borehole that the high frequency of intrusions increased the permeability. In fact, the loss circulation rate is very low in the depth that intrusions appear (Figure 5.8).

Alteration intensity in the intrusive rocks from HV formation is moderate to low. Meanwhile, intrusions in the LSAV formation show higher alteration intensity. The composition difference between the two formations more likely affects the alteration intensity instead of the intrusions frequency (Figure 5.7)

6.2 Mineral geothermometry

Each secondary mineral is susceptible to the condition of the hydrothermal fluid, mainly temperature and pH, and the host rock composition. Accordingly, some index minerals can be used as geothermometry to estimate the paleo-temperature and pH during the deposition, as suggested by Reyes (1990). Figure 6.3 shows the geothermometry index minerals that were found in the borehole and its corresponding temperature ranges. A neutral pH alteration suit is indicated by smectite, which is stable at a low temperature up to about 170 °C. Illite suggests temperature ranges of 220 – 310 °C, secondary biotite >280 °C, chlorite spans at 120 – 340 °C, secondary quartz at 180 to 320 °C, wairakite at 220 – 310 °C, epidote at >230 °C, actinolite at >280 °C, and anhydrite >180 °C. An acid pH mineral indicator is kaolinite, that stable at a temperature lower than 200 °C.

The maximum temperature from smectite and kaolinite delineates the low-temperature zone in the borehole (green area in Figure 6.3). In this zone, smectite and kaolinite overlap with secondary quartz, and there are no high-temperature minerals. The low-temperature zone possibly indicates a clay cap zone with an estimated temperature of less than 170 °C (Figure 6.3).

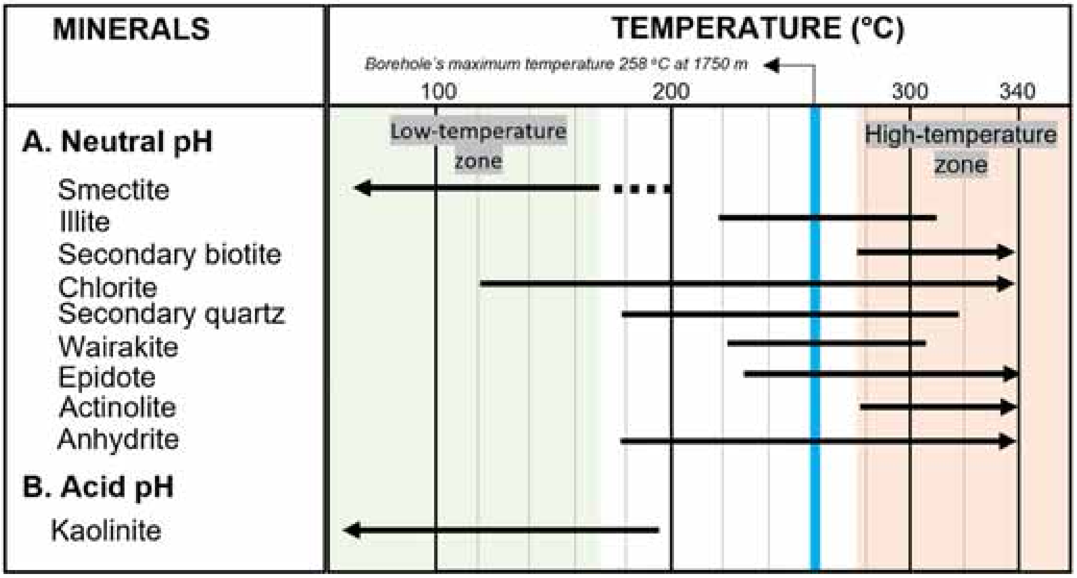

Figure 6.3 Applied mineral geothermometry to estimate the paleotemperature and pH during the hydrothermal alteration process in the borehole. The blue line indicates the highest measured temperature in the borehole.

The lowest margin of secondary biotite and actinolite delineates the high-temperature zone (the orange area in Figure 6.3). The high-temperature zone is expected to associate with the reservoir zone at minimum temperatures of around 280 °C. However, illite, wairakite, and epidote allow a reservoir zone temperature span from 230 °C. The highest temperature measured from the borehole is around 258 °C at 1750 m, which is slightly lower than the suggested by the geothermometry. Further discussion about borehole temperature and geothermometry is explained in Chapter 6.5.

6.3 Hydrothermal alteration zonation

The hydrothermal alteration zones were defined based on the secondary mineral assemblages discovered along the borehole. The top boundary of the hydrothermal alteration zone was estimated by the first appearance of an index alteration mineral.

The alteration zones mentioned from the surface are the weakly altered, smectite, mixed-layer clays, epidote-illite, and secondary biotite zone (Figure 5.8). The hydrothermal alteration zone in the borehole of HLS-EX is compared with the hydrothermal alteration model of the entire field suggested by Koestono et al. (2015) and Nusantara et al. (2017), and it is illustrated in Figure 6.4.

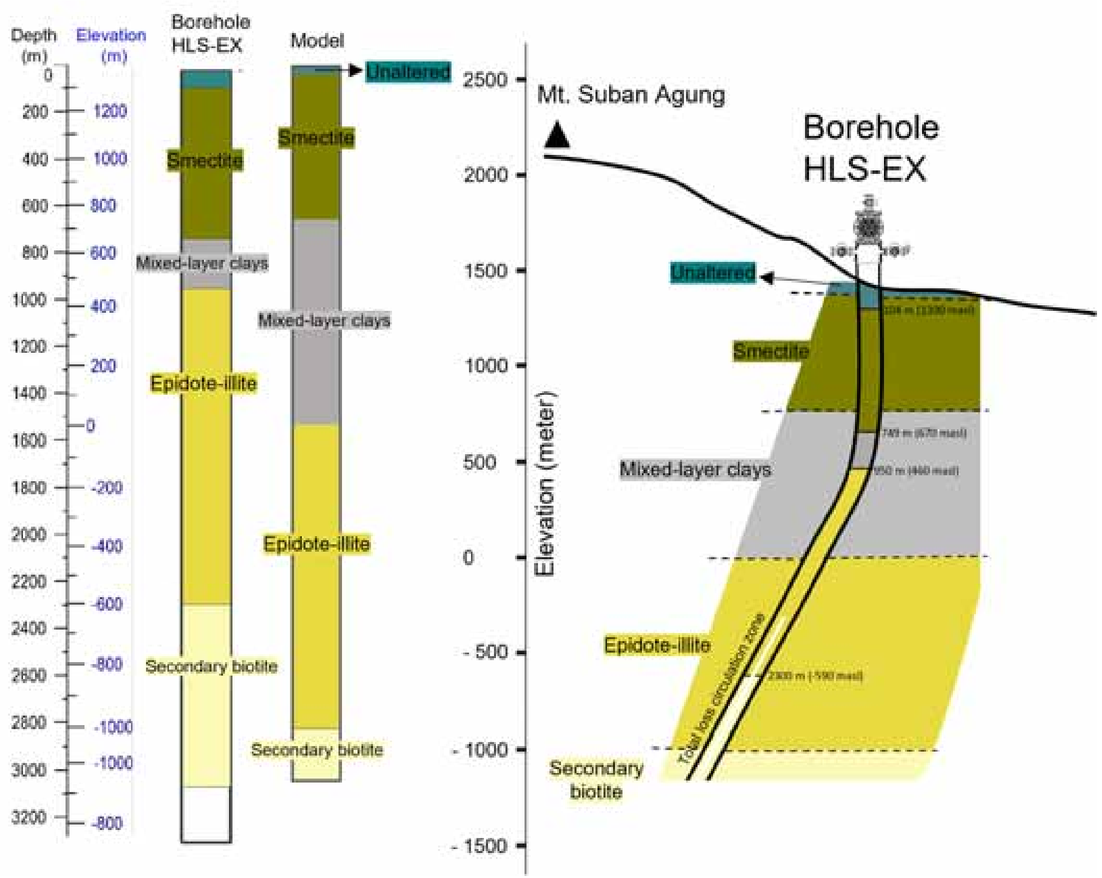

Figure 6.4 Illustration of hydrothermal alteration zone in borehole HLS-EX compared to the general alteration model of the Hululais geothermal field.

A minor amount of secondary minerals characterizes the weakly altered zone. The rocks in this zone are dominated by lava andesite, with alteration intensity ranging from 10 to 30%. The primary minerals such as plagioclase, K-feldspar, and pyroxene are undisturbed by hydrothermal alteration. The weakly altered zone is found from the surface to 104 m depth. However, no rock sample could be recovered at 26 – 55 m and 67 – 70 m depth due to the total loss circulation condition (Figure 5.8). The unaltered zone in the borehole is 70 m thicker compared to the suggested model.

The smectite zone is indicated by smectite and kaolinite identified in XRD. Moreover, the reactive clay (possibly smectite group) was also increased, reflected by the spikes in the methylene blue dye test log. The concentration of reactive clay in this zone reaches 51% at 476 m and gradually decreases to 15% at 527 m depth (Figure 5.8). The smectite zone appeared from depths 104 to 749 m in lava andesite and volcanic breccia. The bottom boundary of the smectite zone in the borehole is 30 m deeper than the model.

Mixed-layer clays (MLC) in the borehole contain a smectite/illite interlayer identified at 749 m (Table 5.3). The MLC zone was determined by the first occurrence of the MLC associated with the wairakite, chlorite, albite, and relict epidote. The MLC zone extends from 749 to 950 m. The MLC zone in the borehole appears thinner than the model.

The epidote-illite zone comprises of epidote, illite, chlorite, albite, and anhydrite. The mineral association in this zone suggests a temperature of at least 180 °C but possibly reached over 230 °C. Despite no cuttings being successfully recovered from a depth of 1937 m, the epidote-illite zone was estimated to extend from 950 to 2280 m depth (670 to -590 masl), following the distribution of the bottom boundary of the HV formation. The assumption was made that if the type of hydrothermal fluid does not change, the alteration minerals would likely be controlled by the composition of the rock formation. Thus, the alteration zone would tend to follow the formation zone. In addition, there was no secondary biotite found in the epidote-illite zone (Figure 5.8). The epidote-illite zone in the borehole appears about 460 m shallower than the model (Figure 6.4).

The secondary biotite zone was characterized by the secondary biotite, actinolite, and epidote. This zone was only recognized through the sidewall core (SWC) samples from depths 2286, 2290, 2300, 2400, 2420, 2440, 2500, and 2550 m. The mineral assemblages in this zone are suggested to reach more than 280 °C. The secondary biotite zone was delineated at depths of 2300 (first occurrence in SWC sample) to 2280 m, the TD well (Figure 5.8). The secondary biotite zone in the borehole was discovered about 600 m shallower (at -600 masl) than the model (at -1000 masl). It was also estimated to be about 300 m thicker than the model (Figure 6.4).

The significant discrepancy between the model and the finding in this study is the thickness of the MLC zone. The MLC zone boundary in this borehole was delineated based on XRD analysis and petrographic observations, respectively. However, only five samples were measured for XRD analysis, and they did not sufficiently cover the intervals 749 and 1550 m where the model depicted the MLC zone. Thus, more XRD analysis is suggested in samples from interval 749 – 1550 m for further study to clarify the bottom of the MLC zone in this borehole. Nevertheless, the stable illite was notified at 1550 m, which indicates the MLC zone is possibly thinner than the model.

6.5 Evolution of the borehole temperature and the estimation of the clay cap and reservoir zone

6.5.1 Evolution of the borehole temperature

The pressure and temperature (PT) profiles from the well were measured after two years of heating up. The measurement depths are presented as Y-axis in the meter unit, and the PT was plotted as the X-axis in bar and centigrade (°C) unit. The boiling point curve displays the PT with depth assuming boiling condition in the borehole. The geothermometry temperature suggested by Reyes (1990) is adopted and plotted into the profile to compare the current PT versus the paleo- conditions in the borehole.

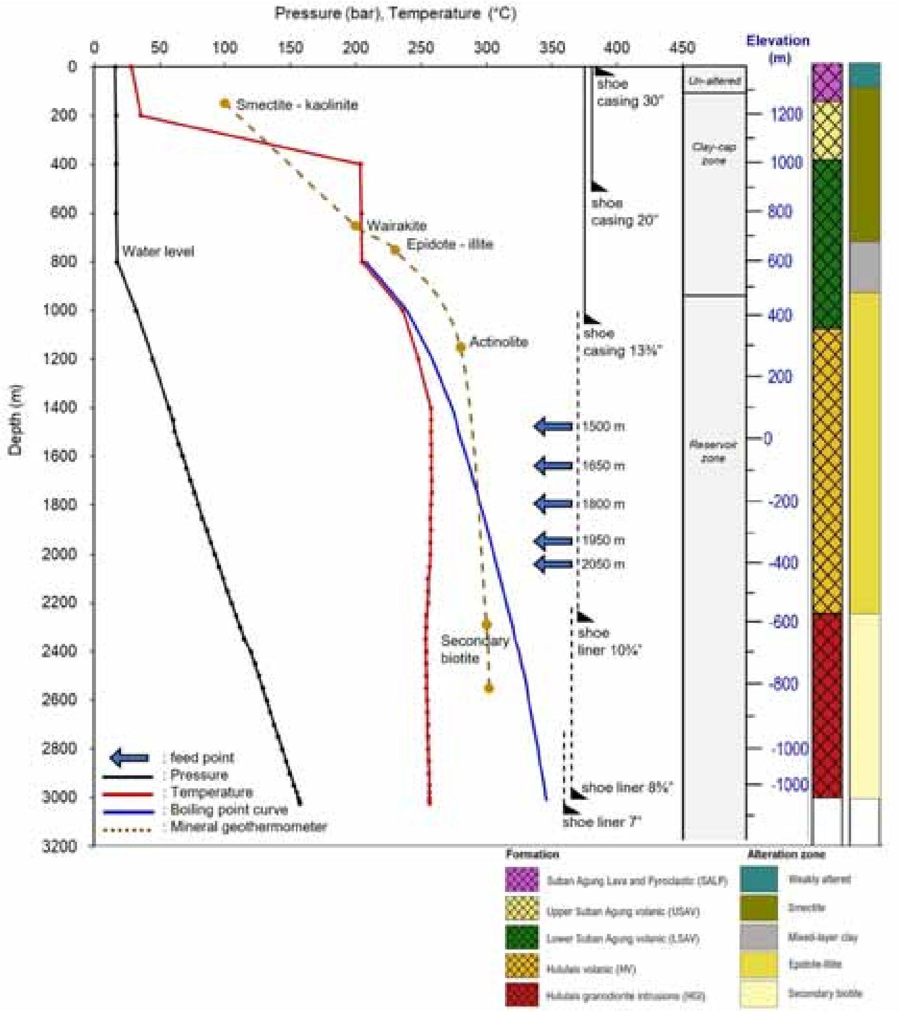

Figure 6.5 Measured pressure and temperature (PT) versus geothermometry profile

The current measured temperature falls below the boiling point curve suggesting the borehole is filled with the liquid phase. Two-phase fluid possibly located in depths of 800 – 1000 m, where the measured temperature line slightly overlapped with the boiling point curve. The measured temperature at 800 m is 205.08 °C with a boiling point temperature of 207.09 °C. In 1000 m, the measured temperature is 236.05 °C with a boiling point temperature of 238.99 °C. The sharp gradient point indicating the water level depth in the pressure profile is apparent at 800 m.

The trend of measured temperature is running almost parallel with the geothermometry trend. However, the geothermometry suggests a slightly higher temperature than the measured one, which deviates by about 50 °C. Temperature estimation based on geothermometry (Reyes, 1990) is likely to have a wide range of analytical errors due to the large temperature range for mineral stability in nature. Thus, the 50 °C temperature span does not absolutely suggest a cooling temperature in the borehole.

The measured temperature profile portrayed a conductive regime from the surface to 1200 m depth. The conductive regime is indicated by the steep increase in the temperature gradient. The temperature built up from 28 °C on the surface and reached 247 °C at 1200 m.

The convective regime in the measured temperature profile appears from depth 1200 to 3025 m. The convective regime shows a steadier temperature with no significant gradient. The temperature rose from 247 °C at 1200 m to 256 °C at 3025 m (bottom hole measured temperature). The highest measured temperature in the borehole is 258 °C at 1750 m. However, a slight temperature reversal trend was notable from 2050 to 3025 m depth. In this interval, the measured temperature decreased from 265.7 to 256.3 °C, gently declining about 9.4 °C (Figure 6.5).

6.5.2 Estimation of the clay cap and reservoir and zone

Correlation between the measured temperature distribution with the geothermometry, rock formation, and alteration zone was performed to estimate the depth of the clay cap and the reservoir zone in the borehole. The clay cap zone is pointed out by the smectite alteration and a steep conductive regime at 104 to 749 m depth, equivalent to 1300 to 460 masl (Figure 6.5). The Upper Suban Agung Volcanic (USAV) and Lower Suban Agung Volcanic (LSAV) formations dominate the rock types in the clay cap.

The mineral geothermometry in the clay cap zone estimated that a temperature around 100 °C was reached by the appearance of smectite and kaolinite. However, the measured temperature reached 203 °C (at 400 m depth) and was relatively unchanged until 800 m depth. The clay cap in the borehole is interpreted to have a steeper temperature gradient than suggested by the geothermometry and a slightly higher temperature (Figure 6.5).

The reservoir zone is indicated by the appearance of the convective regime and the high-temperature alteration mineral association. A geothermometry from epidote-illite, actinolite, and secondary biotite is applied in this zone, suggesting an initial borehole temperature of ~180 to more than 320 °C. The depth of 950 to 3025 m is estimated to represent the high-temperature reservoir zone (Figure 6.5). The Hululais Volcanic (HV) and Hululais Granodiorite (HGI) dominate the rock formation in the reservoir zone. The total loss of circulation (TLC) zone and the feed points were discovered in this interval, indicating a good well permeability within the reservoir.

6.6 Distinguishing the trend of magmatic differentiation and hydrothermal alteration

The magmatic composition is best represented in an unaltered rock whose original composition has not been altered. However, no chemistry data from the surface rocks are available to model the magmatic differentiation in Hululais geothermal field. Some components in the rocks were mobilized during the hydrothermal alteration process. Therefore, the least altered rock cuttings were selected to observe the magmatic differentiation in this study. Meanwhile, the compositional variation after the hydrothermal alteration process is pointed out in the highly altered cuttings. The processes responsible for the element variability observed in the rock samples are discussed in the following chapter.

6.6.1 Magmatic differentiation trends

Na_2O, K_2O, SiO_2, and Zr show an increasing concentration with decreasing MgO (Figure 5.16). These components are hosted in the alkali feldspars, quartz, and zircon, respectively. The crystallization of alkali feldspar, quartz, and zircon is typical in rhyolitic igneous rocks. These minerals were not observed as the major mineral phases in the weakly to moderately altered rock samples, which are dominated by andesitic composition (Figure 5.14). Moreover, rhyolites were not observed in the borehole. Thus, the increasing concentration of Na_2O, K_2O, SiO_2, and Zr can be explained by the incompatible nature of these elements in the mineral phases which have crystallized during the evolution of the magma observed in the borehole.

In the intermediate magma, plagioclase feldspar is one of the major mineral phases to crystallize. Plagioclase (although in many cases are strongly altered) was observed as the major primary mineral in the studied rocks. In the intermediate magma, plagioclase commonly has a bytownite to andesine composition (Gill, 2010). Thus, plagioclase crystallization increased Na_2O and SiO_2, and decreased CaO (and Sr, which replaces Ca in plagioclase structure) content of the residual melt during magma differentiation.

The decreasing of CaO is affected by the crystallization of pyroxene and hornblende, which appear as the microphenocrysts in the studied rock. The decrease of FeO concentration also implies the ferromagnesian mineral (clinopyroxene and hornblende) separation during fractional crystallization. The decreasing trend in FeO and TiO_2 indicates the crystallization of Fe-Ti oxides (ilmenite), which is possibly the major oxide among the opaque phases in the weakly altered rock in this study. Co, Cr, V, and Sc decrease show that these elements were mobilized from the melt during the ferromagnesian minerals and Fe-oxides crystallization (Figure 5.16).

6.6.2 Effect of hydrothermal alteration on element mobility

Some elements have proven to be actively mobile during hydrothermal alteration, which was observed as a strong deviation relative to the magmatic differentiation trend in the highly altered samples (Figure 5.17 and Figure 5.18). The trace elements Zr, Sr, Co, Cr, V, and Sc were strongly mobile relative to the magmatic differentiation trend due to the hydrothermal alteration (Figure 5.17 d, f, and Figure 5.18 i-l).

Several logs were produced to observe the variation of the major element loss and gain in the highly altered rocks relative to the weakly altered samples, which preserve the trend of magmatic differentiation (Figure 6.6).

SiO_2 content in the dacitic rocks of Lower Suban Agung volcanic (LSAV) formation is naturally increased by magmatic differentiation compared to the andesites of Suban Agung Lava and Pyroclastic (SALP) and Upper Suban Agung Volcanic (USAV). However, between the depth range of approximately 450 – 800 m, SiO_2 is enriched in the strongly altered rocks relative to what is expected by magma differentiation based on the highly altered dacitic rocks (Figure 6.6 a). Dacitic tuff from depth 551 m has the highest SiO_2 enrichments up to 71 wt.% and shows intense secondary quartz veins in the rock sample (Figure 5.17 a and Figure 5.9 d). The same SiO_2 enrichment is observed at a depth of 1000 – 1100 m. This SiO_2 gain is the result of silicification and can be confirmed by the presence of abundant secondary quartz in veins and vesicles in this depth range. Interestingly, at 851 – 950 m, SiO_2 loss can be observed. The SiO_2 leached at this depth might have been deposited in the formations above at depths 450 to 800 m (Figure 6.6 a).

As MgO was proposed as the least mobile element in the studied rocks, the increase of MgO is correlated with the occurrence of basalt and basaltic andesite rocks, and therefore the variation of MgO is related to the magmatic differentiation only (Figure 6.6 b).

Basaltic andesite rocks were observed at intervals of 77 m (5.48 wt%), 1121 – 1280 m (4 – 4.79 wt.%), and possibly at 1874 – 1916 (4.66 to 4.76 wt.%). MgO enrichment occurred at a highly altered tuff from 551 m, possibly led by the presence of clay minerals and opaque minerals that reach 12% and 8%, respectively, in this sample (Figure 6.6 b).

A highly altered basalt from a depth of 884 m is apparent from the TAS diagram with 2.43 wt.% of MgO and 51.35 wt.% of SiO_2 content (Figure 5.14). This sample is located in the depths where the SiO_2 leaching occurred (Figure 6.6 a). Thus, the sample possibly originated from the andesite that lost the SiO_2 due to hydrothermal alteration.

K_2O enrichment relative to the magma differentiation trend was observed in the volcanic breccia from LSAV formation at a depth of 452 m and intervals of 749 – 1082 m (Figure 6.6 c). The K_2O gain was possibly caused by illitization, as indicated from a sample at 749 m where the illite/smectite MLC was identified. However, illite was not detected in the sample at 452 m. The clay composition contains smectite, kaolinite, and chlorite at this depth (Figure 5.12).

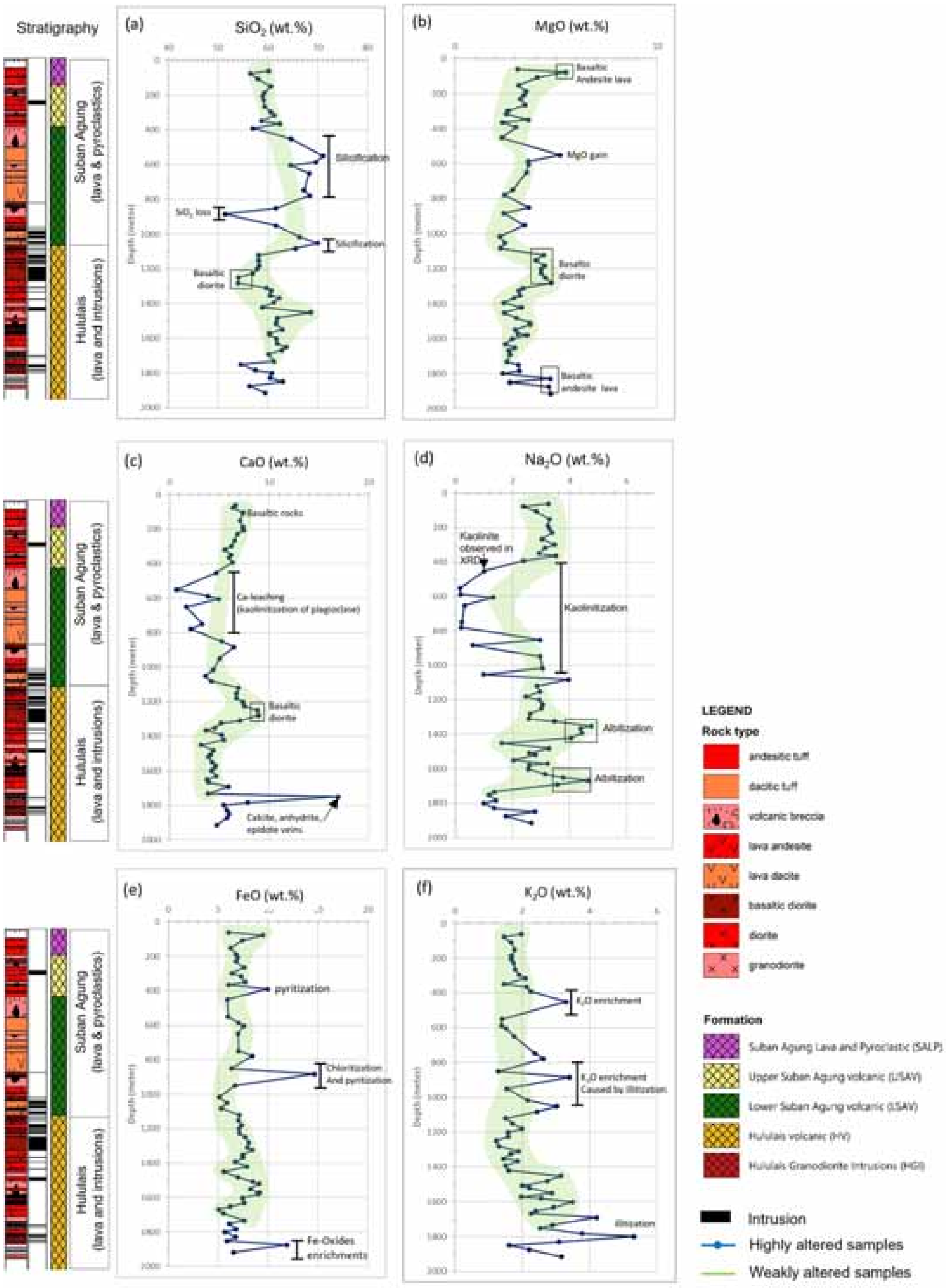

Figure 6.6 Element concentration in highly altered rocks (blue line) was plotted relative to the compositional range of magmatic differentiation trend (green zone) to observe the chemical process that occurred in the borehole e.g., silicification, illitization, kaolinitization, albitization, chloritization, pyritization, iron and Ca enrichment.

CaO concentration is the highest in the moderately altered basaltic diorite formations at the depth range of 1120 – 1310 m. CaO content in dacitic rocks of LSAV is lower than basaltic to andesitic rock in the other formations (Figure 6.6 d) in accordance with magma differentiation. Calcium leaching is observable at depths 452 – 779 m related to the rock's kaolinitization. Kaolinitization of plagioclase confirmed by XRD is shown at depth 452 m (Figure 5.12). The excess of CaO in an outlier sample at the depth of 1751 m was likely caused by the abundance of Ca-rich secondary minerals (calcite, anhydrite, and epidote) as the vein filling deposits (Figure 6.7).

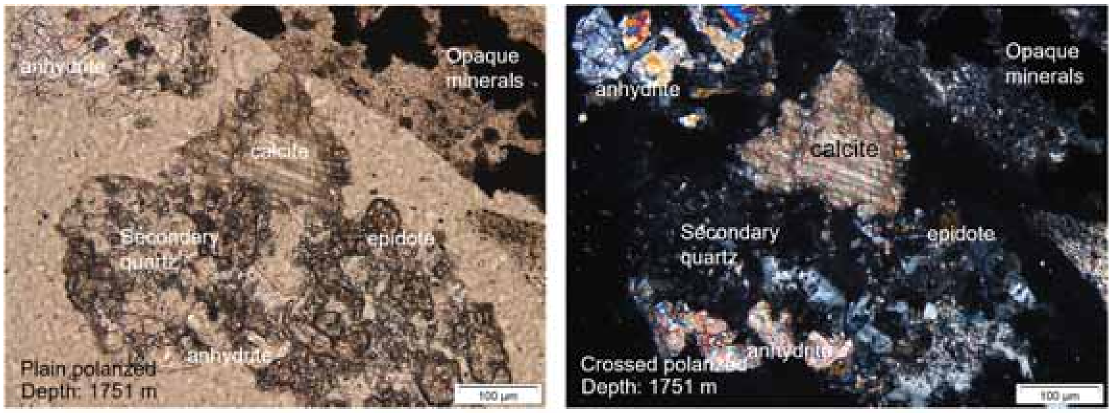

Figure 6.7 Calcite (13%), anhydrite (6%), and epidote (3%) dominate the composition of secondary minerals in the veins at sample depth 1751 m and show an excess of CaO concentration in the sample.

Albitization in Ca-plagioclase increased the Na_2O content at lava depths 1352 – 1421 m and 1652 – 1733 m (Figure 5.17 a). Albitization also caused the depletion in CaO with the reaction:

$$\underset{\text{Plagioclase}}{Na_4CaAl_6Si_{14}O_{40}} + H_2O_{(aq)} = \underset{\text{Albite}}{4NaAlSi_3O_8} + Ca^{2+} + 2AlO_2^- + 2SiO_2 + H_2O$$

Na_2O content in the LSAV formation was leached out of the system at depths of 400 – 800 m (Figure 6.6 e). Kaolinitization in plagioclase leads to the loss of Na_2O (Figure 5.17 a). Na-plagioclase (albite) is altered into kaolinite which leads to the loss of Na_2O with the reaction:

$$\underset{\text{Albite}}{2NaAlSi_3O_8} + 9H_2O_{(l)} + 2H^+_{(aq)} = \underset{\text{Kaolinite}}{Al_2Si_2O_5(OH)_4} + 2Na^+_{(aq)} + \underset{\text{silicic acid}}{4H_4SiO_{4(aq)}}$$

Both albitization and kaolinization processes were confirmed by petrographic and XRD analysis (Figure 5.10 e and Figure 5.12).

FeO gain were observed at depths 392, 884, and 1874 m (Figure 6.6 f). FeO gain relative to the magmatic differentiation trend caused by the chloritization in Fe-Mg minerals (Figure 5.18 g). Moreover, pyrite (FeS_2) deposition from hydrothermal fluid also contributes to the FeO enrichment in the altered rocks, as pyrite is abundant in the sample's rock veins (Figure 5.9 h). The outliers appear in sample depths of 884 m and 1874 m showing an excess of FeO induced by the abundance of pyrite and Fe-oxides minerals (Figure 6.8).

Figure 6.8 The abundance of pyrite and Fe-oxides minerals causes the excess of FeO relative to the magmatic differentiation trend observed at samples from 884 and 1874 m.

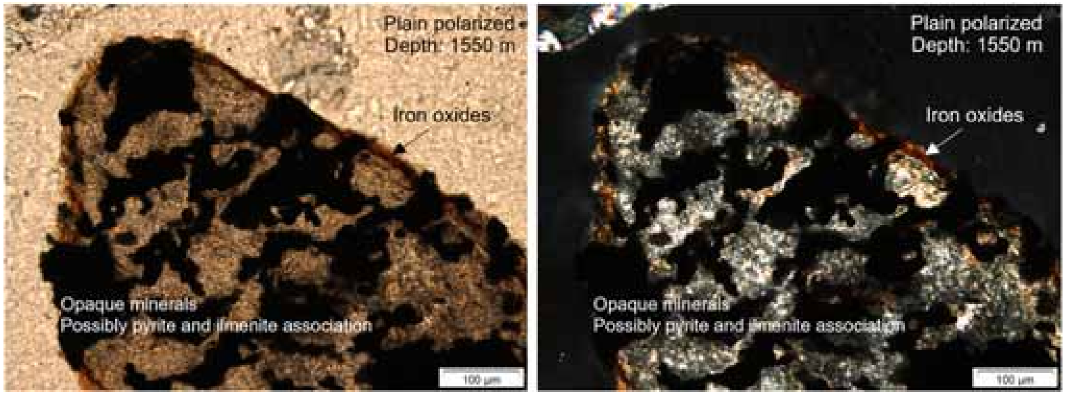

Figure 6.9 Highly altered andesitic breccia from a depth of 1550 m shows abundant Fe-riched minerals and opaque minerals (possibly pyrite and ilmenite).

7 Conclusions

The borehole geology study of well HLS-EX, Hululais geothermal field concludes that:

1. The altered rocks from lava andesite and dacite, basaltic diorite and diorite, andesitic and dacitic tuff, and volcanic breccia compose the stratigraphy in borehole HLS-EX. Subsurface rock formations identified from the surface to the deeper part of the borehole are The Suban Agung Lava and Pyroclastic (SALP), the Upper Suban Agung Volcanic (USAV), the Lower Suban Agung Volcanic (LSAV), the Hululais Volcanic (HV), and the Hululais Granodiorite Intrusions (HGI). The stratigraphy confirms the previous model with slight thickness differences in formations.

2. Smectite, kaolinite, illite, epidote, MLC, wairakite, anhydrite, secondary biotite, and actinolite are the secondary mineral assemblages that characterize the hydrothermal alteration in the borehole. The hydrothermal alteration zones from the borehole were determined as the weakly altered zone, smectite zone, MLC zone, epidote-illite zone, and secondary biotite zone. The MLC zone was identified as thinner, and the secondary biotite zone was discovered to be shallower and thicker than the suggested model.

3. The secondary mineral assemblages indicate that borehole HLS-EX is a high-temperature well, and it fits with the highest temperature measured in the borehole, which reached 258 °C. The measured borehole temperature trend is similar to the geothermometry profile, although it has a slightly lower temperature. Permeability was proven from the total loss circulation and productive feed points discovered in the well.

4. The hydrothermal alteration process significantly shifted the magmatic composition in the rock from borehole HLS-EX. Major elements such as SiO_2, K_2O, CaO, Na_2O, and TiO_2 were intensively mobilized during the hydrothermal alteration process. FeO was slightly mobilized, and MgO is the least mobile element.

References

Arifin, M. T., Nurseto, S. T., Nusantara, V. D., Pratama, G. R., Marastio, F. E., & Thamrin, M. H. (2020). Feed zone evaluation in Hululais field, Bengkulu, Indonesia. *Proceedings 42nd New Zealand Geothermal Workshop 24-26 November 2020.* Waitangi.

Arnórsson, S., Thórhallsson, S., & Stefánsson, A. (2015). Utilization of Geothermal Resources. In H. Sigurdsson, B. Houghton, H. Rymer, J. Stix, & S. McNutt, *The Encyclopedia of Volcanoes* (pp. 1235–1252). Elsevier Inc. All rights reserved.

Baker Hughes INTEQ. (1996). *Wellsite geology, reference guide.* Houston: Baker Hughes INTEQ.

Boss, C. B., & Fredeen, K. J. (2004). *Concepts, instrumentation, and techniques in inductively coupled plasma optical emission spectrometry* (3rd ed.). Shelton: PerkinElmer Inc.

Browne, P. (1984). *Lectures on geothermal geology and petrology.* National energy authority. Reykjavik: UNU geothermal training programme. Retrieved from https://orkustofnun.is/gogn/unu-gtp-report/UNU-GTP-1984-02.pdf

Budiardjo, B., Hantono, D., Setyabudi, H. A., & Nugroho. (2001). Geochemical characterization of thermal waters in Hululais geothermal prospect. *Stanford geothermal workshop*, (p. 9). Stanford.

Chen, P. Y. (1977). *Table of key lines in X-ray powder diffraction patterns of minerals in clays and associated rocks.* Bloomington: Authority of the state of Indiana.

Darma, S., Imani, Y. L., Shidqi, N. A., Riyanto, T. D., & Daud, M. Y. (2021). Country Update: The Fast Growth of Geothermal Energy Development in Indonesia. *Proceedings World Geothermal Congress 2020+1, April - October 2021* , (p. 8). Reykjavik.

Darman, H., & Sidi, H. (2000). An outline of the geology of Indonesia. *Indonesian Association of Geologists*, 193.

Earle, S. (2015). *Physical geology.* Victoria: BCcampus. Retrieved from https://opentextbc.ca/geology/

Fisher, R. V. (1961). Proposed classification of volcaniclastic sediments and rocks. *Geol Soc Am Bull 72*, 1409-1414.

Gill, R. (2010). *Igneous rocks and processes: a practical guide.* London: John Wiley & Sons Ltd.

Hall, R. (2009). Indonesia, Geology. In R. Gillespie, & D. Clague, *Encyclopedia of Islands* (pp. 454 - 460). Berkeley: University of California Press. doi:10.1525/9780520943728-104

Juanda, A. A., Wardhani, A. D., & Raharjo, I. B. (2015). Microearthquake (MEQ) Investigation Reveals the Sumatran Fault System in Hululais Geothermal Field, Bengkulu, Indonesia. *Proceedings World Geothermal Congress 2015 Melbourne, Australia, 19-25 April 2015.* Melbourne.

Koestono, H., Prasetyo, I. M., Nusantara, V. D., Thamrin, M. H., & Kamah, M. Y. (2015). Hydrothermal alteration mineralogy of well HLS-C, Hululais geothermal field, Bengkulu, Indonesia. *Proceedings World Geothermal Congress 2015*, (p. 5). Melbourne.

Kohno, I., Tanabe, K., & Tomita, T. (1993). Determination of clay minerals by the ignition loss method using a muffle furnace. *Memoirs of the faculty of engineering, Okayama University, Vol.28, No.1, November 1993*, 51-59.

Le Bas, M., Le Maitre, R., Streckeisen, A., & Zanettin, B. (1986). IUGS Subcommission on the systematics of igneous rocks, A chemical classification of volcanic rocks based on the Total Alkali-Silica diagram. *Journal of petrology Volume 27, Issue 3, June 1986*, 745-750. doi:10.1093/petrology/27.3.745

Lindal, B. (1973). Industrial and other application of geothermal energy. In H. Armstead, *Geothermal energy, UNESCO* (pp. 135-148). Paris.

McPhie, J., Doyle, M., & Allen, R. L. (1993). *Volcanic textures: a guide to the interpretation of textures in volcanic rocks.* Tasmania: June Pongrarz.

Moore, D., & Reynolds, R. (1997). *X-ray diffraction and the identification and analysis of clay minerals* (2nd ed.). New york: Oxford university press inc.

Mulyadi. (1995). Interpretation of geoelectric structure at Hululais prospect area, South Sumatra. *Proceedings 17th NZ Geothermal Workshop*, (pp. 133-137).

Natawidjaja, D. H., & Triyoso, W. (2007). The Sumatran fault zone - from source to hazard. *Journal of Earthquake and Tsunami*, 21-47. doi:10.1142/S1793431107000031

Nurseto, S. T., Arifin, M. T., Pratama, G. R., Nusantara, V. D., Thamrin, M. H., & Suryantini, N. (2021). Structural geology and volcanism in Hululais geothermal area, Bengkulu, Indonesia. *ITB International Geothermal Workshop 2020. 732*, pp. 1 - 9. Bandung: IOP Conf. Series: Earth and Environmental Science. doi:10.1088/1755-1315/732/1/012004

Nusantara, V. D., Prasetyo, I. M., Thamrin, M. H., & Siahaan, E. E. (2016). Integrated petrology analysis: a guide to successful exploration in Hululais field. *Proceedings The 4th Indonesia International Geothermal Convention & Exhibition 10-12 August 2016.* Jakarta.

Nusantara, V. D., Prasetyo, I. M., Thamrin, M. H., & Siahaan, E. E. (2017). 3D geological modelling: an advance method to build geological baseline model in Hululais geothermal prospect, Bengkulu, Indonesia. *Proceedings 39th New Zealand Geothermal Workshop 22-24 November 2017.* Rotorua.

Nusantara, V. D., Pratama, G. R., Nurseto, S. T., Arifin, M. T., & Thamrin, M. H. (2020). Characterization of Hululais subsurface rock formation and its implication to strato volcano facies model, Huluais geothermal field, Indonesia. *Proceedings 42nd New Zealand Geothermal Workshop 24-26 November 2020.* Waitangi.

Pratama, G. R., Nusantara, V. D., Sapto, T. N., Arifin, M. T., & Thamrin, M. H. (2020). Volcanostratigraphy of Hululais geothermal field, Bengkulu, Indonesia. *42nd New Zealand Geothermal Workshop*, (p. 8). Waitangi.

PT Pertamina. (1994). *Scientific model of the Hululais geothermal resource - internal report of the exploration geothermal division Pertamina.* Jakarta.

PT Pertamina Geothermal Energy. (2018). *Final well report drilling well HLS-E (unplublished).* Jakarta: PT Pertamina Geothermal Energy.

PT Pertamina Geothermal Energy. (2021). *Laporan geologi lapangan hululais.* Exploration Geoscience Region I. Jakarta: Unpublished.

PT Pertamina Geothermal Energy Indonesia. (2021). *Geological map of Hululais geothermal field.* Jakarta: PT Pertamina Geothermal Energy Indonesia.

Reyes, A. (1990). Petrology of Philippine geothermal systems and the application of alteration mineralogy in theis assessment. *J. Volcanol. Geotherm. Res. Vol 43*, 279-309.

Sieh, K., & Natawidjaja, D. (2000, December 10). Neotectonics of the Sumatran Fault, Indonesia. *Journal of geophysical research Vol. 105, No. B12*, 28295 - 28326.

The Ministry of Economy, Trade and Industry Indonesia. (2011). *Study on economic partnership projects in developing countries in FY2010 study on geothermal power development project in Hululais, Indonesia.* Jakarta: The Ministry of Economy, Trade and Industry Indonesia.

Utami, P. (2011). *Hydrothermal alteration and evolution of the Lahendong geothermal system, North Sulawesi, Indonesia. Dissertation.* Auckland: University of Auckland.

Whitman , C., Iddings, J., & Pirsson, L. (1906). The Texture of Igneous Rocks. *The Journal of Geology Vol. 14, No. 8 (Nov. - Dec.,1906)*, 692-707. doi:10.1086/621356

Appendix A – The result of ICP-OES

No	Depth	Alteration intensity	Rock texture	SiO_2	Al_2O_3	FeO	MnO	MgO	CaO	Na_2O	K2O	TiO_2	P_2O_5	Total oxide
	meter	%							wt.%					
1	62	15	CL	60.10	17.68	6.03	0.11	3.12	6.64	3.26	1.97	0.80	0.17	99.89
2	77	35	CL	56.46	16.84	9.49	0.19	5.48	6.40	2.39	1.45	1.04	0.14	99.88
3	107	30	CL	58.00	17.26	7.41	0.14	4.10	7.41	2.84	1.66	0.91	0.16	99.88
4	152	10	CL	60.57	16.74	6.25	0.11	3.16	7.07	3.30	1.77	0.77	0.15	99.89
5	188	35	CL	59.23	16.88	6.79	0.13	3.51	7.40	3.24	1.68	0.85	0.17	99.88
6	206	25	CL	58.92	16.99	6.93	0.13	3.42	7.43	3.30	1.68	0.91	0.16	99.88
7	230	10	CL	59.13	17.59	6.77	0.12	3.25	6.83	3.39	1.74	0.87	0.17	99.88
8	266	40	INT	59.37	16.82	7.57	0.14	3.47	6.54	3.04	1.78	0.98	0.17	99.88
9	299	25	CL	60.51	17.54	6.35	0.17	2.63	6.23	3.48	1.91	0.89	0.17	99.88
10	317	40	VB	61.28	16.48	7.27	0.34	2.56	5.57	3.15	2.09	0.99	0.16	99.88
11	350	40	CL	58.71	18.03	7.69	0.16	3.64	6.16	2.92	1.46	0.95	0.16	99.89
12	365	15	CL	62.37	16.48	5.99	0.11	2.37	5.96	3.51	2.12	0.80	0.17	99.89
13	392	55	PT	56.98	17.60	9.94	0.17	3.03	6.35	2.40	2.24	0.98	0.18	99.88
14	452	65	VB	64.62	17.16	5.90	0.13	2.34	4.70	1.01	3.30	0.66	0.11	99.92
15	551	50	PT	71.07	14.13	5.98	0.11	5.20	0.73	0.16	1.39	1.03	0.15	99.93
16	587	50	PT	69.65	12.64	7.04	0.21	3.62	3.88	0.18	1.38	1.05	0.21	99.86
17	605	40	CL	64.49	15.08	7.54	0.20	3.65	4.95	1.32	1.53	0.94	0.21	99.89
18	650	60	VB	68.27	16.07	7.00	0.11	3.55	1.71	0.32	1.75	0.94	0.19	99.91
19	749	60	CL	67.23	15.71	7.06	0.09	2.87	3.29	0.22	2.38	0.90	0.17	99.92
20	779	50	CL	68.35	14.74	8.39	0.07	2.46	2.15	0.19	2.62	0.81	0.14	99.93
21	851	50	CL	61.53	17.80	6.32	0.13	3.65	5.28	2.96	1.29	0.81	0.13	99.90
22	884	65	VB	51.35	19.68	14.62	0.10	2.43	6.49	0.60	3.40	1.08	0.16	99.91
23	950	60	CL	61.62	17.53	6.68	0.15	3.44	5.04	2.97	1.54	0.81	0.13	99.90
24	1016	45	CL	66.32	15.69	5.10	0.13	2.22	4.42	3.05	2.15	0.65	0.15	99.90
25	1052	55	CL	69.98	12.83	5.84	0.15	2.49	3.61	0.99	3.03	0.81	0.19	99.92
26	1082	55	CL	65.51	15.18	5.32	0.16	2.26	4.24	3.96	2.44	0.58	0.16	99.80
27	1121	50	CL	58.14	17.72	7.13	0.19	4.39	6.96	2.85	1.51	0.84	0.17	99.89
28	1151	40	INT	58.13	18.17	7.02	0.18	4.02	6.72	2.96	1.71	0.81	0.17	99.89
29	1181	40	INT	58.22	17.39	7.35	0.23	4.44	6.71	2.46	1.99	0.89	0.20	99.88
30	1202	40	INT	57.76	17.48	7.10	0.21	4.26	7.40	2.94	1.57	0.94	0.21	99.88
31	1226	30	INT	56.97	17.96	7.16	0.22	4.27	7.53	3.06	1.59	0.92	0.22	99.88
32	1250	30	INT	54.13	19.16	7.68	0.19	4.48	8.84	3.02	1.22	0.95	0.20	99.86
33	1280	30	INT	54.08	18.69	8.06	0.19	4.78	8.95	2.63	1.30	0.98	0.22	99.88
34	1310	30	CL	59.75	15.94	7.88	0.23	3.37	7.10	2.57	1.89	0.93	0.23	99.90
35	1325	30	CL	60.64	15.69	8.41	0.21	3.16	5.20	3.49	1.66	1.06	0.38	99.90
36	1352	35	CL	60.40	16.51	7.45	0.18	3.23	4.57	4.76	1.44	1.02	0.33	99.90
37	1367	35	CL	62.25	15.79	7.47	0.17	2.94	3.69	4.39	1.87	0.98	0.35	99.90
38	1394	35	CL	61.15	16.86	6.68	0.20	2.42	5.25	4.44	1.51	1.00	0.39	99.89
39	1421	35	CL	58.82	17.31	7.86	0.24	3.29	5.45	4.05	1.60	0.98	0.29	99.89
40	1451	40	VB	68.57	14.29	5.55	0.17	2.45	3.19	1.63	3.15	0.64	0.18	99.81
41	1481	40	VB	61.86	16.31	6.99	0.22	3.04	4.38	3.29	2.74	0.86	0.20	99.89
42	1508	40	VB	61.68	15.50	8.45	0.26	3.71	4.14	2.58	2.00	1.27	0.31	99.90
43	1520	40	VB	61.58	14.61	9.05	0.27	3.73	3.95	2.79	2.20	1.36	0.35	99.90
44	1550	45	VB	62.94	14.70	8.19	0.29	2.98	4.28	2.03	2.88	1.24	0.36	99.90
45	1571	45	CL	60.23	15.63	9.12	0.28	3.13	4.64	3.22	1.96	1.22	0.45	99.88
46	1580	45	CL	60.36	15.54	8.98	0.26	3.58	4.55	2.59	2.56	1.10	0.38	99.89
47	1601	45	CL	61.65	15.87	7.45	0.22	2.84	4.22	2.56	3.48	1.19	0.41	99.89
48	1631	45	CL	61.92	15.53	7.58	0.29	2.50	4.72	3.14	2.93	0.92	0.35	99.88
49	1652	40	CL	63.69	15.92	6.16	0.20	2.96	3.76	3.78	2.40	0.73	0.28	99.89
50	1667	40	CL	62.83	17.16	5.05	0.21	2.69	3.91	4.66	2.26	0.81	0.31	99.90
51	1691	50	VB	60.12	16.74	5.49	0.17	2.72	5.92	3.56	4.21	0.71	0.20	99.85
52	1733	40	VB	61.12	19.17	7.62	0.28	2.59	3.90	1.36	2.89	0.73	0.20	99.86
53	1751	70	VB	54.57	14.43	6.09	0.26	3.16	16.95	1.18	2.53	0.56	0.16	99.88
54	1784	60	CL	57.48	18.02	6.76	0.25	3.20	7.83	1.40	3.79	0.88	0.28	99.89
55	1799	55	INT	60.71	17.95	5.69	0.17	2.38	5.44	0.99	5.32	0.93	0.31	99.88
56	1829	65	INT	60.40	16.43	6.74	0.28	4.71	5.79	1.36	3.08	0.80	0.21	99.80
57	1850	65	CL	63.02	16.98	5.85	0.23	2.73	5.96	2.79	1.61	0.54	0.14	99.84
58	1874	65	CL	56.27	16.06	11.86	0.26	4.66	5.75	1.76	2.20	0.84	0.16	99.84
59	1916	65	CL	59.43	17.18	6.54	0.24	4.76	4.76	2.65	3.17	0.83	0.27	99.83
60	1571b	45	CL	59.63	16.17	9.10	0.27	3.09	4.66	3.32	1.99	1.22	0.44	99.89

CL: coherent lava, INT: intrusions, VB: volcanic breccia, PT: pyroclastic tuff.

No	Depth	Alteration intensity	Rock texture	Ba	Co	Cr	Cu	Ni	Sc	Sr	V	Y	Zn	Zr
	meter	%		μg/g										
1	62	15	CL	325	14	23	43	22	18.9	322	123	26.3	66	155
2	77	35	CL	300	26	76	54	33	30.9	268	199	24.2	82	138
3	107	30	CL	308	19	54	48	24	28.0	297	176	23.1	73	144
4	152	10	CL	300	15	23	51	21	20.2	321	147	22.4	72	145
5	188	35	CL	312	17	36	52	21	22.7	335	154	21.4	72	136
6	206	25	CL	316	17	33	69	27	23.3	339	170	21.8	80	139
7	230	10	CL	325	17	25	70	44	24.6	334	157	23.3	73	138
8	266	40	INT	325	18	24	57	24	24.6	303	169	23.0	81	139
9	299	25	CL	348	16	19	80	10	21.7	315	157	24.2	75	150
10	317	40	VB	389	18	22	71	39	21.7	250	164	23.2	86	145
11	350	40	CL	248	18	22	57	41	23.3	299	193	24.6	82	123
12	365	15	CL	344	14	20	52	15	18.8	290	139	22.0	77	145
13	392	55	PT	211	20	212	47	17	26.5	257	188	21.3	117	118
14	452	65	VB	231	13	18	37	24	18.7	118	138	19.5	69	118
15	551	50	PT	152	13	30	13	5	19.1	24	145	24.6	85	166
16	587	50	PT	236	14	18	46	8	18.9	53	142	26.4	623	214
17	605	40	CL	310	18	25	41	11	19.9	200	145	26.9	112	184
18	650	60	VB	273	14	16	38	19	20.9	77	152	27.9	38	179
19	749	60	CL	274	15	10	46	8	18.7	50	157	29.4	35	190
20	779	50	CL	246	12	12	12	1	19.1	40	146	22.6	50	136
21	851	50	CL	223	16	24	43	15	20.3	296	163	21.6	64	123
22	884	65	VB	208	23	23	6	1	18.3	169	170	22.6	95	152
23	950	60	CL	164	15	17	46	8	19.6	322	145	22.2	67	132
24	1016	45	CL	311	11	10	44	10	13.3	300	103	21.5	79	141
25	1052	55	CL	251	12	22	34	10	15.2	106	111	24.5	64	163
26	1082	55	CL	415	10	71	797	67	13.5	293	82	26.5	66	163
27	1121	50	CL	224	17	29	50	19	21.0	348	156	20.6	87	95
28	1151	40	INT	237	15	23	54	20	20.5	363	145	19.0	73	92
29	1181	40	INT	288	20	43	89	35	23.5	324	177	21.4	112	110
30	1202	40	INT	255	19	37	89	34	24.0	361	168	21.2	110	122
31	1226	30	INT	249	19	38	64	36	23.4	372	163	20.7	127	118
32	1250	30	INT	224	20	32	127	48	26.5	408	214	21.9	138	100
33	1280	30	INT	220	22	39	69	28	28.5	401	197	19.3	121	91
34	1310	30	CL	215	16	10	38	10	21.3	299	120	26.0	125	107
35	1325	30	CL	187	13	8	27	8	23.9	317	89	40.5	140	150
36	1352	35	CL	198	14	29	22	7	25.0	373	71	39.2	118	144
37	1367	35	CL	204	13	12	20	7	23.6	354	105	35.4	112	139
38	1394	35	CL	197	13	14	22	6	22.9	405	106	37.5	108	149
39	1421	35	CL	206	15	50	32	29	24.9	375	107	33.3	109	108
40	1451	40	VB	332	9	69	585	272	17.5	165	57	32.1	204	132
41	1481	40	VB	324	13	21	43	10	22.4	262	116	30.1	129	130
42	1508	40	VB	200	17	17	27	7	27.7	178	138	37.2	170	138
43	1520	40	VB	255	17	14	18	6	27.3	185	77	42.3	164	145
44	1550	45	VB	364	17	4	20	16	27.0	177	73	42.0	129	145
45	1571	45	CL	292	16	8	12	10	25.5	274	97	42.5	232	155
46	1580	45	CL	286	15	25	15	15	24.9	232	71	42.7	201	145
47	1601	45	CL	337	14	28	24	9	26.8	215	109	41.7	155	162
48	1631	45	CL	334	12	6	14	16	23.1	242	31	47.3	271	164
49	1652	40	CL	321	12	32	17	7	20.2	277	64	39.6	165	165
50	1667	40	CL	253	9	21	15	10	17.1	312	83	30.9	120	156
51	1691	50	VB	430	12	46	93	162	16.0	354	75	26.9	123	142
52	1733	40	VB	287	20	86	71	43	26.8	286	194	44.8	133	176
53	1751	70	VB	252	12	134	38	49	15.8	338	95	27.5	147	130
54	1784	60	CL	325	16	41	32	15	22.7	186	128	34.2	166	167
55	1799	55	INT	523	14	19	37	7	22.5	151	137	32.3	119	164
56	1829	65	INT	427	20	164	74	44	25.8	230	155	21.7	725	99
57	1850	65	CL	276	11	25	29	16	12.1	448	75	18.6	654	83
58	1874	65	CL	368	18	190	68	78	24.1	235	177	23.2	342	91
59	1916	65	CL	619	15	108	63	68	19.5	241	127	27.7	325	129
60	1571b	45	CL	234	15	6	20	10	26.3	283	100	43.1	183	158

CL: coherent lava, INT: intrusions, VB: volcanic breccia, PT: pyroclastic tuff.

Appendix B – Rock type depths in the borehole log

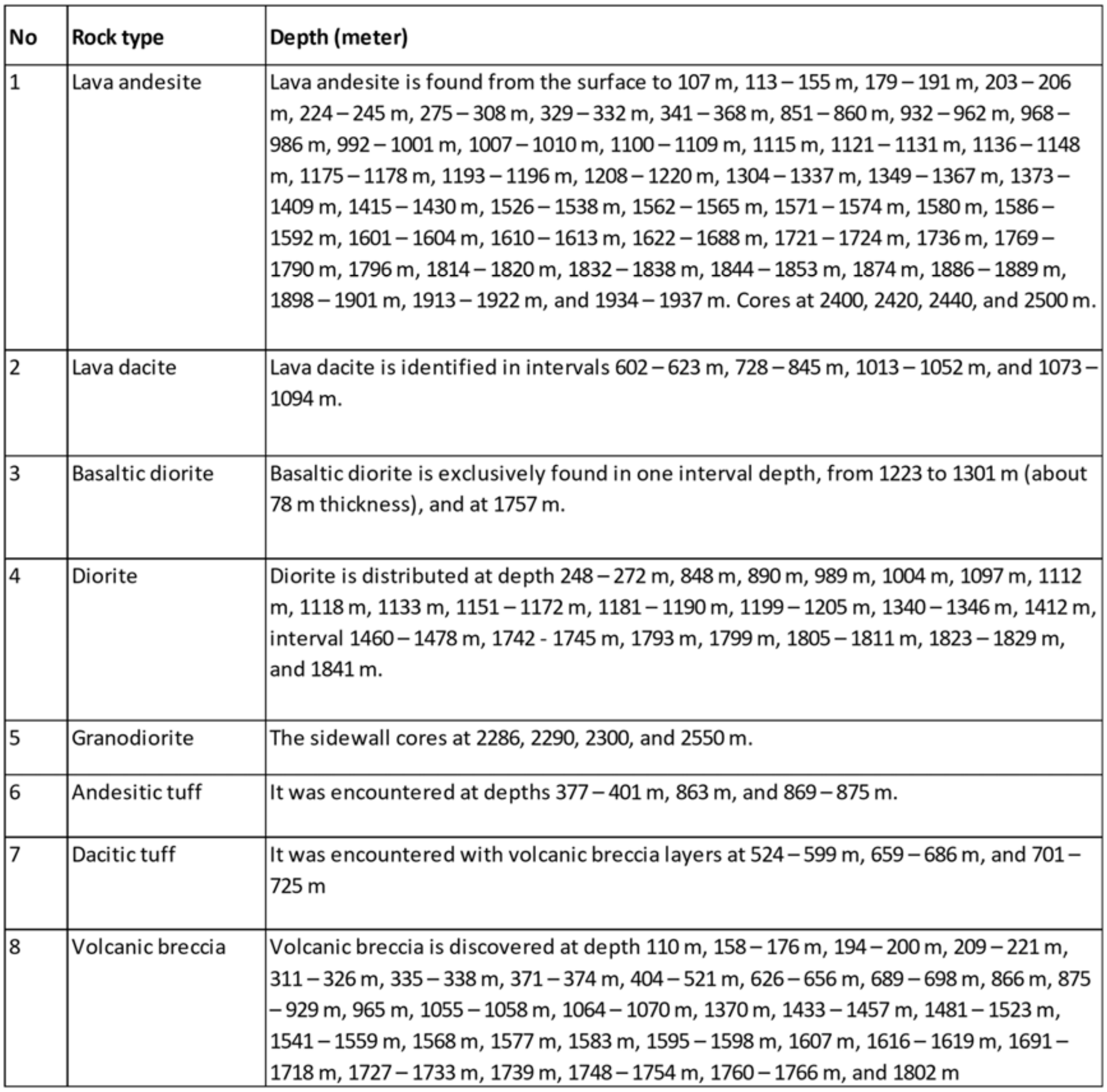

No	Rock type	Depth (meter)
1	Lava andesite	Lava andesite is found from the surface to 107 m, 113 – 155 m, 179 – 191 m, 203 – 206 m, 224 – 245 m, 275 – 308 m, 329 – 332 m, 341 – 368 m, 851 – 860 m, 932 – 962 m, 968 – 986 m, 992 – 1001 m, 1007 – 1010 m, 1100 – 1109 m, 1115 m, 1121 – 1131 m, 1136 – 1148 m, 1175 – 1178 m, 1193 – 1196 m, 1208 – 1220 m, 1304 – 1337 m, 1349 – 1367 m, 1373 – 1409 m, 1415 – 1430 m, 1526 – 1538 m, 1562 – 1565 m, 1571 – 1574 m, 1580 m, 1586 – 1592 m, 1601 – 1604 m, 1610 – 1613 m, 1622 – 1688 m, 1721 – 1724 m, 1736 m, 1769 – 1790 m, 1796 m, 1814 – 1820 m, 1832 – 1838 m, 1844 – 1853 m, 1874 m, 1886 – 1889 m, 1898 – 1901 m, 1913 – 1922 m, and 1934 – 1937 m. Cores at 2400, 2420, 2440, and 2500 m.
2	Lava dacite	Lava dacite is identified in intervals 602 – 623 m, 728 – 845 m, 1013 – 1052 m, and 1073 – 1094 m.
3	Basaltic diorite	Basaltic diorite is exclusively found in one interval depth, from 1223 to 1301 m (about 78 m thickness), and at 1757 m.
4	Diorite	Diorite is distributed at depth 248 – 272 m, 848 m, 890 m, 989 m, 1004 m, 1097 m, 1112 m, 1118 m, 1133 m, 1151 – 1172 m, 1181 – 1190 m, 1199 – 1205 m, 1340 – 1346 m, 1412 m, interval 1460 – 1478 m, 1742 - 1745 m, 1793 m, 1799 m, 1805 – 1811 m, 1823 – 1829 m, and 1841 m.
5	Granodiorite	The sidewall cores at 2286, 2290, 2300, and 2550 m.
6	Andesitic tuff	It was encountered at depths 377 – 401 m, 863 m, and 869 – 875 m.
7	Dacitic tuff	It was encountered with volcanic breccia layers at 524 – 599 m, 659 – 686 m, and 701 – 725 m
8	Volcanic breccia	Volcanic breccia is discovered at depth 110 m, 158 – 176 m, 194 – 200 m, 209 – 221 m, 311 – 326 m, 335 – 338 m, 371 – 374 m, 404 – 521 m, 626 – 656 m, 689 – 698 m, 866 m, 875 – 929 m, 965 m, 1055 – 1058 m, 1064 – 1070 m, 1370 m, 1433 – 1457 m, 1481 – 1523 m, 1541 – 1559 m, 1568 m, 1577 m, 1583 m, 1595 – 1598 m, 1607 m, 1616 – 1619 m, 1691 – 1718 m, 1727 – 1733 m, 1739 m, 1748 – 1754 m, 1760 – 1766 m, and 1802 m

Appendix C – Scattered magmatic differentiation trends relative to the MgO

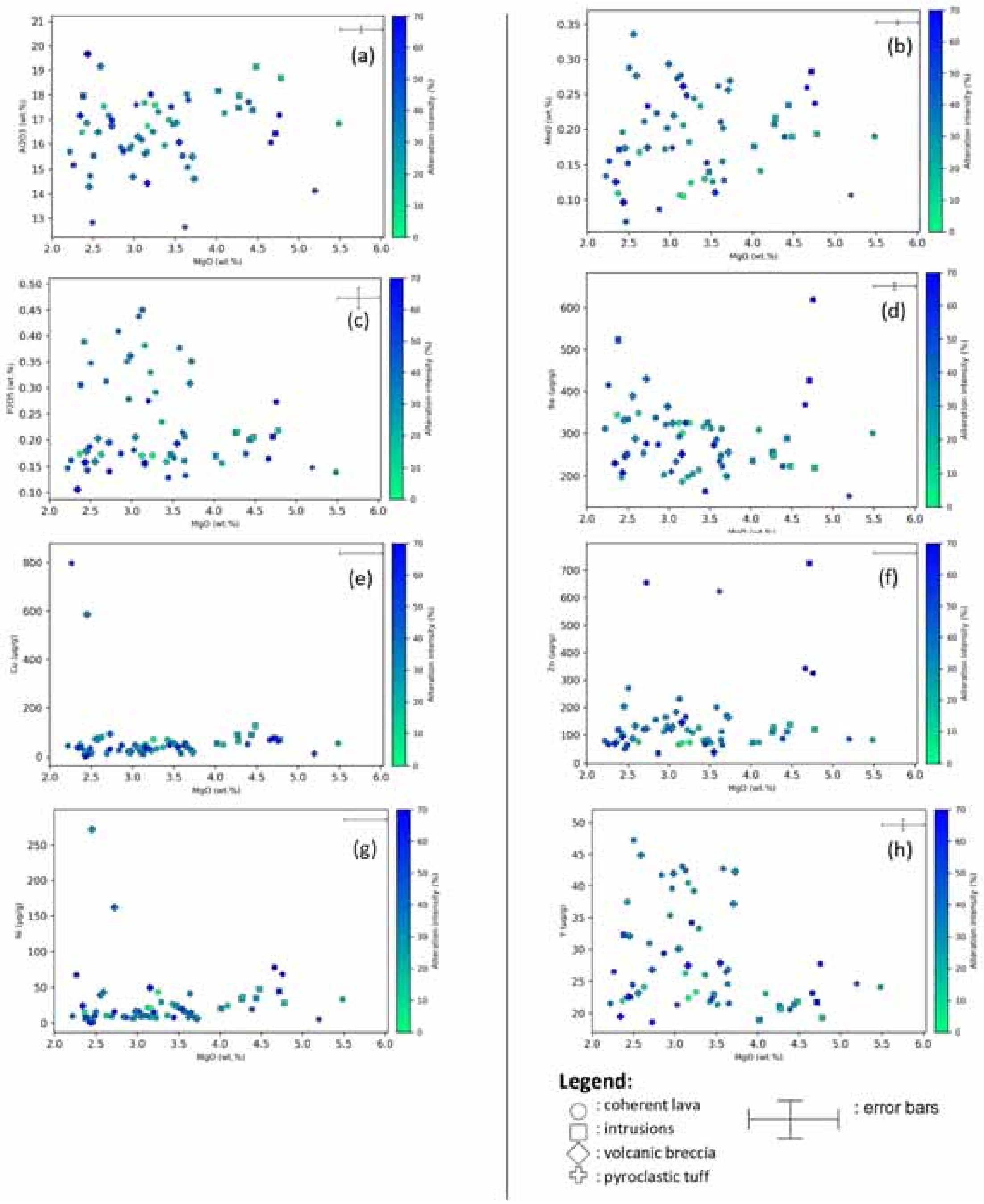

Appendix D – Paragenetic sequences observed in thin section samples

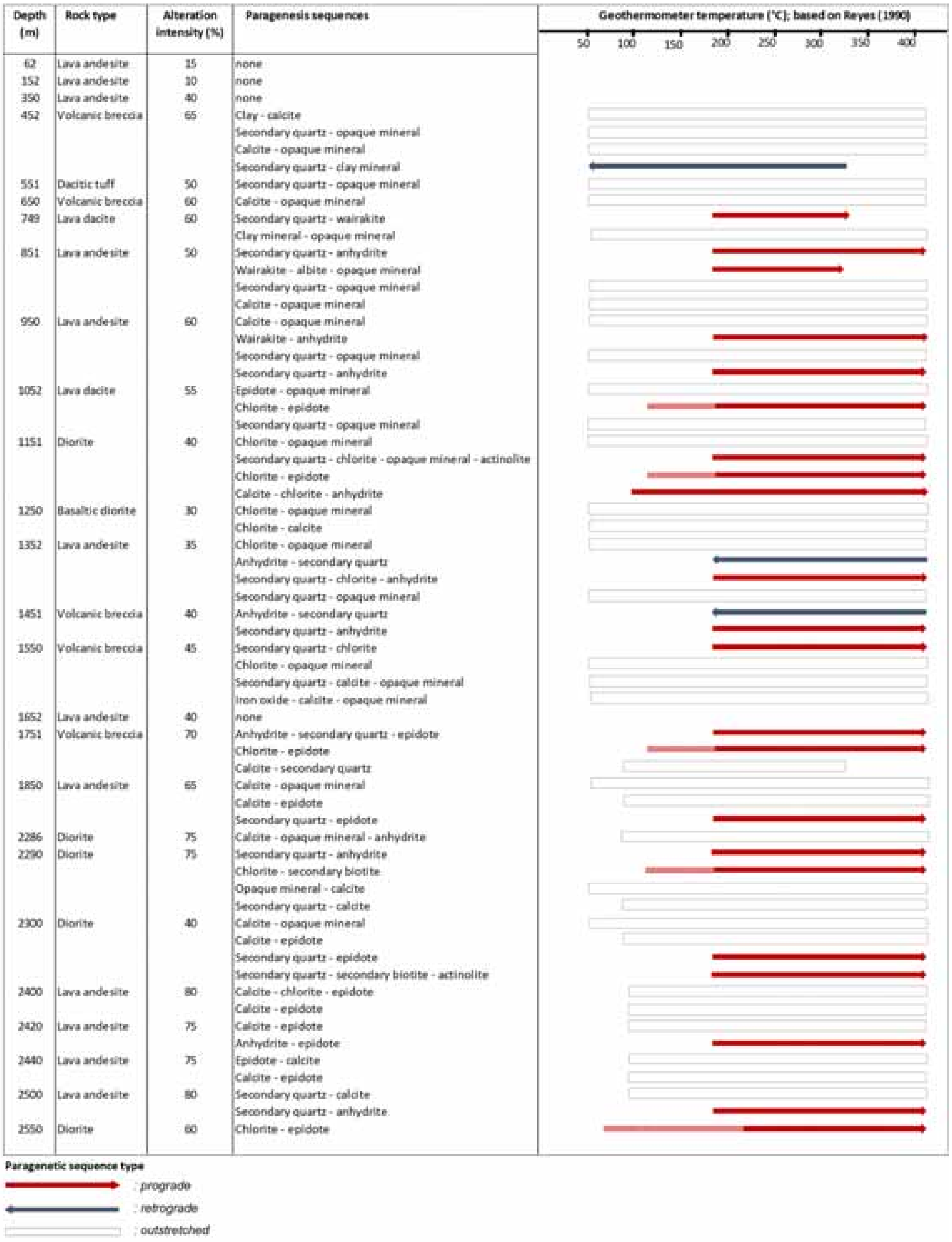

Depth (m)	Rock type	Alteration intensity (%)	Paragenesis sequences	Geothermometer temperature (°C); based on Reyes (1990)
62	Lava andesite	15	none	
152	Lava andesite	10	none	
350	Lava andesite	40	none	
452	Volcanic breccia	65	Clay - calcite	▭
			Secondary quartz - opaque mineral	▭
			Calcite - opaque mineral	▭
			Secondary quartz - clay mineral	←
551	Dacitic tuff	50	Secondary quartz - opaque mineral	▭
650	Volcanic breccia	60	Calcite - opaque mineral	▭
749	Lava dacite	60	Secondary quartz - wairakite	→
			Clay mineral - opaque mineral	▭
851	Lava andesite	50	Secondary quartz - anhydrite	→
			Wairakite - albite - opaque mineral	→
			Secondary quartz - opaque mineral	▭
			Calcite - opaque mineral	▭
950	Lava andesite	60	Calcite - opaque mineral	▭
			Wairakite - anhydrite	→
			Secondary quartz - opaque mineral	▭
			Secondary quartz - anhydrite	→
1052	Lava dacite	55	Epidote - opaque mineral	▭
			Chlorite - epidote	→
			Secondary quartz - opaque mineral	▭
1151	Diorite	40	Chlorite - opaque mineral	▭
			Secondary quartz - chlorite - opaque mineral - actinolite	→
			Chlorite - epidote	→
			Calcite - chlorite - anhydrite	→
1250	Basaltic diorite	30	Chlorite - opaque mineral	▭
			Chlorite - calcite	▭
1352	Lava andesite	35	Chlorite - opaque mineral	▭
			Anhydrite - secondary quartz	←
			Secondary quartz - chlorite - anhydrite	→
			Secondary quartz - opaque mineral	▭
1451	Volcanic breccia	40	Anhydrite - secondary quartz	←
			Secondary quartz - anhydrite	→
1550	Volcanic breccia	45	Secondary quartz - chlorite	→
			Chlorite - opaque mineral	▭
			Secondary quartz - calcite - opaque mineral	▭
			Iron oxide - calcite - opaque mineral	▭
1652	Lava andesite	40	none	
1751	Volcanic breccia	70	Anhydrite - secondary quartz - epidote	→
			Chlorite - epidote	→
			Calcite - secondary quartz	▭
1850	Lava andesite	65	Calcite - opaque mineral	▭
			Calcite - epidote	▭
			Secondary quartz - epidote	→
2286	Diorite	75	Calcite - opaque mineral - anhydrite	▭
2290	Diorite	75	Secondary quartz - anhydrite	→
			Chlorite - secondary biotite	→
			Opaque mineral - calcite	▭
			Secondary quartz - calcite	▭
2300	Diorite	40	Calcite - opaque mineral	▭
			Calcite - epidote	▭
			Secondary quartz - epidote	→
			Secondary quartz - secondary biotite - actinolite	→
2400	Lava andesite	80	Calcite - chlorite - epidote	▭
			Calcite - epidote	▭
2420	Lava andesite	75	Calcite - epidote	▭
			Anhydrite - epidote	→
2440	Lava andesite	75	Epidote - calcite	▭
			Calcite - epidote	▭
2500	Lava andesite	80	Secondary quartz - calcite	▭
			Secondary quartz - anhydrite	→
2550	Diorite	60	Chlorite - epidote	→

Paragenetic sequence type

→ : *prograde*

← : *retrograde*

▭ : *outstretched*

Appendix E – Thin section descriptions

Cutting sample 1. Depth 62 m. Lava andesite

The sample consists of lava chips (90%), and vesicular tuff chips (10%). The lava chips are porphyritic, unaltered. Phenocrysts size is around 0.2-0.5 mm. Their crystal habit is prismatic, euhedral to subhedral. Phenocrysts are composed of plagioclase (15%), and pyroxene (10%), clino- and orthopyroxene appear in the same amount. Ground mass is unaltered volcanic glass (55%).
Minor presence of tuff fragments. It shows vesicular texture with clay as the pore filling. Rock mass composed of volcanic glass and primary quartz. Tuff fragments are altered to clay minerals.

Secondary minerals are: Clay mineral (11%) forming from the ground mass, associated with dispersed opaque mineral. Opaque mineral is possibly pyrite (5%), fine-grained, granular, distributed in groundmass and within phenocrysts. Albite (2%), altering some of the plagioclase crystals. Iron oxide (2%) is rare, associated with opaque minerals, mostly found in pyroxene crystals. Low alteration intensity 20%, poorly sorted, no vein or paragenesis sequence.

Cutting sample 2. Depth 152 m. Lava andesite

The sample consists of lava lava chips (95%) and tuff chips (5%). The lava chips are porphyritic, unaltered. Phenocrysts size is around 0.2-1 mm, their habit is prismatic, euhedral to subhedral. Sample rocks show glomerocrysts. Phenocrysts are composed of coarse plagioclase (15%), and pyroxene (10%), mostly orthopyroxene. Groundmass is slightly altered volcanic glass (55%). Minor presence of tuff fragments. Composed of volcanic glass and angular shaped primary quartz. Tuff fragments are altered to clay and opaque minerals.

Secondary minerals are: Clay mineral (8%) brownish to green in color, found in ground mass. Opaque mineral possibly pyrite (5%) dispersed in the groundmass and around phenocrysts. Iron oxide, (4%) found in plagioclase and pyroxene crystals. Albite (3%) replaces plagioclase. Low alteration intensity 20%, poorly sorted, no vein or paragenesis sequence.

Cutting sample 3. Depth 350 m. Altered lava andesite

The sample consists of lava chips. It is porphyritic, moderately altered by iron oxide, calcite, and clay. Phenocrysts are coarse, with a size around 0.2-1 mm, their habit is prismatic, euhedral to subhedral. Phenocrysts are composed of plagioclase (18%), and pyroxene (10%), clino- and orthopyroxene appear in the same amount. Groundmass is unaltered volcanic glass (46%).

Secondary minerals are: Iron oxide (8%) associated with clay (5%) and opaque minerals (8%), found in phenocrysts´ rims, also in groundmass. Calcite (5%) and clay found as deposits in microfractured plagioclase. Albite rarely found in plagioclase. Moderate alteration intensity 26%, poorly sorted, micro-veins with low intensity is found filled by clay mineral and calcite.

Cutting sample 4. Depth 452 m. Altered volcanic tuff (or breccia)

The sample consists of volcanic tuff (85%) and lava (15%). Volcanic tuff is fragmental, shows flow structure and is glassy. Composed of clay size altered volcanic glass, and coarse size 0.5-1 mm of primary quartz with embayment structure. Small amount of lava fragments composed of fine-grained plagioclase and pyroxene as phenocrysts.

Secondary minerals are: Calcite (10%) abundantly found in rock mass and veins associated with clay and opaque minerals. Clay mineral (8%) formed by strong alteration of ground-mass, and occurs also as open space fillings. Secondary quartz (3%). Opaque mineral, possibly pyrite (3%). Chlorite (2%) formed by the alteration of the groundmass intensively. Iron oxide, rare. Moderate alteration intensity 26%, veins intensity increases compare to sample from depth 350 m. Veins are filled by calcite, clay minerals, opaque minerals and quartz. Paragenesis sequence: Clay – calcite, quartz – opaque mineral, calcite – opaque mineral, secondary quartz – clay mineral.

Cutting sample 5. Depth 551 m. Altered vitric tuff

The sample consists of volcanic tuff (85%) and lava (15%). Volcanic tuff is fragmental, composed of altered volcanic glass and fine grained feldspar. Strongly altered by secondary quartz, calcite, clay, and opaque minerals. Lava chips are strongly altered by calcite, the phenocrysts are replaced by calcite and clay minerals.

Secondary minerals are: Secondary quartz (20%), found as space filling, replacing the ground mass, and veins. As vein, it is associated with calcite and opaque minerals. Calcite, (10%) replaces the phenocrysts and as veins. Clay minerals (12%). Opaque minerals (8%) dominantly fill the veins, and alters the groundmass. Alteration intensity 50%. Veins are filled by secondary quartz, calcite, clay, and opaque minerals. Paragenesis sequences: Secondary quartz – opaque mineral.

Cutting sample 6. Depth 650 m. Altered vitric tuff

The sample consists of strongly altered volcanic tuff. Fragmental texture. Composed of fine grained volcanic material. The former phenocrysts are identified as feldspar that replaced by calcite and clay minerals.

Secondary minerals are: Secondary quartz (20%) found as space filling, replacing the groundmass, and veins. Calcite (20%) associated with anhydrite replaces the phenocrysts and as veins. Clay minerals (8%). Anhydrite (5%) replaces feldspar grains. Opaque minerals (5%) dominantly fills the veins. Sericite (2%) dispersed in the groundmass. Alteration intensity 60%. Alteration intensity increasing in the rock mass, and the vein intensity is decreasing compare to sample from 551 m depth. Minor veins are found filled by calcite, opaque, and clay minerals. Paragenesis sequences: Calcite – opaque mineral.

Cutting sample 7. Depth 749 m. Altered lava dacite

The sample consists of lava chips. Porphyritic texture is identified with the fully altered prismatic grains (possibly feldspars). The grain size of the former phenocrysts varies from 0.2 to 1.2 mm, altered by calcite, clay minerals, and epidote. Majority of the groundmass is altered to secondary quartz and calcite.

Secondary minerals are: Secondary quartz (15%) as rock mass replacement and vein filling. Calcite (15%) is associated with clay minerals possibly chlorite (10%) replaces the phenocryst grains, groundmass, and as veins. Opaque minerals (8%) dispersed in the rock mass and veins. Anhydrite (3%) and wairakite (3%) are found as veins. Sericite (3%) and epidote (3%) found as granular secondary minerals. High alteration intensity 60%. The primary grains are completely replaced by secondary minerals. The veins are dominated by calcite, secondary quartz, opaque minerals. Minor veins are filled by anhydrite and wairakite. Paragenesis sequences: secondary quartz – wairakite, chlorite – opaque mineral.

Cutting sample 8. Depth 851 m. Altered lava andesite

The sample consists of lava chips. It has porphyritic texture. Phenocrysts are plagioclase grains in size 0.2 to 1 mm, which are moderately altered. Plagioclase grains are still recognisable by its twinning feature. Groundmass is composed of altered volcanic glass.

Secondary minerals are: Calcite (15%) replaces phenocrysts, fills the veins, and alters the groundmass. Secondary quartz (10%) found as vein and in the groundmass. Opaque minerals (10%) dispersed in the rock mass, and as veins. Anhydrite (8%) and wairakite (5%) are found as veins. Anhydrite also spotly found in rock mass. Albite (2%) replaces plagioclase.

Alteration intensity 50%. Veins are dominated by calcite, secondary quartz, opaque mineral, anhydrite, and wairakite. Paragenesis sequences: Secondary quartz – anhydrite, wairakite – albite – opaque mineral, secondary quartz – opaque mineral, calcite – opaque mineral.

Cutting sample 9. Depth 950 m. Altered lava andesite

Cutting chips consist of porphyritic lava. Phenocrysts are plagioclase grains in size 0.2 to 1.2 mm, they are prismatic, moderately altered by albite, anhydrite, and calcite. The groundmass is altered volcanic glass with secondary quartz, opaque minerals, calcite, and anhydrite.

Secondary minerals are: Calcite (15%) replaces plagioclase and as veins. Secondary quartz (l5%) found in volcanic glass and veins, associated with opaque minerals and clay. Opaque mineral (10%), possibly pyrite is dispersed in rock mass, and as veins. Anhydrite (8%) replaces plagioclase grains, also found as veins and space filling with wairakite (rare). Clay mineral (7%) possibly chlorite is associated with opaque mineral. Albite (5%) dominantly replaces plagioclase. Fine grain epidote is found in groundmass (rare).

Alteration intensity 60%. Veins are filled by calcite, secondary quartz, opaque mineral, anhydrite, and wairakite. Paragenesis sequences: Calcite – opaque mineral, wairakite – anhydrite, secondary quartz – opaque mineral, secondary quartz – anhydrite.

Cutting sample 10. Depth 1052 m. Altered lava andesite

Cuttings are composed of porphyritic lava. Phenocrysts are plagioclase grains 0.1 to 0.6 mm, moderately altered to clay mineral, albite, anhydrite, calcite, and epidote. Groundmass is altered to secondary quartz, opaque mineral, and clay.

Secondary minerals are: Secondary quartz (15%), calcite (12%), and opaque mineral (8%) are dominantly replaces plagioclase grains, and dispersed in groundmass. Also found as veins associated with anhydrite and chlorite. Albite (7%) replaces plagioclase. Anhydrite (6%) as veins. Chlorite (5%) and epidote (2%) appear together as veins, and in phenocrysts. Wairakite (rare) in veins, with anhydrite. Alteration intensity decreases to 55%. Paragenesis sequences: Epidote – opaque mineral, chlorite – epidote, secondary quartz – opaque mineral.

Cutting sample 11. Depth 1151 m. Diorite

The sample is composed of coarse – grained rock with phaneritic texture. Phenocrysts are medium size plagioclase, 0.3 – 1.5 mm, and coarse hornblende, 0.5 to 1 mm. Plagioclase is altered to chlorite, calcite, epidote, and albite. Hornblende is replaced by chlorite and opaque minerals.

Secondary minerals are: Secondary quartz (9%) as veins, and replaces groundmass. Chlorite (8%) replaces phenocrysts and hornblende. Also found as veins with calcite (7%), and opaque minerals (6%). Albite (3%) replaces plagioclase and associated with epidote. Epidote (3%) increasingly appear in veins and in plagioclase grains. Anhydrite (2%) is present as vein. Actinolite (2%) is associated with chlorite and opaque minerals in veins. Alteration intensity is 40%. Paragenesis sequences: chlorite – opaque mineral, secondary quartz – chlorite – opaque mineral – actinolite, chlorite – epidote, calcite – chlorite – anhydrite.

Cutting sample 12. Depth 1250 m. Diorite

Cutting sample is composed of coarse grained rock chips, very possible intrusion. Medium to coarse grained crystals appear with phaneritic texture. Plagioclase dominates the primary mineral assemblage about 90%, and pyroxene around 10%. Plagioclase appears in euhdral to subhedral crystal habit, with a coarse size from 0.5 to 2 mm. Pyroxene presents in medium size, 0.2 – 0.5 mm. Generally, plagioclase and pyroxene are moderately altered to unaltered.

Secondary minerals are: calcite (7%) is associated with chlorite. Opaque minerals possibly pyrite (6%) present as vein fillings. Chlorite (4%) replaces pyroxene and plagioclase intensely. Epidote (5%) is formed in plagioclase and pyroxene in fine size grains. Albite (5%) significantly replaces most of the plagioclase crystals. Secondary quartz (3%) appears as space fillings, and in plagioclase. Anhydrite (rare) presents as vein.

Alteration intensity drops to 30%. Permeability in the sample is low. Veins and porosity is rare. Pyrite and chlorite generally fills the veins. Secondary minerals mostly found as mineral replacement in plagioclase and pyroxene crystals. Paragenesis sequences: Chlorite – opaque mineral, chlorite – calcite.

Cutting sample 13. Depth 1352 m. Altered lava andesite

Sample is composed of lava chips. Grain size aphanitic to very fine grained, <0.1 mm. The sample isporphyritic with trachytic texture. The rock is composed dominantly of fine size feldspar and volcanic glass. Moderately altered.

Secondary minerals are: calcite (10%) is found replacing the fine grained crystals in the ground mass and as veins. Opaque minerals possibly pyrite (8%) are dispersed. As veins pyrite is associated with chlorite and secondary quartz. Chlorite (6%) mostly found as veins with secondary quartz (5%) and anhydrite (4%). Fine grain epidote (2%) spotly found in ground mass. Chips of wairakite (rare) is found as vein fragments.

Alteration intensity is around 35%. Permeability is low. Small size veins are found generally filled by calcite, opaque minerals, chlorite, secondary minerals, and anhydrite.
Some veins are crossing cut with the others. For example, secondary quartz vein cuts chlorite vein, anhydrite vein cuts secondary quartz vein. Paragenesis sequences: Chlorite – opaque mineral, anhydrite – secondary quartz, secondary quartz – chlorite – anhydrite, secondary quartz – opaque mineral.

Cutting sample 14. Depth 1451 m. Altered vitric tuff

The sample is composed of mixture chips of tuff (85%) and lava (15%) fragments. Tuff is consisted of very fine grained altered volcanic glass material. Lava is composed of fine grained feldspar from 0.1 to 0.3 mm, euhedral to subhedral. Both tuff and lava are moderately altered.

Secondary minerals are: Secondary quartz (10%) replaces the tuff materials and as veins. Calcite (7%), opaque mineral (7%), and anhydrite (5%) are associated in veins systems. Albite (5%) replaces coarse feldspar grain in lava fragments. Chlorite (3%) is found in rock matrix, mostly in tuff. Wairakite (2%) forms fine size veins. Epidote (1%) fills the pore space in the rock. Adularia, rarely found as clasts of veins.

Alteration intensity 40%. Permeability medium to low. The chips are in lack of veins. Secondary quartz, calcite, and anhydrite are commonly found as the vein fillings. Feldspar was replaced by albite and chlorite. Paragenesis sequences: Anhydrite – secondary quartz, secondary quartz – anhydrite.

Cutting sample 15. Depth 1550 m. Altered vitric tuff (Breccia)

Sample is identified as breccia by its contact structure. It is consisted of tuff and lava fragments. Tuff fragments composed of altered volcanic glass and fine feldspar. Lava composed of microlits plagioclase and fine feldspar. The sample is intensely altered.

Secondary minerals are: Secondary quartz (13%), clay minerals (10%), calcite (7%), opaque minerals (7%), and chlorite (4%) are abundantly found in the matrix and veins. These minerals are associated with vein and pore fillings. Anhydrite (4%) is mainly formed in veins. Iron-oxide, wairakite, and epidote are rarely found and are associated with the pore fillings.

Alteration intensity and permeability increases to 45% and 17%, respectively. Various paragenesis sequences are abundantly found. Paragenesis sequence: Secondary quartz – chlorite, chlorite – opaque mineral, secondary quartz – calcite – opaque mineral, iron-oxide – calcite – opaque mineral.

Cutting sample 16. Depth 1652 m. Altered lava dacite

The cuttings have porphyritic texture, inequigranular. It is identified as lava with trachytic (flow) texture. It is composed of altered volcanic glass and fine grained feldspar. Intensely altered.

Secondary minerals are: calcite (9%), secondary quartz (9%), clay (7%), and opaque minerals (5%) are distributed abundantly in ground mass and as vein fillings. Albite (3%) replaces the fine grained feldspar, associated with chlorite (3%). Anhydrite (3%) and epidote (2%) are found as veins. Iron- oxide is rare. Alteration intensity 40%, permability moderate to high (20%). No clear paragenesis sequence was observable from the sample.

Cutting sample 17. Depth 1751 m. Altered volcanic breccia

Sample is composed of fragments of intensely altered tuff and lava. The main component is altered volcanic glass, fine grained plagioclase. Secondary minerals are: Calcite (13%) and secondary quartz (13%) are found in veins. Clay (11%) and opaque minerals (10%) are dispersed in ground mass and cavities. Albite (7%) replaces the composition of plagioclase. Chlorite (7%) is associated with clay mineral. Anhydrite (6%) and epidote (3%) are commonly found together as veins, in some samples they show paragenesis sequences.

Alteration intensity 70%. The chips are heavily altered. The permeability increases to 50%. Vein and cavity density is generally increasing. Paragenesis sequence: Anhydrite – secondary quartz – epidote, chlorite – epidote, calcite – secondary quartz.

Cutting sample 18. Depth 1850 m. Altered lava andesite

Cutting sample is composed of lava chips. Texture porphyritic. Phencrysts size is around 0.2 to 1 mm, euhedral, composed of heavily altered (by epidote and chlorite) prismatic minerals, feldspar. Very vew fragments of plagiclase with a size of around 0.2 – 0.5 mm were found, and they were altered to clay minerals. Groundmass is very fine-grained, volcanic glass that was altered to secondary quartz.

Secondary minerals are: Secondary quartz (27%) replaced the majority of the ground mass. The groundmass is completely altered to secondary quartz and clay mineral. Chlorite (15%) replaced the groundmass, phenocrysts, and filled the open vesicles. Calcite (10%) and opaque minerals (7%) are mostly found as veins, small fraction were dispersed in the rock groundmass. Epidote (4%) replaced the phenocrysts and occurs in veins (2%) and illite (rare) was found in plagioclase.

Alteration intensity 65%. The chips are generally altered to secondary quartz (silisification) especially in the groundmass. The permeability from vein density is around 27%. Veins are occur in many sizes, small and bigger aperture veins. Paragenesis sequence: Calcite – opaque mineral, calcite – epidote, secondary quartz – epidote.

Core sample 1. Depth 2286 m. Altered intrusion diorite (Hb andesite)

Intrusion rock from a core sample was taken near the vein zone of the rock. It has phaneritic, holocrystalline texture. The phenocryst are intensely altered feldspar and hornblende. Coarse-grained feldspar have a size around 0.4 – 1 mm, it is prismatic, altered to calcite, chlorite, and quartz. Horblende has a size around 0.1 – 0.2 mm, it is euhedral, altered to chlorite and calcite.

Secondary minerals are: Calcite (25%) dominantly altered the grains, as well as veins. Secondary quartz (13%) presents as space fillings and as veins. Chlorite (10%) altered ground mass and as veins associated with opaque minerals. Albite (8%) replaced the feldspar grains. Anhydrite (7%) appeared as veins and flaky minerals, associated with chlorite. Opaque minerals (7%) and wairakite (3%) were found in the vein system. Epidote (2% to rare) was found as fine-grained granular crystals dispersed and associated with chlorite.

Alteration intensity 75%, the sample contains a vein system which is dominated by calcite and chlorite. Cross-cutting between veins are found, namely calcite cuts opaque minerals vein, wairakite cut secondary quartz, and wairakite cut calcite veins. Paragenesis sequence: Calcite – opaque mineral – anhydrite.

Core sample 2. Depth 2290 m. Altered diorite

The core was identified as an intrusive rock. Composed of coarse grained prismatic crystals with sizes from 0.5 to 1.5 mm. Grains have subhedral crystal habit. The minerals are feldspar, pyroxene, and hornblende that are heavily altered to calcite and chlorite.

Secondary minerals are: Calcite (25%) appeared as veins and replaced grains. Secondary quartz (15%) and opaque minerals (10%) were found as space fillings and veins. They are associated with anhydrite. Anhydrite (10%) and chlorite (15%) replaced the grains and as veins. Secondary biotite (rare) occurs as vein filling. Epidote (rare) occurs as a replacement in grains.

Alteration intensity 75%. The veins are intensively fractured the ground mass. Veins are filled by secondary quartz, calcite, anhydrite, and opaque minerals. Some crosscutting relationships are observable. Anhydrite vein cut by secondary quartz vein. Paragenesis sequence: Secondary quartz – anhydrite, chlorite – secondary biotite, opaque mineral – calcite, secondary quartz – calcite.

Core sample 3. Depth 2300 m. Intrusions (granodiorite)

The core sample is identified as an intrusion rock. It has a phaneritic, and holocrystalline texture. It is composed of coarse-grained plagioclase and hornblende. Subhedral to euhedral prismatic plagioclase (45%) presents in size 0.5 – 1 mm. It is moderately altered. Euhedral hornblende (15%) has a grainsize of 0.5 – 3 mm, it is pleochroic from light brown to dark brown and weakly altered. Quartz (10%) filled in between grains.

Primary quartz (5%) filled the veins. Chlorite (7%) replaced hornblende and filled the space in between grains. It is associated with opaque minerals, secondary biotite, actinolite, and epidote. Albite (7%), with secondary quartz and anhydrite eplaced plagioclase grains. Opaque minerals (4%) are dispersed in the ground mass and occur as veins. Secondary biotite (4%) is associated with actinolite (2%) replaced hornblende and deposited in between grains. Anhydrite (1%) was found as veins.

Alteration intensity 40%. Very few veins were found. Most of the secondary minerals filled the space in between grains, and occurred as a replacement in grains . Paragenesis sequence: Calcite – opaque mineral, calcite – epidote, secondary quartz – epidote.

Core sample 4. Depth 2400 m. Altered lava (possibly andesite)

The core sample was identified as altered lava. It has a porphyritic texture and is hypocrystalline. It is composed of fine to medium-grained altered feldspar, possibly amphibole, and altered groundmass. Feldspar is in prismatic shape, size 0.2 – 1 mm, euhedral, strongly altered to calcite and epidote. Possible amphibole was found in euhedral prismatic hexagonal shape, size 0.4 – 1 mm, altered to calcite and clay minerals.

Secondary minerals are: Secondary quartz (25%) replaced the groundmass occurs with calcite, chlorite, and clay mineral. Calcite (20%) and epidote (7%) replaced the grains and occur as veins. Chlorite (15%) appeared as space-filling, with calcite and as veins. Clay minerals (10%) are dispersed in the ground mass with opaque minerals (3%).

Alteration intensity 80%. The rock has completely altered. An open fracture filled with a vein of calcite – chlorite – epidote was found in the sample. Moreover, smaller veins filled with similar secondary minerals were also found abundant in this sample. The primary minerals were replaced by the secondary minerals. Groundmass was altered to secondary quartz, calcite, and clay mineral. Paragenesis sequence: Calcite – chlorite – epidote, calcite – epidote.

Core sample 5. Depth 2420 m. Altered lava (andesite)

A core sample is a lava with a porphyritic texture. Phenocrysts are composed of plagioclase with a size 0.2 – 0.4 mm. They are highly altered to calcite and secondary quartz. The groundmass is composed of fine-grained volcanic glass material and altered to secondary quartz. The trachytic texture is visible in the groundmass.

Secondary minerals are: Calcite (25%) appeared as veins, Secondary quartz (20%) abundantly replaced the groundmass, and as veins, Opaque minerals (12%) are associated with calcite and chlorite (10%) in veins, also dispersed in the groundmass. Epidote (4%) occurs as space-filling and in veins. Anhydrite (4%) is associated with calcite and prehnite in the veins. Prehnite (rare) is present as a very fine grained mineral near the veins. Alteration intensity is 75%. Veins are dominated by calcite. Cross-cutting relationships between veins are observable. The density of the veins is high, with a larger aperture around 0.1 to 0.5 mm. Paragenesis sequence: Calcite – epidote, anhydrite – epidote.

Core sample 6. Depth 2440 m. Altered lava (possibly andesite)

The core is a lava with very few phenocrysts. Texture is porphyritic. Graoundmass is composed of fine-grained volcanic glass that was replaced by secondary quartz. However, the trachytic texture is still visible. The phenocrysts are prismatic minerals with a size of 0.2 to 0.4 mm, that were replaced by epidote and calcite.

Secondary minerals are: Secondary quartz (35%) mainly replaced the groundmass. Calcite (20%) is found as veins, replacement of phenocrysts, and space fillings associated with chlorite (10%) and opaque minerals (6%). Epidote (4%) was found as veins and mineral replacement in phenocrysts associated with calcite.

Alteration intensity is 75%. The dimensions of the veins and their density are smaller compared to the core sample from 2420 m. Paragenesis sequence: Epidote – calcite, calcite – epidote.

Core sample 7. Depth 2500 m. Altered lava (possibly andesite)

The core sample has a fine-grained, porphyritic texture, where the groundmass, and phenocrysts are strongly altered. Phenocrysts were fine-grained feldspar which are completely altered to calcite. The groundmass was replaced by secondary quartz.

Secondary quartz (50%) replaced the groundmass and abundantly filled the veins and occurs with calcite. Calcite (20%) replaced phenocrysts and groundmass, and occurs as veins. Opaque minerals (10%) are dispersed in the ground mass, and are present in veins. These three secondary minerals are associated with the vein system. Alteration intensity is high (80%). The veins are abundantly contain secondary quartz, calcite, and opaque minerals. Cross-cutting in between veins is common. Paragenesis sequence: Secondary quartz – calcite, secondary quartz – anhydrite.

Core sample 8. Depth 2550 m. Altered diorite

Sample core was identified as intrusion rock, possibly diorite. It is composed of coarse plagioclase and hornblende, in size ranges of 0.5 to 2 mm.

Secondary minerals are: Calcite (25%) intensively replaced the grains. Secondary quartz (17%) occurs as space fillings and veins associated with chlorite (10%).
Opaque minerals (5%) are present as veins. Epidote (3%) spotly found as vein fillings and replacement in minerals. Alteration intensity is 60%. Vein intensity is low to intermediate. However, the secondary minerals appear as the open space fillings in between grains. Paragenesis sequence: Chlorite – epidote.